

Analysis and Evaluation of Brush-DC Equivalent Controlled Multiphase Cage Induction Machine Drive

by
Nkosinathi Gule

*Dissertation presented in fulfilment of the requirements for the degree
Doctor of Philosophy in the Faculty of Engineering at Stellenbosch University*



Supervisor: Prof. Maarten J. Kamper
Department of Electrical and Electronic Engineering

March 2011

Declaration

By submitting this dissertation electronically, I declare that the entirety of the work contained therein is my own, original work, that I am the sole author thereof (save to the extent explicitly otherwise stated), that reproduction and publication thereof by Stellenbosch University will not infringe any third party rights and that I have not previously in its entirety or in part submitted it for obtaining any qualification.

March 2011

Copyright © 2011 University of Stellenbosch

All rights reserved

Abstract

The multiphase induction machine drive has been under investigation for the last half century. Although it offers several attractive advantages over the conventional three-phase induction machine drive, it is restricted to highly specialised applications. One aspect of the multiphase induction machine drive is the complexity of the control algorithm for decoupled flux and torque control. The complexity, arising from the required coordinate transformations, increases with increase in the number of phases of the machine. Recently, a method that allows the control of a six-phase induction machine drive without any coordinate transformations was developed and tested. This new control technique allows the control of the machine to be similar to that of dc machines through the use of special trapezoidal-shaped stator current waveforms. These stator phase current waveforms consist of field (flux) and torque current components, with flat-topped amplitudes allowing a stator phase to act alternately in time as either a flux or a torque producing phase. The idea is to have a number of stator phases acting as flux producing phases, whilst the remaining phases act as torque producing phases at each time instance. This dissertation takes a further step in the research on this particular control technique. As the control method relates directly to the brush-dc machine operation, in this dissertation, the control method is defined as a “brush-dc equivalent” (BDCE) control method.

First, in this dissertation, a simple analytical method is developed to determine a defined optimal ratio of the number of field to the number of torque phases of a multiphase induction machine that utilises trapezoidal stator current waveforms. The method is applied to induction machines with up to fifteen stator phases. Finite element analysis is used to verify the validity of the developed criterion and to verify the square-like air gap flux density.

Secondly, in this dissertation, an analytical method for predicting and evaluating the rotor bar current waveform of a cage multiphase induction machine is proposed. The method is based on the Fourier transform and the winding function theory under linear condition assumptions. The method also allows for the calculation of the electromagnetic torque and rotor bar losses. Skin effect is considered in the calculation of the rotor bar resistance of the machine. Again, finite element analysis is used to verify the analytically calculated results. The developed method can be expanded and used to evaluate the rotor current waveform of any multiphase induction machine supplied with any stator current waveforms.

The BDCE control method is implemented on a prototype nine-phase cage-rotor induction machine drive. A nine-phase inverter and control system are developed for supplying the nine-phase induction machine with the trapezoidal stator current waveforms. Rotor current waveform measurements are taken on a specially designed rotor to verify the analytically predicted waveform. The linear relationship of the developed torque and torque current of the proposed BDCE control method is verified through measurements. Through the comparison of analytical calculated results with finite element calculated and measured results, it is shown in this dissertation that the developed analytical techniques can be used in the design and performance analysis of multiphase induction machines. Also, from the results, it is clear that the new control technique works remarkably well even in the flux weakening region. However, outstanding aspects, such as efficiency and generated torque quality of the proposed drive still need to be investigated further.

Opsomming

Die multifase induksiemasjien aandryfstelsel word in die laaste halwe eeu al in navorsing ondersoek. Alhoewel dit verskeie aantreklike voordele bied bo die konvensionele driefase induksiemasjien aandryfstelsel, is dit beperk tot hoogs gespesialiseerde toepassings. Een aspek van die multifase induksiemasjien aandryfstelsel is die kompleksiteit van die beheer algoritme vir ontkoppelde vloed en draaimoment beheer. Die kompleksiteit, wat voortspruit uit die vereiste koördinaat transformasies, neem toe met toename in die aantal fases van die masjien. Onlangs is 'n metode wat die beheer van 'n sesfase induksiemasjien sonder enige koördinaat transformasies doen, ontwikkel en getoets. Hierdie nuwe beheertegniek maak die beheer van die masjien soortgelyk aan dié van GS masjiene deur die gebruik van spesiale trapezium-vormige statorstroom golfvorms. Hierdie stator fasestroom golfvorms bestaan uit veld- (vloed-) en draaimoment-stroom komponente met plat amplitudes, sodat 'n statorfase om die beurt in tyd optree as óf 'n vloed of 'n draaimoment genereerde fase. Die idee is om 'n aantal statorfases te hê wat as vloed genereerde fases dien, terwyl die oorblywende fases as draaimoment genereerde fases optree op enige tydstep. Hierdie tesis neem 'n verdere stap in die navorsing op hierdie spesifieke beheertegniek. Met die beheermetode wat direk verband hou met borsel-GS masjien werking, word in hierdie proefskrif die beheermetode as 'n "borsel-GS ekwivalente" ["brush-DC equivalent" (BDCE)] beheermetode gedefinieer.

In die eerste plek word in hierdie proefskrif 'n eenvoudige analitiese metode ontwikkel om 'n gedefinieerde optimale verhouding van die aantal veld tot die aantal draaimoment fases van 'n multifase induksiemasjien te bepaal, wat van trapesoïdale statorstroom golfvorms gebruik maak. Die metode word toegepas op induksiemasjiene met tot vyftien statorfases. Eindige element analise is gebruik om die geldigheid van die ontwikkelde kriterium te verifieer en om die vierkantvormige lug-gaping vloeddigheid te verifieer.

In die tweede plek word in hierdie proefskrif 'n analitiese metode vir die voorspelling en evaluering van die rotorstaafstroom golfvorm van 'n kourotor multifase induksiemasjien voorgestel. Die metode is gebaseer op die Fourier transform en die wikkelfunksie teorie onder lineêre-toestand aannames. Die metode wend hom ook daartoe tot die berekening van die elektromagnetiese draaimoment en rotorstaafverliese. Die huideffek word in ag geneem in die berekening van die rotorstaafweerstand van die masjien. Weereens is eindige element analise gebruik om die analitiese berekende resultate te verifieer. Die ontwikkelde metode kan uitgebrei en gebruik word om die rotorstroom golfvorm van van enige multifase induksiemasjien te evalueer wat gevoer word met enige statorstroom golfvorms.

Die BDCE beheermetode is toegepas op 'n prototipe negefase kourotor induksiemasjien. 'n Negefase omsetter en beheerstelsel is ontwikkel vir die toevoer van die trapesoïdale statorstroom golfvorms aan die negefase induksiemasjien. Die rotorstroomgolfvorm metings is geneem op 'n spesiaal ontwerpte rotor om die analitiese voorspelde golfvorm te verifieer. Die lineêre verwantskap tussen die ontwikkelde draaimoment en draaimomentstroom van die voorgestelde BDCE beheermetode is geverifieer deur metings. Deur die analitiese berekende resultate met die eindige element berekende en gemete resultate te vergelyk, wys hierdie proefskrif dat die ontwikkelde analitiese tegnieke gebruik kan word in die ontwerp en werkverrigting analise van 'n multifase induksiemasjien. Vanuit die resultate is dit ook duidelik dat die nuwe beheertegniek besonder goed werk, selfs in die vloed-verswakking spoedgebied. Egter, uitstaande aspekte soos effektiwiteit en genereerde draaimoment kwaliteit van die voorgestelde aandryfstelsel moet nog verder ondersoek word.

Acknowledgements

I would like to thank my promoter, Prof. Maarten J. Kamper for his support and guidance throughout this project. I would also like to thank:

- My sponsor, ESKOM for their financial support.
- My colleagues at the Electrical Machines Laboratory for their support.
- David Groenewald for designing the inverter control boards.
- The people in the workshop for their help in assembling the machine and test setup.
- My wife for all her unlimited support.
- To God be the Glory, Great things He has done!

To my wife, Nonjabulo.

Table of Contents

Declaration	i
Abstract	ii
Opsomming	iii
Acknowledgements	iv
Chapter 1 Introduction	1
1.1 Background on Multiphase Induction Machines	1
1.1.1 Classification and winding layouts	2
1.1.2 Control of multiphase induction machine systems	3
1.1.3 Voltage source inverter current control	4
1.2 Rotor Current Measurements	5
1.3 Objectives of the Study	5
1.4 Dissertation layout	6
Chapter 2 Brush-DC Equivalent (BDCE) Control Method	7
2.1 Background on Brush-DC Machines with Compensating Windings	7
2.2 Conceptualisation of the BDCE Operation of Multiphase Induction Machine	8
2.3 Principle and Description of BDCE Multiphase Induction Machine Drive	9
2.4 Analysis of a BDCE Six-Phase Induction Machine	11
2.5 Summary and Conclusions	12
Chapter 3 Optimal Ratio of Field to Torque Phases of Multiphase Induction Machines under BDCE Control	14
3.1 Introduction	14
3.2 Background Information	14
3.2.1 Developed power and torque	14
3.2.2 Inverter currents and stator slot current density	15
3.2.3 Stator copper losses	16
3.2.4 Rotor copper losses	19
3.3 Constructing the Stator Current Waveforms	20
3.4 Machine Dimensions	20
3.4.1 Stator core main dimensions	21
3.4.2 Stator slots and winding	21
3.4.3 Stator slot sizing	21
3.4.4 Rotor slot sizing	21
3.5 MMF Calculations	22
3.6 Finding the Optimal Ratio of Field to Torque Phases	24
3.7 Analytical Results	24

3.8 Finite Element Analysis (FEA).....	26
3.8.1 Air-gap Flux Density.....	27
3.8.2 Rotor Induced Voltage	29
3.9 Summary	29
Chapter 4 Theoretical Analysis of BDCE Controlled Multiphase Induction Machines	31
4.1 Introduction.....	31
4.2 Rotor Voltage Equations	31
4.2.1 Resistance matrix R_r	33
4.2.2 Rotor inductance matrix L_{rr}	33
4.2.3 Mutual inductance matrix L_{sr}	33
4.3 Mutual Inductance Calculation	33
4.4 Instantaneous Bar and End Ring Currents.....	34
4.5 Torque Calculation.....	35
4.6 Simulation Algorithm.....	36
4.7 Finite Element Analysis (FEA) Modelling.....	36
4.8 Theoretical Analysis of a Nine-Phase Induction Machine	38
4.8.1 Nine-phase trapezoidal current waveforms and their mathematical expressions.....	38
4.8.2 MMF generated by the trapezoidal current waveforms.....	41
4.8.3 Air-gap flux density.....	43
4.8.4 Rotor current waveforms.....	45
4.8.5 Torque	47
4.8.6 Rotor copper loss.....	47
4.9 Summary	48
Chapter 5 Design and Test Setup of Experimental Nine-Phase Induction Motor Drive System.....	49
5.1 Introduction.....	49
5.2 Rogowski Coil Current Transducer.....	49
5.3 Nine-phase Induction Machine	50
5.3.1 Stator winding	50
5.3.2 Standard rotor winding.....	52
5.3.3 Special rotor for current measurement	52
5.3.4 Other design and performance parameters.....	54
5.4 Inverter design.....	56
5.4.1 Intelligent power module (IPM).....	56
5.4.2 Control modules and power modules	57
5.4.3 Nine-phase inverter	57
5.4.4 Digital signal processor (DSP) control system.....	58

5.5 Nine-phase Drive System	59
5.6 Experimental Setup	60
5.7 Summary	61
Chapter 6 Calculated and Measured Results	62
6.1 Introduction	62
6.2 Calculated Current Waveforms	62
6.2.1 Rotor circuit loop current waveforms.....	62
6.2.2 Rotor bar current waveforms.....	64
6.3 Measured Current Waveforms	64
6.3.1 Inverter output current waveforms	65
6.3.2 Rotor loop / end ring current waveforms	65
6.3.3 Bar current waveforms	66
6.3.4 Rotor bar current waveform at rated speed	67
6.4 Measured Torque and Efficiency	68
6.4.1 Torque measurements at constant flux	69
6.4.2 Efficiency measurements at constant flux	71
6.4.3 Flux weakening measurements above base speed.....	72
6.5 Ratio of torque to rotor copper losses.....	74
6.6 Summary	75
Chapter 7 Conclusion and Recommendation	76
7.1 Contributions of the study	76
7.2 Conclusions	76
7.3 Recommendations	77
References	78
Appendix A Control of Induction Machines.....	84
A.1 Vector Control.....	84
A.2 Direct Torque Control (DTC).....	85
Appendix B Rogowski coil.....	86
Appendix C Calculation of Resistances and Inductances.....	87
C.1 End Ring Resistance and Inductance Calculation	87
C.2 Rotor Bar Resistance and Inductance	87
Appendix D Digital Hysteresis Controller	89
Appendix A Per Phase Equivalent Circuit	90
E.1 Determination of the x th Equivalent Circuit Parameters	90
E.2 Analysis of the x th Equivalent Circuit	91

List of Figures

Figure 2-1. Geometry of a brush dc machine with salient poles and pole-face compensating windings.	8
Figure 2-2. Geometry of a non-salient round stator machine with compensating windings.	9
Figure 2-3. Trapezoidal six-phase current waveforms [58].	10
Figure 2-4. Current distribution and MMF space phasors at time $t = t_f/2$ [58].	10
Figure 2-5. Current distribution and MMF space phasors when $\alpha = 0$	10
Figure 2-6. BDCE control system operation [58].	11
Figure 2-7. Assumed rotor current with number of field phases equal to the number of torque phases in a six-phase induction machine [58].	12
Figure 3-1. Possible stator current waveform shapes for a BDCE-controlled multiphase induction machine (only half a period of the waveform is shown)	16
Figure 3-2. Single stator phase current waveform torque component.	16
Figure 3-3. $2u^2 - 2u + 1$ function plot.	17
Figure 3-4. Trapezoidal stator current waveform.	20
Figure 3-5. Stator current waveforms, with fifteen stator phases, $m_f = 3$ and $m_t = 12$, <i>a</i>) first group ($z = 1$), and <i>b</i>) second group ($z = 2$).	20
Figure 3-6. Stator slot geometry.	22
Figure 3-7. Rotor slot geometry.	22
Figure 3-8. Dimensions of the machine cores with the magnetic circuit used in the analysis.	24
Figure 3-9. Program flowchart for evaluating m_f/m_t with $I_f = I_t$ and P_n , B , N_p and p set at certain constant values.	25
Figure 3-10. Field plot of 4-pole 15-phase induction machine.	27
Figure 3-11. Air-gap flux density distribution around the air-gap of four pole fifteen-phase induction machine at $t = 0$	28
Figure 3-12. Averaged air-gap flux density at different times of a 4-pole, 15-phase induction machine.	28
Figure 3-13. Air-gap flux density amplitude versus rotating position (4-pole, 15-phase).	28
Figure 3-14. Rotor bar flux linkages with position of field MMF.	29
Figure 3-15. Un-skewed rotor induced bar voltage (stationary rotor and moving stator field).	30
Figure 3-16. Skewed rotor induced bar voltage (moving rotor and stationary stator field).	30
Figure 4-1. Equivalent circuit of a squirrel cage rotor showing rotor loop currents.	31
Figure 4-2. Phase <i>a</i> winding function for a concentrated full pitch winding.	34
Figure 4-3. Winding function of a rotor loop [8].	34
Figure 4-4. Winding distribution of a rotor loop [8].	34
Figure 4-5. Simulation program flow chart, where t is time in seconds, t_{stop} is the time allowed for the simulation to run and x_{max} is a preset value of highest considered stator current harmonic.	37
Figure 4-6. FE model of the nine-phase induction machine	38

Figure 4-7. Nine-phase stator current waveforms.	39
Figure 4-8. Stator winding layout of a 4-pole, 9-phase induction machine.	40
Figure 4-9. Phase <i>a</i> stator current waveform, $i_a(t)$, with $m_f = 3$ and $m_t = 6$	40
Figure 4-10. Per phase stator current waveform ($x = 500$) with its first six harmonics ($I_f = 5.83$ A and $I_t = 5.5$ A). The waveform of the sum of the first six harmonics is also shown.	41
Figure 4-11. MMF waveform produced by a full-pitch single coil for a 4-pole induction machine.	42
Figure 4-12. Phase <i>a</i> stator current waveform with only field current.	44
Figure 4-13. Analytically calculated flux density variation versus time at a position in the air-gap ($x = 1, 3, \dots, 49, v = 1, 3, \dots, 99$).	44
Figure 4-14. Analytically calculated air-gap flux density versus air-gap position ($x = 1, 3, \dots, 49, v = 1, 3, \dots, 99$).	45
Figure 4-15. FEA air-gap flux density versus air-gap position at time $t = 0$ (unskewed rotor).	45
Figure 4-16. An approximate stator current waveform consisting of the first seven harmonics.	46
Figure 4-17. End ring current waveform of the nine-phase induction machine.	46
Figure 4-18. Rotor bar current waveform of the nine-phase induction machine.	46
Figure 4-19. Filtered rotor bar current waveform of the nine-phase induction machine.	46
Figure 4-20. FEA simulated rotor bar current waveform of the 9-phase induction machine.	47
Figure 4-21. Analytically calculated torque of the nine-phase induction machine.	47
Figure 4-22. FEA predicted torque waveform of the nine-phase induction machine (unskewed rotor).	47
Figure 4-23. Rotor copper losses of the nine-phase induction machine calculated by the analytical method.	48
Figure 4-24. FEA calculated rotor copper loss of the 9-phase induction machine.	48
Figure 5-1. Schematic of the Rogowski current transducer.	49
Figure 5-2. Rogowski Coil and integrator box.	49
Figure 5-3. Stator and rotor laminations of an off-the-shelf 11 kW three-phase induction machine. ...	50
Figure 5-4. 9-phase, 4-pole induction machine stator winding layout.	51
Figure 5-5. Stator of the nine-phase induction machine.	51
Figure 5-6. Stator slot geometry.	52
Figure 5-7. Slot shape and dimensions of the standard cage rotor.	52
Figure 5-8. Schematic of the new rotor.	53
Figure 5-9. From left to right: new rotor lamination, lamination holder and end ring.	53
Figure 5-10. Developed rotor without rotor bars.	53
Figure 5-11. Rotor with Rogowski coil fitted on the end ring.	54
Figure 5-12. Relationship between flux density and field current.	54
Figure 5-13. Block diagram of the 6MBP25RA120 IPM.	57
Figure 5-14. Schematic of the IGBT control signals and H – bridge connections.	58

Figure 5-15. The nine-phase inverter block diagram.	58
Figure 5-16. Nine-phase inverter.....	58
Figure 5-17. Functional diagram of the DSP controller.	59
Figure 5-18. DSP controller.	59
Figure 5-19. The nine-phase drive system.	60
Figure 5-20. Test bench setup schematic.	60
Figure 5-21. Nine-phase induction machine on the test bench.....	61
Figure 6-1. Finite element model of a nine-phase induction machine with the special rectangular copper bar cage rotor.	63
Figure 6-2. Waveforms of the analytically calculated consecutive rotor circuit loop currents i_{r1} , i_{r2} and i_{r3} at rotor standstill with the field current, $I_f = 5.83$ A and torque currents equal to a) $I_t = 0$ A, b) $I_t = 2$ A, and c) $I_t = 4$ A. The fundamental frequency of the stator current waveform is 16.67 Hz.	63
Figure 6-3. Analytically calculated and FE calculated rotor bar current at rotor standstill with $I_f = 5.83$ A and torque currents equal to, a) $I_t = 0$ A, b) $I_t = 2$ A, and c) $I_t = 4$ A. The fundamental stator frequency is 16.67 Hz.....	64
Figure 6-4. Measured stator phase current waveforms at rotor standstill with the fundamental stator current frequency at 16.67 Hz, $I_f = 5.83$ A and a) $I_t = 0$ A, and b) $I_t = 4$ A. Note: these waveforms are for demonstration purposes only and have nothing to do with the actual control of the machine.	65
Figure 6-5. Comparison of measured and analytically calculated end ring current waveforms at rotor standstill with the fundamental stator current frequency at 16.67 Hz, $I_f = 5.83$ A and a) $I_t = 0$ A, b) $I_t = 2$ A, and c) $I_t = 4$ A.	66
Figure 6-6. Comparison of measured and calculated rotor bar current waveforms at rotor standstill with the fundamental stator current frequency at 16.67 Hz, $I_f = 5.83$ A and a) $I_t = 0$ A, b) $I_t = 2$ A, and c) $I_t = 4$ A.....	67
Figure 6-7. Different calculated rotor bar current waveforms with the machine running at rated operating speed of 1466 r/min, $I_f = 5.83$ A and $I_t = 5.5$ A. The stator current is at 50 Hz.	68
Figure 6-8. Finite element model of a nine-phase induction machine with the standard cast aluminium cage rotor.....	68
Figure 6-9. Comparison of the measured and calculated torque versus torque current with $I_f = 5.83$ A and $k = 0.638$. The rotor speed for this measurement is 500 r/min.	69
Figure 6-10. Comparison of the measured and calculated torque versus torque current with $I_f = 5.83$ A and $k = 0.638$. The rotor speed for this measurement is 1500 r/min.	70
Figure 6-11. Measured effects of changing the k -value in the drive system on the torque for different values of I_t . The rotor speed for the measurements is 500 r/min.....	70
Figure 6-12. Measured effect of different k -values at 500 r/min.....	71

Figure 6-13. Measured system (converter and motor) efficiency versus percentage load of the nine-phase induction machine drive compared to a conventional three-phase induction machine drive, with (m_f, m_t) a parameter. (Rotor speed = 1500 r/min and at rated dc bus voltage of $V_{dc} = 400$ V)..... 71

Figure 6-14. Measured stator current waveforms at rated flux and rated torque, with (m_f, m_t) a parameter and $k = 0.638$. For (3,6), $I_f = 5.83$ A and $I_t = 5.5$ A, whilst, for (4,5), $I_f = 4.68$ A and $I_t = 6.83$ A. The dc bus voltage for this measurement is, $V_{dc} = 400$ V and the rotor speed is 1500 r/min... 72

Figure 6-15. Relationship between the air-gap flux density, B , control gain, k , and field current, I_f , versus frequency, f 73

Figure 6-16. Measured torque and field current versus the frequency range of the drive..... 73

Figure 6-17. Measured stator current waveforms at 1500 r/min and 3000 r/min. The dc bus voltage for this measurement is $V_{dc} = 400$ V 74

Figure 6-18. 36-slot, nine-phase stator winding layout..... 75

List of Tables

Table 1-1. Multiphase machines having multiples of three phases [19]	3
Table 1-2. Multiphase machines having other than multiples of three phases [19]	3
Table 3-1. 12 phase, 31.4 kW machine parameters.....	18
Table 3-2. Calculated values of I_t , I_f and P_{scu}/R_s	19
Table 3-3. Estimation of stator slot variables.....	22
Table 3-4. Estimation of rotor slot variables.....	22
Table 3-5. Air-gap flux density recommended ranges [69].....	25
Table 3-6. m_f/m_t for a 4-pole, 100 kW induction machine versus number of stator phases.....	26
Table 3-7. m_f/m_t for a 4-pole, 15-phase induction machine versus rated power.....	26
Table 3-8. m_f/m_t for a 6-pole, 15-phase induction machine versus rated power.....	26
Table 3-9. m_f/m_t for an 8-pole, 15-phase induction machine versus rated power.....	26
Table 3-10. Comparison of analytically and FEA calculated air-gap flux densities calculated for determined m_f/m_t for a 4-pole 15-phase induction machine with varying rated power.	27
Table 4-1. Machine parameters of a 4-pole 9-phase induction machine.....	39
Table 5-1: General design data.....	51
Table 5-2. Stator slot variables.....	52
Table 5-3. Nine-Phase Machine Data.....	56
Table 6-1. Rated torque with $I_f = 5.83$ A, $I_t = 5.5$ A and $k = 0.638$ at a rotor speed of 1466 r/min.....	70
Table 6-2. Comparison of the ratio of torque to rotor copper losses for different windings and different current waveform supplies.	75

Nomenclature

Variable definitions

Symbol	Description	Unit
A	cross sectional area of a rotor slot	[m ²]
a	number of parallel circuits	[#]
B	air gap flux density	[m]
d_r	rotor diameter	[m]
d_s	stator outer diameter	[m]
d_{si}	stator inner diameter	[m]
E_b	amplitude of the induced bar voltage	[V]
E_s	amplitude of the induced stator phase voltage	[V]
f	stator current fundamental frequency	[Hz]
F_f	amplitude of the stator field MMF produced by mf field phases	[A-turns]
F_r	amplitude of the rotor air-gap MMF	[A-turns]
F_t	amplitude of the stator torque MMF produced by mt torque phases	[A-turns]
g	air-gap length	[m]
I_{2x}	x th harmonic rotor current referred to the stator	[A]
I_a	armature current	[A]
I_b	rotor bar current	[A]
i_{ds}	direct axis component of the armature / stator currents in a synchronously rotating reference frame	[A]
i_d^* and i_q^*	control currents in the synchronously (dq) rotating reference frame	[A]
I_f	stator field current amplitude	[A]
I_{mx}	x th harmonic magnetizing current	[A]
i_{qs}	quadrature axis components of the armature / stator currents in a synchronously rotating reference frame	[A]
\mathbf{I}_r	rotor loop currents vector	[A]
\mathbf{I}_s	stator current vector	[A]
I_t	stator torque current amplitude	[A]
I_x	x th harmonic current	[A]
J	current density	[A/mm ²]
k	control gain	[(rad/s)/A]
k_{fill}	fill factor	[#]
K_s	stacking factor	[#]
l	stack length	[m]

L_{er}	end ring inductance	[H]
l_i	average length of the end ring segment	[m]
\mathbf{L}_{rr}	rotor inductance matrix	[H]
\mathbf{L}_{rs}	mutual inductance matrix between rotor loop circuits and stator phases	[H]
L_{slot}	per unit length slot inductance	[H]
\mathbf{L}_{sr}	mutual inductance matrix between stator phases and rotor loop circuits	[H]
m_f	number of field phases per pole	[#]
M_r	total number of rotor slots	[#]
m_{ra}	number of active rotor bars or phases per pole	[#]
M_s	total number of stator slots	[#]
m_t	number of torque phases per pole	[#]
N_p	number of stator phases	[#]
N_r	number of turns per rotor phase, $N_r = 0.5$ for squirrel cage	[#]
N_s	number of turns in series per stator phase	[#]
p	number of pole pairs	[#]
P_n	rated power	[W]
q	number of phase belts per pole	[#]
R_{2x}	xth rotor resistance	[Ω]
R_{ac}	ac resistance	[Ω]
R_{dc}	dc resistance	[Ω]
R_e	end ring resistance	[Ω]
r_g	air gap radius	[m]
R_b	dc bar resistance	[m]
\mathbf{R}_r	resistance matrix	[Ω]
R_{slot}	per unit length slot resistance	[Ω]
S_A	copper area in a stator slot	m ²
s_x	xth per unit slip	[#]
T	torque of the machine	[Nm]
V_{dc}	dc bus voltage	[V]
\mathbf{V}_r	rotor loop voltage vector	[V]
X_{2x}	xth rotor reactance referred to the stator	[Ω]
X_{mx}	xth magnetizing reactance	[Ω]
θ	electrical angle	[rad]
θ_r	rotor position	[rad]
$\mathbf{\Lambda}_r$	rotor loop flux linkages matrix	[Wb-turn]

μ_0	absolute permeability	[H/m]
ρ	resistivity of the bar material at a particular temperature	[Ωm]
ω	synchronous speed	[rad/s]
ω_r	rotor speed	[rad/s]
ω_{sl}	slip speed	[rad/s]

Abbreviations

ADC	Analog to Digital Converter
BDCE	Brush-dc Equivalent
D/A	Digital to Analog Converter
DSP	Digital Signal Processor
DTC	Direct Torque Control
EPLD	Electrically Programmable Logic Device
FEA	Finite Element Analysis
FPGA	Field Programmable Gate Array
IGBT	Insulated-gate Bipolar Transistors
IM	Induction Machine
IPM	Intelligent Power Module
MMF	Magneto-motive Force
PCB	Printed Circuit Board
PWM	Pulse Width Modulation
VSI	Voltage Source Inverter

Constants

$$K_s = 0.95$$

$$k_{fill} = 0.5$$

$$\mu_0 = 4\pi \times 10^{-7} \text{ H/m}$$

$$J = -3.0P_n + 6 \times 10^6 \text{ A/mm}^2$$

$$\rho_{Al} = 2.63 \times 10^{-8} \Omega\text{m} \text{ (aluminium resistivity)}$$

$$\rho_{Cu} = 1.7 \times 10^{-8} \Omega\text{m} \text{ (copper resistivity)}$$

Chapter 1

Introduction

The three phase induction machine is widely used in industry today due to its robustness, reliability, low cost and low maintenance. The introduction of the inverter in the control of the induction machine in the last century led to the consideration of induction machines with more than three phases. These types of machines are called multiphase induction machines. Increasing the number of stator phases in an induction machine drive lead to the following benefits [1], [2], [3], [4], [5], [6], [7], [8];

- reduction of the amplitude of the torque pulsation and the increase of the torque pulsation frequency,
- reduction in rotor harmonic currents and reduction in the current per phase without increasing the voltage per phase (since the number of phases increase),
- decrease in the dc link current harmonics,
- increase in machine power and torque per rms current for the same volume machine,
- use of lower rated semiconductor switches as the power is split across a number of inverter legs,
- better fault tolerance and higher reliability,
- depending on the stator winding, other advantages are: independent control of multimotor multiphase drive systems with a single power electronic converter supply and torque enhancement through stator current harmonic injection, and,
- improvement of the quality of the air-gap flux density waveform regardless of the current waveform or winding design, because with a higher phase number there is less interaction between space and time harmonics.

At present, multiphase induction machines are used in highly specialized applications such as locomotive traction, electric and hybrid-electric vehicles, industrial high power applications, electric ship propulsion [3], [9] and the more electric aircraft [10], [11], [12]. Battery powered applications such as cordless power tools and small traction drives are also considered [13].

1.1 Background on Multiphase Induction Machines

In this section, a literature review summary of the work done on multiphase induction machines is presented. In 1969, Ward and Harer [14] built and tested a five-phase inverter fed induction motor. Their choice of a five-phase induction motor was based on their argument that the performance of a motor with even number phases is inferior to that of a motor with odd number phases. The reason given for that was that the poles of a motor, with even number of phases, coincide in pairs and thus it has a torque pulsation with frequency and amplitude of a machine with half its phases. They found that increasing the number of phases leads to the reduction of the torque pulsations, whilst the frequency of the torque pulsation increases. Also in 1969, McLean *et al* [7] analyzed the performance of induction motors with a square-wave voltage supply. They developed an analysis method using harmonic travelling current-density waves, together with design methods for square-wave excited induction motors with comparable efficiency and output to sinusoidally fed induction motors, to evaluate the performance of the induction machines with square-wave voltage supply. The performance of a prototype nine-phase induction motor was compared to that of a three-phase motor. It was shown that increasing the number of phases and utilizing fully pitched coils improves the electrical efficiency. A developed prototype square-wave fed nine-phase machine was shown to give identical performance to a similar sinusoidally fed three-phase machine. Similarly to Ward and Harer, they found that the

torque pulsating frequency at a given supply frequency increases with an increase in the number of phases.

In the seventies, Nelson and Krause [15] found through computer simulation that six-phase induction motors with 30° phase belts can be used to eliminate the sixth harmonic torque that is normally found in inverter driven three-phase motors. This type of machine has since been known as a dual three-phase induction machine where the stator winding is formed through two different sets of three-phase windings. Jahns [16] proposed multiphase induction machine drives with a high degree of reliability whereby the machine can be started or continue running with reduced torque and increased losses. He proved that the performance of the machine when one phase is open or shorted is improved when the total number of phases is increased.

Characteristics of multiphase machines and experimental results of a six-phase and nine-phase induction machine were presented by Klingshirn [17]. He verified that multiphase machines perform similarly to three-phase machines when supplied by a balanced sinusoidal source, and the increase in the number of phases led to better fault tolerance. Also, multiphase machines with non-sinusoidal voltage sources, have higher stator copper losses due to harmonics and low rotor copper loss, whilst those with non-sinusoidal current sources generally have low copper losses when compared to three-phase machines. The harmonics in non-sinusoidal excited machines were found to reduce torque pulsations. Further investigations of the five-phase induction machine drive were carried out by Pavithran *et al* [18]. The authors presented theoretical and experimental studies showing that a five-phase drive can operate with nearly sinusoidal currents in the pulse width modulation (PWM) mode of operation. In the following sub-sections, a general classification of multiphase induction machines and a summary of the work done on the control of the multiphase induction machine are presented.

1.1.1 Classification and winding layouts

A method of classifying multiphase induction machines proposed by Klingshirn [19] is presented in this section. Generally, for any machine, the number of stator terminals excluding the neutral is equal to the number of phases. It is not adequate to describe a multiphase induction machine by giving only the number of phases since two machine versions are possible based on two possible values of the phase belt angle for a given number of phases. For example, three phase motors with 60° phase belts have some different characteristics when compared to three phase motors with 120° phase belts. The number of phase belts per pole, q , is given by,

$$q = \frac{180}{\beta}, \quad (1-1)$$

where β is the phase belt angle in electrical degrees.

Table 1-1 and Table 1-2 provide a useful description of multiphase machines based on the phase belt angle and the minimum number of stator terminals required. The connection diagrams are also shown in the tables.

A symmetrical stator winding has equal spatial displacement between any two consecutive phases and this is always the case for machines where the number of phases is an odd prime number. That is, the spatial displacement between consecutive stator phases of an m -phase machine is

$$\alpha = \frac{2\pi}{m}. \quad (1-2)$$

For an asymmetrical stator winding, the spatial displacement between consecutive winding is not equal. This is because the winding is formed by different windings which are made of sub-phases. Therefore, an m -phase winding is formed by w windings having i sub-phases, where typically, $w = 2, 3, 4 \dots$ and $i = 3, 5$. Then the spatial displacement between the first phases of two consecutive sub-phase windings is

$$\alpha = \frac{\pi}{m} . \quad (1-3)$$

The stator winding can either be concentrated or distributed depending on the number of phases and stator dimensions. The stator circumference can only have a limited number of slots, and therefore it becomes difficult to have a distributed winding as the number of phases increase.

Table 1-1. Multiphase machines having multiples of three phases [19]

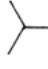
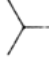



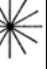




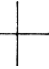






Phase belt angle, degrees (β)	120	60	60	40	30	30	20	20
number of phase belts per pole (q)	1.5	3	3	4.5	6	6	9	9
number of stator terminals(minimum)	3	3	6	9	6	12	9	18
Connection name	Three-Phase	Semi Six-Phase	Six-Phase	Nine-Phase	Semi 12-Phase	12-Phase	Semi 18-Phase	18-Phase
Schematic diagram of star connection and voltage phasor diagram. (Mesh connection may be used also)								
Alternate diagram or common name		Three-Phase						

Table 1-2. Multiphase machines having other than multiples of three phases [19]

Phase belt angle,degrees (β)	90	90	45	45	36	25.71	18	18
number of phase belts per pole (q)	2	2	4	4	5	7	10	10
number of stator terminals(minimum)	3	4	5	8	5	7	5	10
Connection name	Semi 4-Phase	4-Phase	Semi 8-Phase	8-Phase	5-Phase	7-Phase	Semi 10-Phase	10-Phase
Schematic diagram of star connection and voltage phasor diagram								

1.1.2 Control of multiphase induction machine systems

Generally, the control techniques used in three-phase induction machine drives are modified and developed for the control of multiphase induction machines. Scalar control with voltage or current source inverters was used in the control of multiphase induction machines in the late sixties to the early nineties of the last century [14], [18], [20]. Currently, vector control and direct torque control (DTC) methods have taken centre stage in research and applications since the cost of multiphase power electronics is higher compared to the cost of implementing control algorithms [21]. Both these methods rely on mathematical models of the machine.

A general modelling procedure for symmetrical induction machines with a sinusoidally distributed stator winding is found in [22]. The distributed winding assumption allows the omission of higher spatial magneto-motive force (MMF) harmonics in the mathematical modelling. The number of phases

can be either odd or even and the windings are connected in star with a single neutral point. Nelson and Krause [15] presented an analysis method for studying multiphase induction machines with symmetrical or unsymmetrical phase displacement. A dq model for an inverter-fed dual three-phase machine drive system is presented by Lipo [23], and Abbas et al [24]. These modelling methods are widely used in the literature today and form the basis for the development of new methods. An analysis method using the winding function approach for modelling the multiphase cage induction motor was developed by Toliyat and Lipo [8], [25], [26]. The model has been used successfully to simulate machine faults such as asymmetry in the stator, air-gap eccentricity and rotor bar faults [27], [28]. Recently, bifurcation analysis of concentrated and distributed winding induction machines with third harmonic injection was presented by Duran *et al* [29].

The basic operation of vector control and DTC of three-phase machines is explained in Appendix A. Theoretically, the same vector control schemes used in the control of three-phase induction machines are applicable to symmetrical multiphase machines regardless of the number of phases. Here, the co-ordinate transformation has to produce the required stator current or voltage references. Some applications of vector control of multiphase induction machine drives include [5], [6], [30], [31], [32], [33], [34], [35], [36], [37], [38]. Similarly, the same techniques for DTC of three-phase induction machines drives can be appropriately used in multiphase induction machines drives. DTC improves the operating characteristics of the motor and the voltage source inverter through the control of the stator flux and the torque, instead of controlling the current [39]. The DTC principle is based on instantaneous space vector theory. Simultaneous and decoupled control of torque and stator flux is achieved by optimal selection of space voltage vectors in each sampling period in accordance with the torque and flux errors. Then, the performance of a DTC scheme is directly affected by the number of space vectors and switching frequency. Results have shown that DTC of multiphase induction machine drives can achieve higher performance [39], [40], [41], [42], [43], [44]. The vector control and DTC of a five-phase induction motor are compared in [45]. The authors showed that by utilizing current injection, vector control provides the desired nearly rectangular current and flux waveforms, and DTC results in a significant reduction of torque and stator current ripples. The complexity of the vector control and DTC algorithm increases as the number of phases increases [2].

In induction machine drives utilising vector control and DTC, the pulse width modulation (PWM) scheme employed by the voltage source inverter should be carefully selected. Sophisticated space vector PWM and carrier-based PWM techniques are required in the voltage source inverter control of multiphase induction machines. Newer PWM schemes are being introduced such as in [46], [47], [48], [49], [50],[51], [52]. Comparison of carrier-based PWM and space vector PWM shows that space vector PWM becomes more and more complex with increasing phase number [53], [54]. Theoretical and simulation consideration of multilevel voltage source inverters for multiphase machines are given in [55], [56]. A space vector PWM algorithm for multilevel multiphase voltage source inverters with switching state redundancy is presented in [57].

Finally, in [58] a completely different control method for multiphase induction machines is proposed and evaluated. Trapezoidal phase current waveforms that make it possible to have separate field and torque stator currents are introduced. These current waveforms generate a rotating nearly square air-gap flux density that allows control of a multiphase induction machine that is similar to that of a dc machine. In this method, each stator phase acts as either a torque or a flux producing phase. In this dissertation, the method is termed the “brush-dc equivalent” (BDCE) control method and its principle of operation is described in Chapter 2.

1.1.3 Voltage source inverter current control

Current control in voltage source inverter drives has been studied extensively and developed in the literature on three-phase systems. In multiphase voltage source inverter drive systems, the current control technique is very important as it has to relate to the particular system. Three-phase current control methods in voltage source inverters are adapted and employed on asymmetrical multiphase systems, have to cope with unbalanced currents, machine asymmetries and large harmonic currents [14], [24], [59]. Lyra and Lipo [6] proposed a current control scheme that considers third harmonic current injection. A current control scheme in stationary $\alpha\beta$ reference frame that does not require

decoupling circuits and can cope with current imbalances between arbitrary three-phase stator winding sets, is proposed in [32]. Model-based predictive control employed on asymmetrical multiphase drives is proposed and analyzed in [60]. It is shown that this method avoids the use of complex controllers and modulation techniques at the expense of an increased computational cost [60]. Theoretically, in the synchronous reference frame, only two current controllers are used to realize rotor-flux-oriented control of multiphase induction machines with sinusoidal MMF distribution. However, in practice, this is not sufficient as shown in [61]. A modified current control scheme was experimentally verified and shown to provide operation of the machine with a practically perfectly sinusoidal and balanced system of phase currents [61]. Hysteresis current control is used in [58].

1.2 Rotor Current Measurements

This section presents work done on the measurement of the rotor bar current in induction machines. It is essential to measure the rotor bar and end-ring currents in order to verify the theory of induction machines. A method of measuring the real-time rotor bar current, using a Rogowski coil, whilst the machine is moving, is presented in [62], [63]. Here, Bluetooth wireless technology is employed in the transmission of the measured rotor current data to a logging computer whilst the rotor is moving. In [64], rotor bar current measurements were made on an appropriately made cage induction motor using Hall sensors. The low cost, lower weight, good frequency response and ease of installation of the Rogowski coil makes it ideal for a number of current measurement applications [65]. Appendix B provides details of the Rogowski coil. Other advantages of the Rogowski coil are: very high bandwidth, capability to measure large currents with the same size coil, isolation and good linearity due to absence of magnetic materials [66].

1.3 Objectives of the Study

The application of the BDCE control method is evaluated theoretically and experimentally by Ai et al [58]. Finite element analysis is used in the theoretical evaluations, whilst a six-phase wound rotor induction machine is used in the experimental evaluations. The control technique is shown to produce remarkable results, whilst it is simpler than transformation-based control techniques. The presented six-phase induction machine has three field and three torque phases active at any time instance. That is, the number of field phases and torque phase are equal, and, therefore the ratio of the number of field to number of torque phases is one. This theoretically leads to underutilisation of the rotor windings since only half of the rotor phase windings are active and the other half remain idle at each time instance. Other combinations of field and torque phases are not considered. Also, the rotor phase current waveform has not been analytically evaluated. The measured rotor phase current waveform given by [58] contradicts the assumed square-like current waveform.

It is clear from the previous paragraph, that, there are questions that still need to be answered on the new control technique. These questions include:

- What is the best (optimal) ratio of the number of field phases to the number of torque phases of the multiphase induction machine drive utilising the BDCE control technique?

An answer to this question will lead to different trapezoidal stator current waveforms that need to be determined.

- What is the performance of the BDCE-controlled multiphase machine drive when a cage winding is implemented on the rotor?

In [58], the control principle is evaluated on a wound-rotor, six-phase induction machine. However, the principle is applicable to large drives involving cage rotor induction machines. Therefore, the performance of a cage rotor induction machine, under trapezoidal stator current waveforms excitation, needs to be evaluated. This includes the investigation of the losses in the rotor bars resulting from the application of the trapezoidal stator current waveforms. The performance of the proposed BDCE-drive, thus, needs to be evaluated both analytically and experimentally.

- What is the shape of the rotor bar current waveform?

The rotor current waveform affects the performance of an induction machine. The instantaneous torque of the machine together with rotor copper losses can be calculated from the rotor current waveform. In order to enhance the design process of multiphase induction machines supplied with trapezoidal stator current waveforms, a theoretical evaluation of the current waveform is needed. Experimental evaluation should also be carried out to confirm the theory.

The objective of this dissertation is to answer these questions on BDCE controlled multiphase induction machine drives. The dissertation, thus, seeks to provide a further step in the possible application of the BDCE control method

1.4 Dissertation layout

The layout of the remainder of the dissertation is as follows:

- Chapter 2: In this Chapter, the conceptualisation and the principle of operation of the BDCE control method is presented. It is followed by a summary of the results obtained by Ai et al [58].
- Chapter 3: Analytical expressions of the developed power, torque, stator and rotor copper losses are presented in this Chapter. The analytical method of calculating the optimal ratio of field to torque phases is also presented together with analytical results. Finite element analysis results from a non-commercial software are also given.
- Chapter 4: A description of an analytical method of evaluating the performance of a multiphase induction machine is given. Theoretical and finite element analysis results are given based on an arbitrary chosen nine-phase induction machine. The evaluated results: the rotor current waveform, the torque and rotor I^2R (copper) losses of the machine.
- Chapter 5: A detailed description of a nine-phase induction machine drive prototype is presented with its test setup. The design and specifications of each component is given in this Chapter.
- Chapter 6: Measurement results of a nine-phase induction machine drive are presented and compared to theoretical and finite element results.
- Chapter 7: In this Chapter, conclusions are given and recommendations are made for further study.

Chapter 2

Brush-DC Equivalent (BDCE) Control Method

In this Chapter, background theory of separately excited dc machines with compensating windings is presented. From this theory, the principle of operation of the so-called direct flux and direct torque control method proposed in [58] for multiphase induction machine drives is explained. Understanding of how this technique works is essential since the dissertation focuses on furthering the work done in [58]. The control system is also explained and a summary of the results obtained in [58] is given. In this dissertation, the description of the drive as a “direct flux and direct torque controlled” drive is avoided as “direct flux control (DFC)” and “direct torque control (DTC)” are well-known control methods used in conventional induction machine drives, as explained in Appendix A. Instead, the type of drive proposed by [58] and considered in this dissertation is rather referred to as a “brush-dc equivalent” (BDCE) multiphase induction machine drive.

2.1 Background on Brush-DC Machines with Compensating Windings

A schematic picture of a separately excited dc machine is shown in Figure 2-1 with the armature winding on the rotor. The current into the armature winding is fed through a brush or commutator system, whilst the field winding of the stator provides the magnetic field. The field and armature circuits are controlled separately. Assuming that the average of the air-gap magnetic flux density is B , then the torque, T , generated by the machine as derived in all classical text books on brush-dc machines is given by

$$T = M_{ra} r_g l B I_a, \quad (2-1)$$

where, M_{ra} is the number of conductors underneath the poles at any time instance (number of active conductors), r_g is the rotor radius, l is the rotor length and I_a is the armature conductor current. Also, assuming the permeability of iron to be infinitely high, the flux density is given by,

$$B = \frac{\mu_o N_f I_f}{g}, \quad (2-2)$$

where, N_f is the number of field turns per pole, I_f is the field current and g is the air-gap length. Therefore, from (2-1) and (2-2),

$$\begin{aligned} T &= M_{ra} r_g \frac{\mu_o N_f I_f}{g} I_a \\ &= K I_f I_a, \end{aligned} \quad (2-3)$$

where K is a machine constant.

Since brush dc machines are highly salient, the analysis above ignores, as a good approximation, the effect of the armature reaction flux, which is in quadrature with the main field flux. Though much less than the field flux, the armature flux causes a drop in the main field flux per pole due to the saturation of the one side of the iron field poles. This drop in flux per pole causes a drop in the average air-gap flux density, B , so that the torque per current of the machine drops, which is detrimental to the performance of the machine. A compensating winding, as shown in Figure 2-1, can be used to obtain a more uniform air-gap flux distribution and to mitigate the saturation effect due to the armature reaction flux. The compensating coils are mirror images of the armature coils and have the same number of ampere-turns as the armature. In practice, if the compensating coils have the same number of turns as the armature coils, they are connected in series with the armature coils. The function of the

compensating coils is to cancel the flux produced by the armature coils, thus leaving only the flux produced by the field winding.

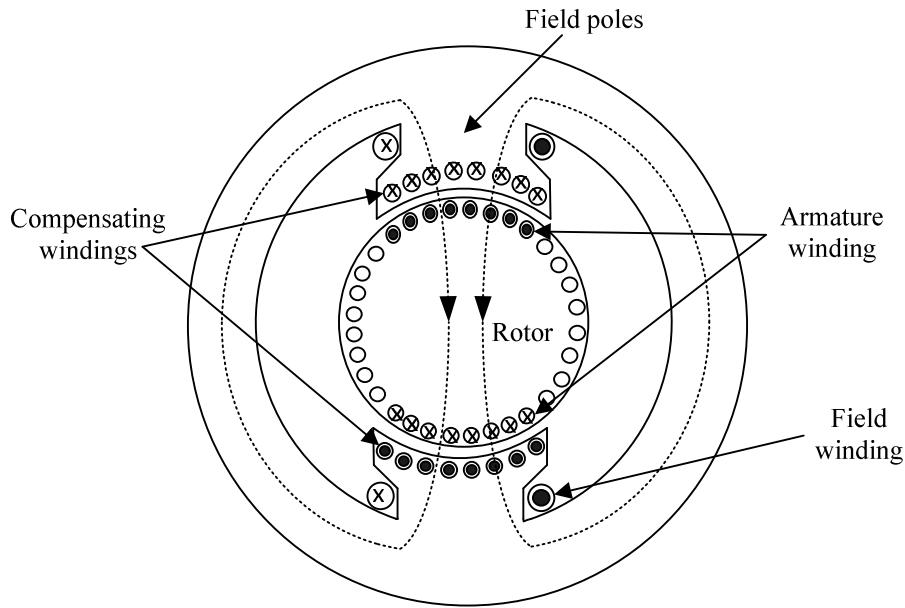


Figure 2-1. Geometry of a brush dc machine with salient poles and pole-face compensating windings.

2.2 Conceptualisation of the BDCE Operation of Multiphase Induction Machine

Machine

Starting with Figure 2-1, the dc machine can be transformed to that as shown in Figure 2-2. Here, the salient stator of the dc machine is transformed to a round stator of an induction machine. The field windings are shifted as shown whilst the compensating windings become the torque windings at a particular instance as shown. In the multiphase induction machine, the compensating (torque) windings are replaced with individual coils that become a group of torque phases and the field windings are replaced with independent coils that become a group of field phases as shown in Figure 2-2. All the windings (field and torque) are placed in evenly spaced identical slots on a non-salient round stator and the number of turns is maintained the same in all the stator slots. The armature winding is replaced with a cage (or wound rotor) winding.

For the induction machine to operate, stator current waveforms and a stator winding layout that allow a phase to alternate between being a field producing phase and a torque producing phase are constructed. At each time instance, a group of phases are to act as field producing phases and the rest as torque producing phases. The flux produced by the field producing phases leads to induced voltages at slip speed in the rotor bars located under the torque phases. Then, the rotor phase currents will flow in the cage or shorted wound rotor winding under the torque phases and produce a flux in quadrature to the main flux. The torque current flowing in the torque phases must then produce a counter MMF to balance the MMF due to the rotor current similarly to the compensating winding in dc machines. The stator waveforms when applied to a properly designed stator winding layout are to produce a moving rectangular air-gap flux density when the rotor MMF is cancelled by the MMF produced by the torque winding at each instance. Thus, torque in the machine is produced similarly as in dc machines with compensating windings. In the next sections, the stator current waveforms and the control method developed in [58] for a two pole BDCE six-phase wound rotor induction machine, are presented.

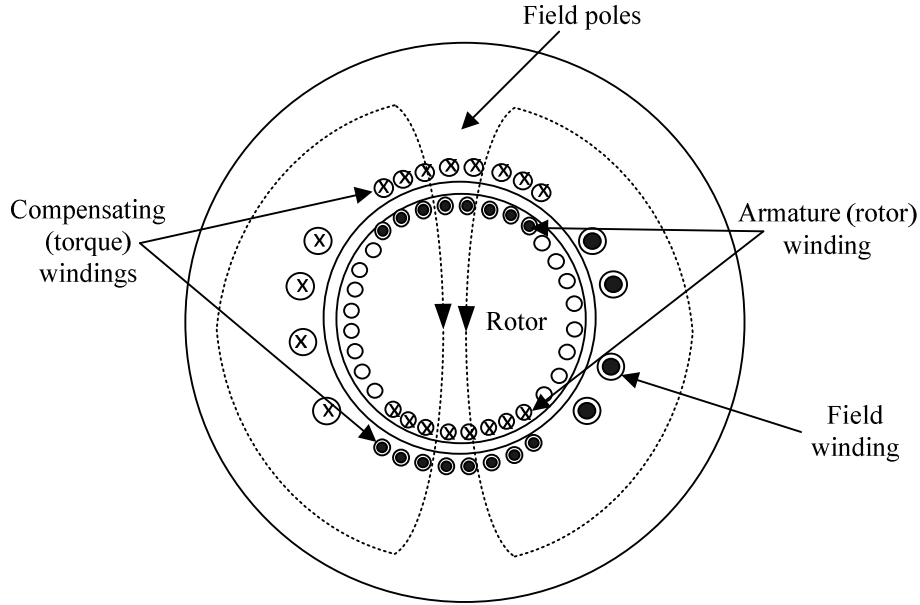


Figure 2-2. Geometry of a non-salient round stator machine with compensating windings.

2.3 Principle and Description of BDCE Multiphase Induction Machine

Drive

The principle of operation of the BDCE multiphase induction machine drive is best explained graphically. The configuration of the stator phase current waveforms shown in Figure 2-3 allows separate rotating flux or field MMF with an amplitude, F_f , and torque MMF with an amplitude, F_t , in a two pole six-phase induction machine. In the figure, it is shown that the stator phase current consists of trapezoidal-shaped field and torque current components, with flat-topped amplitudes of I_f and I_t respectively. That is, a stator phase acts alternately in time as either a flux or a torque producing phase. Furthermore it can be seen from Figure 2-3 and Figure 2-4 that at any instant there are always three neighbouring stator phase windings that act as field windings to generate the flux in the machine whilst the other three neighbouring stator phase windings always act as torque windings to generate the torque of the machine. The generated flux in the machine will lead to induced rotor phase voltages at slip speed and currents will flow in the rotor phases. Then, the rotor currents produce the rotor MMF, F_r , which in turn affects the air-gap flux density. The torque current flowing in the torque producing phases produces a counter MMF that balances the rotor MMF during operation of the BDCE multiphase induction machine. Figure 2-5 is obtained from Figure 2-4, with $F_t = F_r$ and $\alpha = 0$ for balanced MMF condition (flux decoupling condition). There is, thus, an important relationship between the torque current, I_t , and the angular slip frequency, ω_{sl} , for balanced MMF control (or decouple control), that is,

$$k = \frac{\omega_{sl}}{I_t}, \quad (2-4)$$

where k is called the control gain. The control gain depends on physical dimensions of the machine, the total number of phases, the rotor phase resistance and the air-gap flux density. The relationship (2-4) is used in the control system of the drive.

Figure 2-6 shows a block diagram of a six-phase induction machine drive with its control system. Similarly to [67] and phase redundant multiphase systems [1], a full bridge inverter is used for each stator phase winding, which results in twelve phase legs for the drive. For this, four three-phase power inverter modules are used to complete the six-phase full bridge inverter. The rotor speed together with the phase currents of the drive are measured and fed back to a digital signal processor (DSP)

controller. The field current is kept constant and the torque command-current is controlled by the speed controller. The speed controller controls the torque command-current I_t , from which the slip angular frequency ω_{sl} is determined using the control gain. From this and from the known field command current I_f , the six reference phase currents of the drive are generated. A digitally implemented hysteresis current regulator, using a field programmable gate array (FPGA), is used for the current control. The switching signals are sent to the inverter via fibre optic cables. The advantage of this method is that it does not require any transformations such as in vector control and DTC.

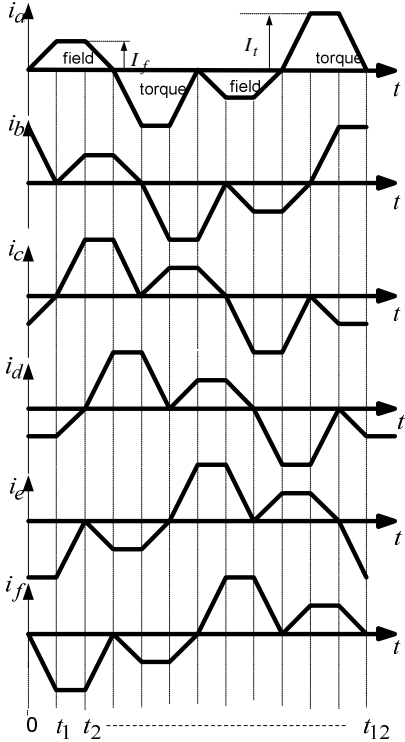


Figure 2-3. Trapezoidal six-phase current waveforms [58].

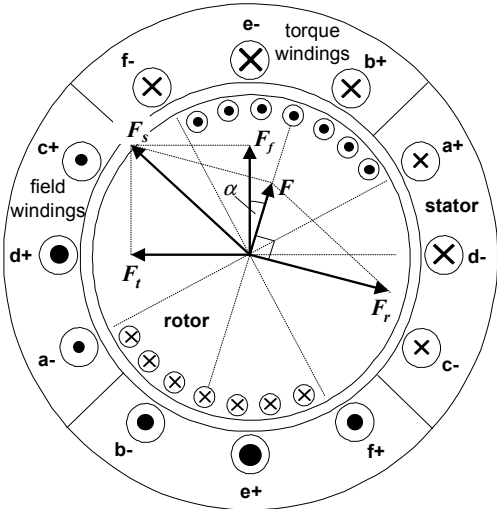


Figure 2-4. Current distribution and MMF space phasors at time $t = t_1/2$ [58].

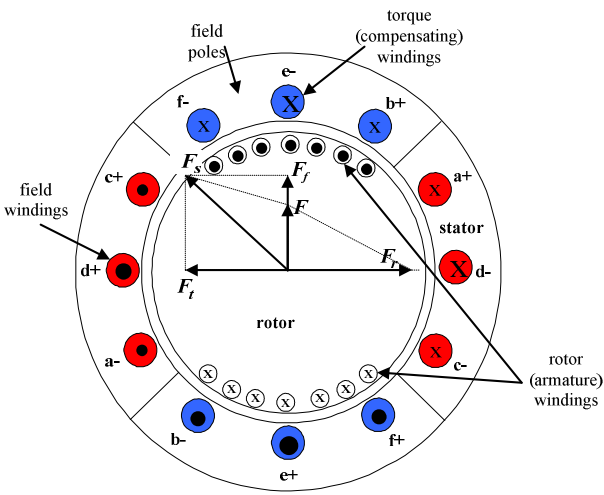


Figure 2-5. Current distribution and MMF space phasors when $\alpha = 0$.

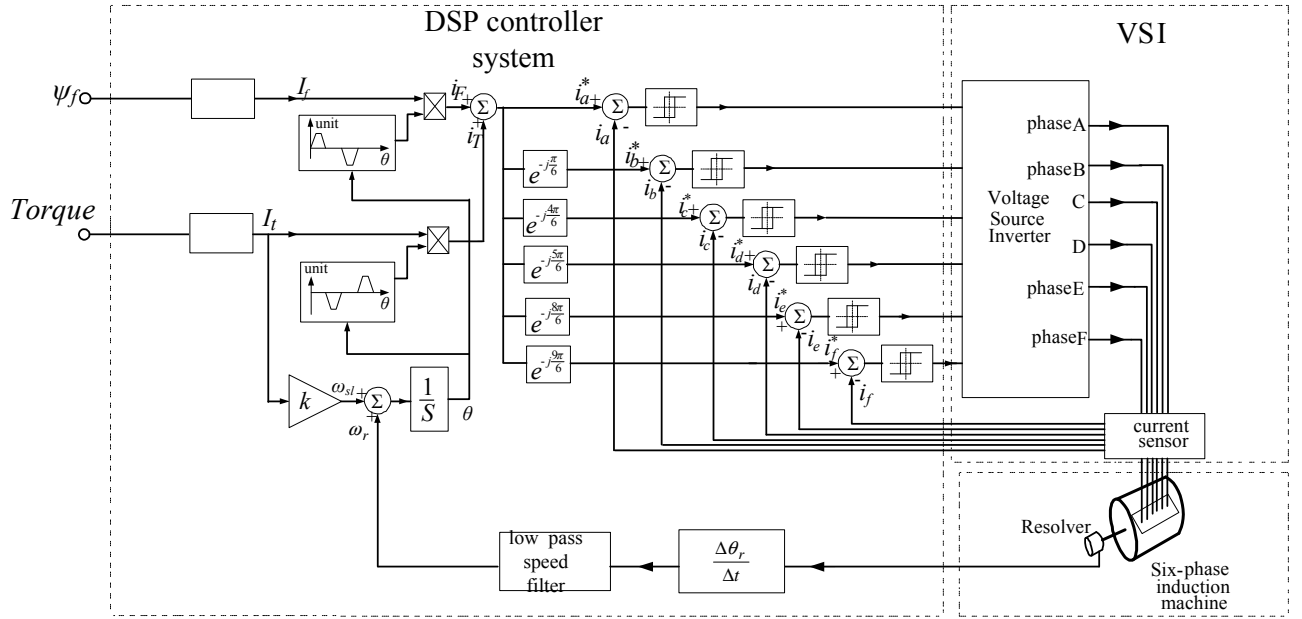


Figure 2-6. BDCE control system operation [58].

2.4 Analysis of a BDCE Six-Phase Induction Machine

From Figure 2-3 to Figure 2-5, it is clear that, at any time instance, the amplitude of the field MMF, F_f , is

$$F_f = 2N_s I_f. \quad (2-5)$$

where N_s is the number of turns per phase. Similarly, the amplitude of the torque MMF is

$$F_t = 2N_s I_t, \quad (2-6)$$

In the analysis, assuming perfect commutation and quasi-square-wave air-gap flux density, the induced rotor phase current waveform will have an ideal square-like form as shown in Figure 2-7. With the position of the active rotor phase windings opposite the position of the compensating or torque phase winding of the stator, the rotor MMF amplitude is given by

$$F_r = m_{ra} N_r I_r, \quad (2-7)$$

where, m_{ra} is the number of conductors or rotor phases underneath a pole at any time instance and N_r is the number of turns per rotor phase. Theoretically, the number of active bars per pole is

$$m_{ra} = \frac{M_r (m_t - 1)}{2N_p p}, \quad (2-8)$$

where M_r is the number of rotor bars, m_t is the number of torque phases, N_p is the total number of stator phases and p is the number of pole pairs.

The rotor phase winding or bar induced voltage waveform assumes a nearly square due to the quasi-square air-gap flux density. The flat-topped amplitude of this waveform can be calculated similarly to that of dc machines as

$$E_b = 2N_r B l \omega_{sl} r_g, \quad (2-9)$$

where ω_{sl} is the angular slip frequency, B is the air-gap flux density, l is the stack length, and r_g is the air-gap radius. The induced rotor phase current is the,

$$I_r = \frac{E_b}{R_b} = \frac{2N_r B l \omega_{sl} r_g}{R_b}, \quad (2-10)$$

where R_b is the rotor phase resistance. Using Lorentz force law, similarly to the brush dc machine case, the electromagnetic torque of the machine is given by,

$$T = 2m_{ra} N_r r_g l B I_r. \quad (2-11)$$

Under balanced MMF conditions ($F_t = F_r$), using (2-6), (2-7) and (2-11) it can be shown that

$$T = 4N_s r_g l B I_t. \quad (2-12)$$

Thus, there is a linear relationship between torque and torque current similarly to (2-3).

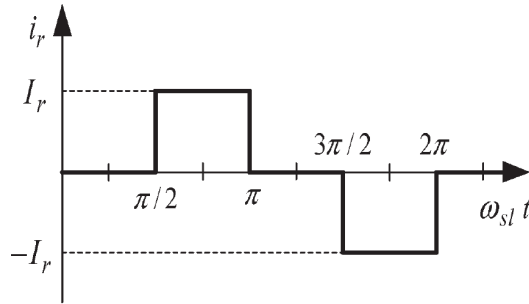


Figure 2-7. Assumed rotor current with number of field phases equal to the number of torque phases in a six-phase induction machine [58].

2.5 Summary and Conclusions

In this section, a summary of the findings of [58] is given. In [58], measured and analytically calculated results of rotor induced voltage, air-gap flux density, torque, dynamic performance and induced rotor current of a BDCE six-phase induction machine drive are presented. From the balanced MMF condition assumption, an analytical expression of the static torque of the machine is derived through the application of Lorentz force law.

The measurements are performed on a modified two pole six-phase wound rotor induction machine. It is found that the proposed stator phase current waveforms generate a nearly square-shape rotating air-gap flux density. A linear relationship between the rotor induced voltage and the slip speed is verified through measurements and analysis. The drive controller is shown to maintain a linear relationship between the torque and torque current: therefore, showing MMF balance in the machine. Fast torque response of the drive is obtained. However, the stator phase current waveforms led to a high frequency ripple on the back electro-motive force. This may have a negative effect on the efficiency and may increase torque ripple.

The control gain, k , is calculated and found to depend on the flux density and the rotor phase resistance of the machine. Since the flux density is controlled through the field current and the rotor phase resistance varies with temperature (about 40 %), it is possible to have a wrong value of k in the

control system during operation of the machine. Analytical and measurement results in [58], show that the torque of the machine is sensitive to a change in the control gain.

Results showed that the assumed rotor phase current waveform differs from the measured rotor phase current waveform. However, the principle of operation of the six-phase induction machine, with the assumed rotor current waveform, is proved to produce remarkable results through analysis and measurement. It is clear that the control method is not restricted only to six-phase induction machines, but, it can be expanded to other multiphase induction machines.

Chapter 3

Optimal Ratio of Field to Torque Phases of Multiphase Induction Machines under BDCE Control

3.1 Introduction

In [58], the total number of phases are equally divided between torque and field phases ($m_f/m_t = 1$), but, the question is: is this ratio necessarily the best in terms of losses and inverter rating for a machine with a certain torque and certain flux density? In this Chapter, this question is investigated by developing an analytical criterion that can be used to determine a defined optimal ratio of the field to torque phases in a BDCE controlled multiphase induction machine. The theory presented in Chapter 2 from [58] is used in developing the criterion. Also, simple expressions for calculating the developed power, torque, stator and rotor copper losses of the BDCE controlled induction machine are presented. A method of constructing the trapezoidal stator current waveform is also presented. Analytically calculated results are presented and compared to finite element analysis results. Furthermore, finite element analysis results of a fifteen phase machine are given. Some of the work described here has been presented in [68].

3.2 Background Information

In this section, mathematical expressions for the developed power, flux density, stator and rotor copper losses of the BDCE controlled machine are presented. From these equations, it is shown that there is a theoretical best (optimal) combination ratio of m_f/m_t for a BDCE controlled machine. (For simplicity, the machine is analysed for rated conditions.)

3.2.1 Developed power and torque

The developed power, P_n , of a BDCE controlled multiphase induction machine is,

$$P_n = (m_t - 1)E_s I_t, \quad (3-1)$$

where, E_s is the induced voltage per stator phase. Rearranging (3-1) leads to

$$(m_t - 1)I_t = \frac{P_n}{E_s}. \quad (3-2)$$

The right hand side of (3-2) is a constant since P_n is equal to the rated power of the machine and E_s is equal to the rated voltage of the machine and thus, a decrease in I_t leads to a proportional increase in $(m_t - 1)$ or vice versa. Also from (3-1), it is seen that, the more the m_t , the lower is I_t and the lower the power rating per phase. Thus, it can be seen at this stage that theoretically m_t should be as large as possible, that is, $m_t = N_p - 3$.

The induced voltage per stator phase is given by,

$$\begin{aligned} E_s &= 2N_s l r_g B \omega_r \\ &= K_1 B \omega_r, \end{aligned} \quad (3-3)$$

where, N_s is the number of series turns per stator phase, l is the stack length, r_g is the air-gap radius, ω_r is the rated speed of the machine, K_l is a constant and B is the air-gap flux density. Since E_s is constant, then from (3-3), B is also a constant as ω_r is at rated speed for rated power. B is given by,

$$\begin{aligned} B &= \frac{\mu_0 F_f}{g k_c k_s} = \frac{\mu_0 N_s (m_f - 1) I_f}{2 p g k_c k_s} \\ &= K_2 \frac{(m_f - 1) I_f}{k_s}, \end{aligned} \quad (3-4)$$

where, F_f is the air-gap field MMF amplitude, g is the air-gap length, K_2 is a constant, k_s is the saturation factor and k_c is the Carter factor. Rearranging (3-4) leads to

$$I_f (m_f - 1) = \frac{k_s}{K_2} B, \quad (3-5)$$

or,

$$I_f (N_p - m_t - 1) = \frac{k_s}{K_2} B. \quad (3-6)$$

It can be seen from (3-5) and (3-6) that, increasing m_t leads to a decrease in m_f and an increase in I_f . In the machine, if m_f is reduced, the flux per pole increases (as B is constant whilst the pole area increases) and saturation increases in the stator and rotor yokes, thus, k_s in (3-6) increases, which leads to I_f increasing even more (due to saturation) to maintain the balance of (3-6). Thus, care must be taken in selecting m_t for a particular machine.

From (3-1) and (3-3), the rated torque of the machine, T , is given by,

$$T = \frac{P}{\omega_r} = K_1 (m_t - 1) B I_t. \quad (3-7)$$

Substituting for B from (3-4) in (3-7) gives,

$$T = \frac{K_2 K_1}{k_s} (m_t - 1) (m_f - 1) I_f I_t. \quad (3-8)$$

In (3-8), with the relations between I_f and $(m_f - 1)$, and between I_t and $(m_t - 1)$ as described above, T is constant.

3.2.2 Inverter currents and stator slot current density

The rated values of the field and torque current amplitudes determine the power rating of the IGBT switches to be used in the inverter. In some cases, the difference between I_f and I_t may be large and the IGBT may be under-utilised during some time instances and over-utilised during others. From section 3.2.1, for the same rating machine and with the total number of stator phases kept constant, the possible stator current waveform shapes are shown in Figure 3-1 *a*), *b*) and *c*). In Figure 3-1 *a*), the number of field and torque phases are equal whilst $I_t > I_f$. Here, only half of the time the inverter switches are operating at full (rated) potential. For some cases, $I_t = I_f$ (Figure 3-1 *b*)) or $I_t < I_f$ (Figure 3-1 *c*)). From Figure 3-1, it is clear that in the case of current waveforms *a*) and *c*), the peak stator slot current density varies during a cycle (period), whilst in the case of *b*), it stays constant. This has a bearing on the cooling of the machine. Thus, it is clear that, I_t must be as close as possible to I_f in order to allow for efficient inverter rating selection, inverter usage and the cooling of the machine.

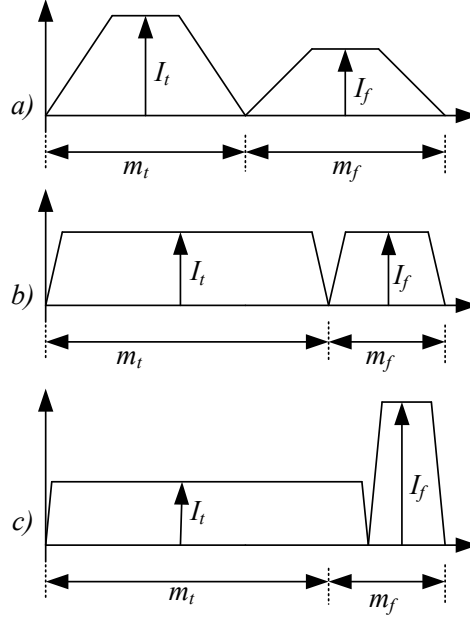


Figure 3-1. Possible stator current waveform shapes for a BDCE-controlled multiphase induction machine (only half a period of the waveform is shown)

3.2.3 Stator copper losses

In this section, the calculation of the stator copper losses of the BDCE controlled multiphase induction machine is presented. The calculation is based on the trapezoidal stator current waveforms and operation of the BDCE machine and it is compared to a general method where rms current values are used. In Figure 3-2, only the torque component of a stator phase current is shown. During drive operation, at any time instance, there are $(m_t - 2)$ torque phases having the rated current I_t , whilst two torque phases are in a transition stage (one with increasing and the other with decreasing I_t versus time). The instant positions of the two phases in a transition stage are labelled as u and $(1 - u)$ in Figure 3-2, where u varies between 0 and 1.

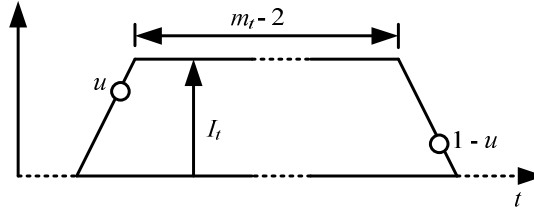


Figure 3-2. Single stator phase current waveform torque component

For ease of calculation, the stator copper loss of the torque phases at each time instance are separately calculated for the $(m_t - 2)$ torque phases and for the two phases in a transition phase. The copper loss of the $(m_t - 2)$ torque phases is

$$P_{tcu1} = (m_t - 2)I_t^2 R_s, \quad (3-9)$$

while the copper loss for the two phases in a transition stage is

$$\begin{aligned} P_{tcu2} &= uI_t^2 R_s + [(1-u)I_t]^2 R_s \\ &= I_t^2 R_s (2u^2 - 2u + 1), \end{aligned} \quad (3-10)$$

where R_s is the stator phase resistance and u is the position on the slope of the waveform varying between 0 and 1 as shown in Figure 3-2. In Figure 3-3, the plot of the function $2u^2 - 2u + 1$ is shown.

It can be seen in the figure that the minimum of the function is when the currents flowing in the two torque phases in the transition stage are equal at $u = 0.5$.

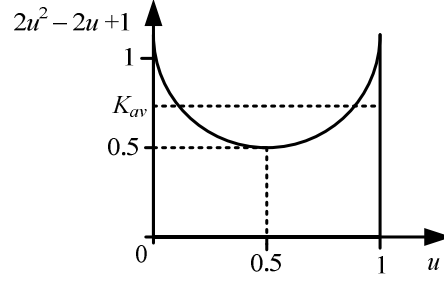


Figure 3-3. $2u^2 - 2u + 1$ function plot.

From (3-9) and (3-10), the total instantaneous copper loss of the torque phases is calculated as

$$\begin{aligned} P_{tcu} &= P_{tcu1} + P_{tcu2} \\ &= (m_t - 2)I_t^2 R_s + I_t^2 R_s (2u^2 - 2u + 1). \end{aligned} \quad (3-11)$$

From (3-11), the average copper loss of the torque phases is

$$P_{tcu} = [(m_t - 2) + K_{av}] I_t^2 R_s, \quad (3-12)$$

where K_{av} is the average of the function $(2u^2 - 2u + 1)$, as shown in Figure 3-3 and is determined as,

$$\begin{aligned} K_{av} &= \int_0^1 (2u^2 - 2u + 1) du \\ &= \frac{2}{3}. \end{aligned} \quad (3-13)$$

It must be noted that the value of K_{av} is the same irregardless of the number of torque phases. Similarly, the average copper loss of the field phases can be shown to be

$$P_{fcu} = [(m_f - 2) + K_{av}] I_f^2 R_s. \quad (3-14)$$

Thus the total stator copper loss, P_{scu} , is

$$\begin{aligned} P_{scu} &= P_{tcu} + P_{fcu} \\ &= [(m_t - 2) + K_{av}] I_t^2 R_s + [(m_f - 2) + K_{av}] I_f^2 R_s, \end{aligned} \quad (3-15)$$

or,

$$P_{scu} = [m_t - 2 + K_{av}] I_t^2 R_s + [N_p - m_t - 2 + K_{av}] I_f^2 R_s. \quad (3-16)$$

Hence, the minimum value of the stator copper losses can be found by differentiating (3-16) with respect to m_t , that is,

$$\frac{dP_{scu}}{dm_t} = I_t^2 R_s - I_f^2 R_s = 0. \quad (3-17)$$

This implies that the minimum value of the stator copper loss is found when

$$I_f = I_t. \quad (3-18)$$

The total stator copper losses can also be calculated as

$$P_{scu} = I_{srms}^2 R_s N_p, \quad (3-19)$$

where, I_{srms} is defined as the rms value of the stator current waveform and N_p is the number of stator phases. I_{srms} is calculated as

$$I_{srms} = \sqrt{\frac{1}{T_p} \int_0^{T_p} (i(t))^2 dt}, \quad (3-20)$$

where T_p is the period of the stator current waveform and $i(t)$ is the waveform. Also, I_{srms} can be calculated by first applying the Fourier transform on the waveform to break it down to its frequency components and then calculate

$$I_{srms} = \sqrt{I_{srms1}^2 + I_{srms3}^2 + I_{srms5}^2 + \dots}, \quad (3-21)$$

where, I_{srmsx} is the x th harmonic rms current. Although the Fourier transform method is complex, it is used in calculating I_{srmsx} in this dissertation because a generic program utilising it had already been developed for other parts of the dissertation.

The above analysis can be further explained by means of an example, as follows. The machine parameters for this example are given in Table 3-1. For each combination of m_f and m_t , the corresponding value of I_f and I_t is calculated from (3-6) and (3-7) respectively as given in Table 3-2. Saturation is assumed constant in the calculation of I_f , and the saturation factor is taken as, $k_s = 1.0$. Also, the ratios, P_{scu}/R_s , calculated from (3-16) and (3-19) are given and compared in the table. It can be seen from Table 3-2 that the minimum value of P_{scu}/R_s is obtained when $I_f \approx I_t$, as also found in (3-18). The results show that (3-16) can be used to calculate the stator copper losses in a simple and fast way.

Table 3-1. 12 phase, 31.4 kW machine parameters

T	200 Nm
N_s	85 turns
l	0.13 m
r_g	0.35 m
B	0.7 T
p	2
g	0.0005 m
k_c	1.2
N_p	12

Table 3-2. Calculated values of I_t , I_f and P_{scu}/R_s

m_f	6	5	4	3
m_t	6	7	8	9
I_t (A)	7.39	6.16	5.28	4.62
I_f (A)	3.15	3.93	5.24	7.86
P_{scu}/R_s (3-16) (W/ Ω)	300.89	271.48	258.95	266.55
P_{scu}/R_s (3-19) (W/ Ω)	301.15	271.63	259.06	266.45

3.2.4 Rotor copper losses

The rotor phase or bar current is directly proportional to the slip speed, ω_{sl} , (from (2-10)) and according to (2-4), ω_{sl} is directly proportional to I_t since the control gain, k , is constant irregardless of the number of torque phases. Thus, decreasing I_t (increasing m_t as suggested in section 3.2.1) results in a decrease in the peak bar current density and a decrease in the copper losses per bar. Thus better cooling is obtained as lower peak currents flows in the rotor bar.

Under balanced MMF conditions, $F_t = F_r$. With

$$F_t = \frac{1}{2}(m_t - 1)(N_s / p)I_t \quad (3-22)$$

and

$$F_r = m_{ra} N_r I_r, \quad (3-23)$$

the rotor bar current is given by

$$I_r = \frac{(m_t - 1)N_s I_t}{2pm_{ra}N_r}, \quad (3-24)$$

The total rotor bar copper losses (for the active bars) can be calculated as

$$\begin{aligned} P_{rcu} &= 2pm_{ra}I_r^2 R_b \\ &= \frac{(m_t - 1)^2 N_s^2 I_t^2}{2pm_{ra}N_r^2} R_b, \end{aligned} \quad (3-25)$$

where R_r is the bar resistance. Using (3-7) it can be shown that (3-25) becomes

$$P_{rcu} = \frac{R_b N_s^2 T^2}{2pm_{ra}N_r^2 K_1^2 B^2}, \quad (3-26)$$

where T , R_b and B are constant. Since from (2-8)

$$m_{ra} = \frac{M_r(m_t - 1)}{2N_p p}, \quad (3-27)$$

it can be seen, from (3-26), that the total rotor copper losses for a specified rated machine, under BDCE control, depends on the number of active rotor bars or rotor phases which, in turn depends on m_t . Thus an increase in m_t will lead to a decrease in P_{rcu} .

In summary, from the above sections, it is noted that in any machine under BDCE control, care needs to be taken in selecting the m_t and m_f combination for a machine, as this directly affects the inverter rating, stator and rotor copper losses and saturation in the machine. The best combination ratio

m_f/m_t is defined as the ratio that provides $I_f \approx I_t$, and limits saturation in the stator and rotor yokes. This ratio is evaluated with P_n , B , N_p and p kept constant.

3.3 Constructing the Stator Current Waveforms

A general procedure for constructing the current waveforms for machines with a number of phases which are multiples of three can be developed in this section. In Figure 3-4, a trapezoidal stator current waveform where the number of field phases, m_f , and the number of torque phases, m_t is labelled. The sum of m_f and m_t gives the total number of stator phases for the machine, N_p . I_f and I_t are the amplitudes of the field and torque current respectively.

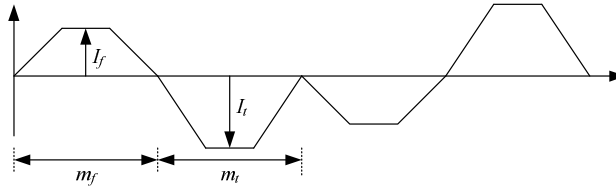


Figure 3-4. Trapezoidal stator current waveform.

For a machine with N_p stator phases, the phases are grouped into three groups of $N_p/3$ phases each. Then, the appropriate combination of m_f and m_t is selected and the waveform as shown in Figure 3-4 is constructed. All the other phases are constructed by phase shifting this waveform by

$$\varphi = \frac{2\pi}{3}(z-1) + \frac{\pi}{N_p}(i-1), \quad z = 1, 2, \text{ or } 3 \text{ and } i = 1, 2, \dots, N_p/3, \quad (3-28)$$

where φ is the phase shift, z is the group index and i is the phase index. For example, the first and second phase groups of a fifteen-phase machine are shown in Figure 3-5, where $m_f = 3$ and $m_t = 12$.

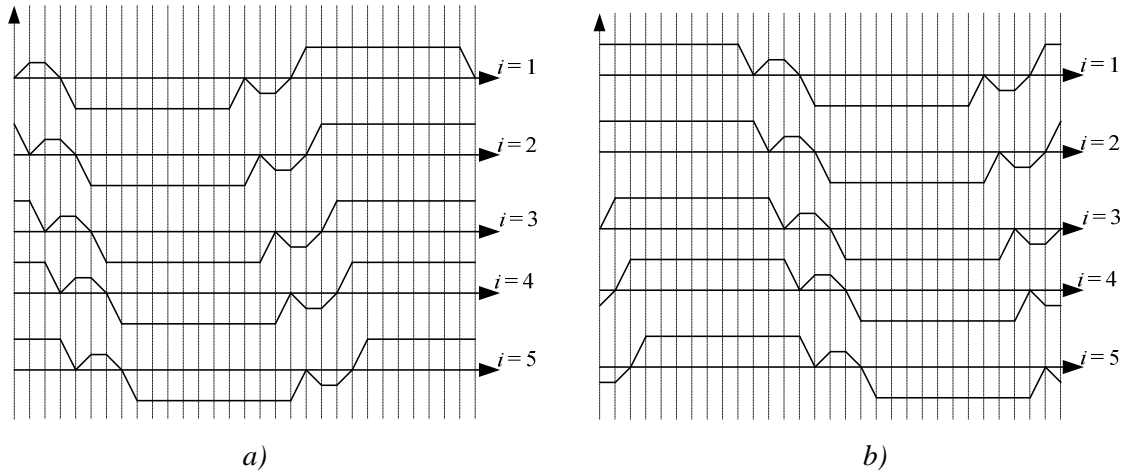


Figure 3-5. Stator current waveforms, with fifteen stator phases, $m_f = 3$ and $m_t = 12$, *a*) first group ($z = 1$), and *b*) second group ($z = 2$).

3.4 Machine Dimensions

In order to calculate the MMF of the machine as described in the next section, the machine dimensions have to be defined. In this section the general machine dimensions, calculated with reference to the stator outer diameter, are provided. Also the chosen stator and rotor slot shapes are presented.

3.4.1 Stator core main dimensions

The stator outer diameter, d_s , is assumed to be known and most of the other machine dimensions are estimated directly or indirectly from it. From experience, the ratio of the stator inner diameter, d_{si} , to the outer diameter of an induction machine is typically,

$$\frac{d_{si}}{d_s} = 0.65. \quad (3-29)$$

The air-gap length is critical in machine design. It is known that a too small air-gap produces large space air-gap field harmonics and additional losses, whilst a too large one leads to a reduction in the power factor and efficiency. Therefore, the air-gap length, g , is expressed in relation to the rated power of a machine in kW, P_n , as [69]

$$g = (0.1 + 0.012\sqrt[3]{P_n}) \times 10^{-3}. \quad (3-30)$$

3.4.2 Stator slots and winding

Since multiphase induction machines with high phase numbers are considered, a single layer concentrated stator winding is appropriate due to limited possible stator slots. Therefore, the total number of stator slots, M_s , is given by,

$$M_s = 2pN_p, \quad (3-31)$$

where p and N_p are the number of pole pairs and phases respectively. Thus, the number of stator slots per pole is equal to N_p .

3.4.3 Stator slot sizing

Figure 3-6 shows the chosen stator slot geometry. The variables of the stator slot geometry are estimated from experience with reference to the stator outer diameter, inner diameter and air-gap length as shown in Table 3-3, where, t_{ps} is the stator slot pitch. The stator slot copper area is then calculated as,

$$S_A = 0.82 \left(s_{ws} s_{hb} + (\pi / 2) (s_{br} / 2)^2 + (s_{br} - s_{ws}) s_{hb} \right). \quad (3-32)$$

The multiplication factor, 0.82, in equation (3-32) takes care of the area covered by the insulation material in the stator slot.

3.4.4 Rotor slot sizing

A cage rotor winding is considered for all the machines in this chapter. Figure 3-7 shows the selected rectangular geometry of the rotor slot. From experience, the slot variables of Figure 3-7 are estimated through the formulas in Table 3-4, where, t_{pr} is the rotor slot pitch and M_r is the number of rotor slots.

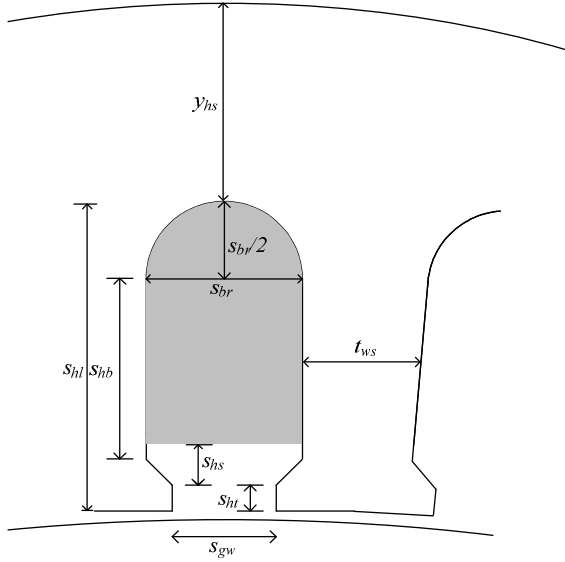


Figure 3-6. Stator slot geometry.

Table 3-3. Estimation of stator slot variables.

Variable	Equation
s_{ht}	$0.004d_s$
s_{hs}	$0.008d_s$
s_{br}	$(\pi d_s - 2\pi y_{hs} - M_s t_{ws}) / M_s$
s_{hb}	$s_{hl} - s_{hs} - s_{ht} - 0.5s_{br}$
s_{gw}	$5g$
y_{hs}	$(d_s - d_{si}) / 4$
s_{hl}	$(d_s - d_{si}) / 2 - y_{hs}$
t_{ws}	$t_{ps} / 2$
t_{ps}	$\pi d_{si} / M_s$

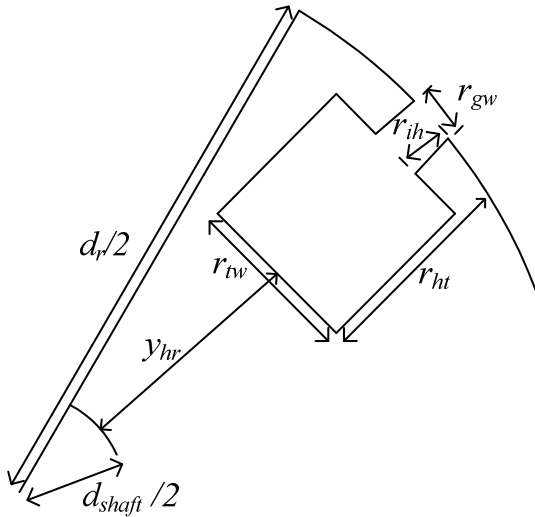


Figure 3-7. Rotor slot geometry.

Table 3-4. Estimation of rotor slot variables.

Variable	Equation
d_{shaft}	$d_s / 6$
r_{gw}	$3.5g$
r_{ih}	$0.004d_s$
d_r	$d_{si} - 2g$
t_{pr}	$\pi d_r / M_r$
r_{ht}	$(d_r - d_{shaft}) / 4$
y_{hr}	$r_{ht} / 2$

3.5 MMF Calculations

A stator winding produces a travelling MMF wave in the air-gap of a machine when alternating currents flows through it. Assuming a uniform air-gap, uniform stator slot current density, J , (no skin effect) and fill factor, k_f , then the total current into a machine stator slot, I , is

$$I = JS_A k_f, \quad (3-33)$$

where S_A is the copper area of the stator slot given in equation (3-32). Generally, $k_f = 0.5$ is used. The current density varies according to the rated power of the machine, and from literature, in this Chapter its range is defined to be $3 \leq J \leq 6 \text{ A/mm}^2$, where a low value of J corresponds to a large machine (1

MW machine). Then, the variation between the rated power and the current density can be approximated by the following linear relationship,

$$J = -3P_n + 6 \times 10^6, \quad (3-34)$$

where P_n is the rated power of a machine in kW. When the machine is excited using the trapezoidal current waveform and the field current is assumed to be equal to the torque current ($I_f = I_t$), the total current into a stator slot, I , can also be represented in terms of the stator field current, I_f , that is,

$$I = \frac{N_s I_f}{pa}, \quad (3-35)$$

where N_s is the number of series turns per stator phase, p is the number of pole pairs and a is the number of parallel circuits. For demonstration purposes, $a = 1$. Therefore, with $I_t = 0$ A, the MMF per pole of the machine at any time instance due to the stator field current components is

$$\begin{aligned} F_1 &= (m_f - 1) \frac{N_s I_f}{pa} \\ &= (m_f - 1) I. \end{aligned} \quad (3-36)$$

In (3-36), I stays constant since $I_f = I_t$. The magnetic circuit (Ampere's) law can be used to calculate the MMF per pole of the machine. Only a fraction of the magnetic circuit needs to be analyzed due to symmetry. That is, for a $2p$ pole machine, only $1/2p$ of the magnetic circuit needs to be analysed, where p is the number of pole pairs. Figure 3-8 shows a section of a machine and the MMF per pole of the machine can be calculated through the application of the magnetic circuit law along the flux or dotted line. The flux line is divided into different segments and the MMF is calculated for each segment. These segments are: the air-gap (g), the stator tooth (ts), the rotor tooth (tr), the stator core (cs) and the rotor core (cr), and their MMFs are evaluated given by,

$$\begin{aligned} F_g &= \frac{B k_c g}{\mu_o} \\ F_{ts} &= H_{sv} h_{sv} \\ F_{tr} &= H_{rv} h_{rv} \\ F_{cs} &= H_{sy} h_{sy} + H_{sef} l_{sef} + H_{set} l_{set} \\ F_{cr} &= H_{ry} h_{ry} + H_{ref} l_{ref} + H_{ret} l_{ret}, \end{aligned} \quad (3-37)$$

where B is the air-gap flux density, k_c is the Carter factor, μ_o is absolute permeability, and H is the magnetic field intensity which is obtained from the B-H curve of the lamination steel after calculating the flux densities for each particular segment. The other symbols represent segments as shown in Figure 3-8 where: l – length, h – height and subscripts: s – stator, r – rotor, y – yoke, t – torque, c – core, v – tooth and f – field. In Figure 3-8, l_{sef} , l_{set} , l_{ret} and l_{ref} are dependent on the number of field and torque phases, and are calculated through basic arithmetic. Then, the individual segment MMFs are summed up, and the result is the MMF per pole of the machine, that is,

$$F_2 = F_g + F_{ts} + F_{tr} + F_{cs} + F_{cr}. \quad (3-38)$$

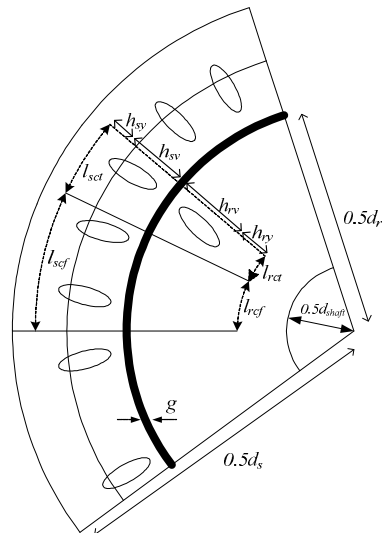


Figure 3-8. Dimensions of the machine cores with the magnetic circuit used in the analysis.

3.6 Finding the Optimal Ratio of Field to Torque Phases

The air-gap MMFs calculated in equations (3-36) and (3-38) are used in the calculation of the defined optimal value of the ratio of field to torque phases (m_f/m_t). The value of the ratio m_f/m_t that leads to $F_1 \approx F_2$, with the air-gap flux density closest to a preset rated value for a particular machine being considered, is the optimal value of the ratio of field to torque phases. An iterative MATLAB program that includes the effects of saturation through the use of the B-H curve has been developed to calculate F_2 of (3-38) and the optimal value of the ratio m_f/m_t more accurately. A high level program flow chart that describes the calculation of the optimal value of the ratio m_f/m_t is shown in Figure 3-9. The minimum values of m_f and m_t must be greater or equal to three in order to maintain the trapezoidal stator current waveform shape.

3.7 Analytical Results

Table 3-5 gives the recommended intervals of the air-gap flux density for the different numbers of poles in a machine obtained from [69]. Arbitrary combinations of stator to rotor slots numbers are selected for the analysis without considering effects such as parasitic torques, additional losses, radial forces, noise and vibration. The optimal ratio of the field to torque phases is given in Table 3-6 for a 100 kW, four pole induction machine considering different number of phases. The results in the table show that a lower number of field phases can be used in the operation of the induction machine using the trapezoidal stator current waveforms. It is observed that, as the number of phases is increased, the ratio m_f/m_t reduces. The calculated flux density is within the range given in Table 3-5. A fifteen phase induction machine is further investigated with different number of poles and the results are given in Table 3-7 to Table 3-9. The results show that, the ratio m_f/m_t decreases with an increase in the number of poles in the machine. Again, the calculated flux density is well within the required range.

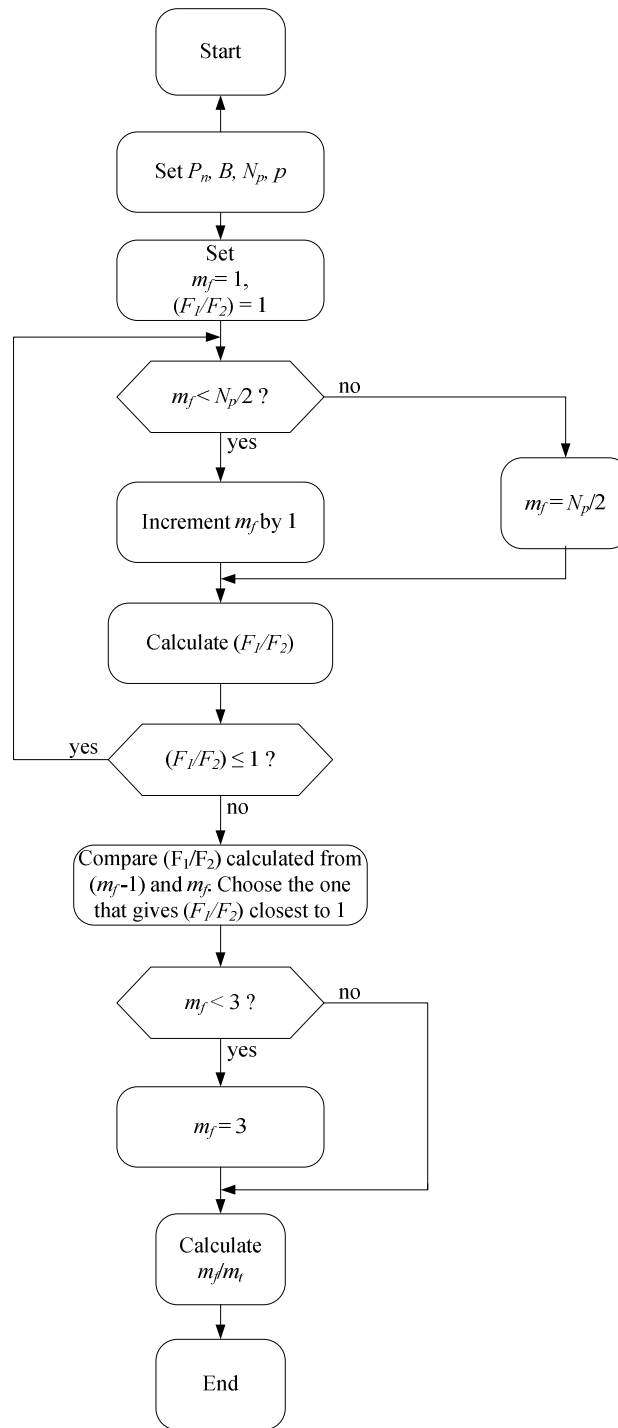


Figure 3-9. Program flowchart for evaluating m_f/m_t with $I_f = I_t$ and P_n, B, N_p and p set at certain constant values.

Table 3-5. Air-gap flux density recommended ranges [69].

Number of pole-pairs, p	Required B (T) range
2	0.65 - 0.78
3	0.7 - 0.82
4	0.75 - 0.85

Table 3-6. m_f/m_t for a 4-pole, 100 kW induction machine versus number of stator phases.

Phases	d_s	M_r	m_f	m_f/m_t	B (T)
9	0.5	28	3	1/2	0.72
12	0.5	37	3	1/3	0.64
15	0.5	47	4	4/11	0.66

Table 3-7. m_f/m_t for a 4-pole, 15-phase induction machine versus rated power.

P_n (kW)	d_s	M_r	m_f	m_f/m_t	B (T)
10	0.25	47	5	1/2	0.71
50	0.4	47	4	4/11	0.66
100	0.5	47	4	4/11	0.66
300	0.6	47	4	4/11	0.67

Table 3-8. m_f/m_t for a 6-pole, 15-phase induction machine versus rated power.

P_n (kW)	d_s	M_r	m_f	m_f/m_t	B (T)
10	0.25	70	3	1/4	0.8
50	0.4	70	3	1/4	0.79
100	0.5	70	3	1/4	0.79
300	0.6	70	3	1/4	0.79

Table 3-9. m_f/m_t for an 8-pole, 15-phase induction machine versus rated power.

P_n (kW)	d_s	M_r	m_f	m_f/m_t	B (T)
10	0.25	93	5	1/2	0.8
50	0.4	93	3	1/4	0.79
100	0.5	93	3	1/4	0.79
300	0.6	93	3	1/4	0.8

3.8 Finite Element Analysis (FEA)

In this section, the aim is to evaluate the analytical method presented in section (3-31). The analytically calculated results of a fifteen-phase induction machine are compared with FEA results obtained through a non-commercial FEA software package. Only a quarter of the four pole, fifteen-phase induction machine considered in this section is modelled in the FEA software through the use of symmetry conditions. Also, for convenience, there is one stator slot per pole per phase, i.e. $q = 1$, and there are twelve rotor bars per pole in the FEA model. Only the field current is applied to the machine in the analysis, whilst the torque current is kept at zero (the balanced MMF condition is assumed). In the FEA software, skewing is realized by using a set of un-skewed machines of which the rotor phases are displaced by an angle that is a fraction of the total skew. When skewing is considered, in the FEA, the rotor is skewed by one stator slot pitch by means of a set of five un-skewed rotors.

3.8.1 Air-gap Flux Density

Table 3-10 gives m_f/m_t results calculated for different fifteen-phase machines according to the analytical method described previously. In the same table, the analytically calculated flux density, B_{an} , is compared with FEA evaluated flux density, B_{FE} . The stator outer diameter and rated power of the machines given in the table are extracted from commercial induction machine data. From the results it is clear that fewer field phases can be used as the machine gets larger to keep the air-gap flux density within the range between 0.65 – 0.78 T. The FEA results show that three field phases are sufficient to produce an air-gap flux density within the range, for a 300 kW, four pole, fifteen-phase induction machine.

The FEA calculated field plot in Figure 3-10 is that of a 100 kW ($d_s=0.5$ m), 4-pole, 15-phase machine, with four field phases active at time $t = 0$. The machine's square-like air-gap flux density with its average trend is shown in Figure 3-11. Figure 3-12 shows a moving average air-gap flux density as time changes from $t = 0$ to $t = t_1/2$. It is clear that the flat topped amplitude of the moving flux density stays almost constant with stator MMF movement.

Figure 3-13 shows that the average amplitude variation of the air-gap flux density with rotating position is a minimal with $m_f = 3$ and $m_f = 4$. In [58], the FE calculations show a variation of 6 %, while the results of Figure 3-13 show far less variation, of, 0.7 % from the required air-gap flux density. From this result, it can be expected that the commutation of the field phases will not introduce significant high frequency induced voltages in the rotor bars, since there is little variation in air-gap flux density amplitude with rotating position.

Table 3-10. Comparison of analytically and FEA calculated air-gap flux densities calculated for determined m_f/m_t for a 4-pole 15-phase induction machine with varying rated power.

P (kW)	J (A/mm ²)	d_s (m)	m_f	m_f / m_t	B_{an} (T)	B_{FE} (T)
5.5	5.98	0.216	5	5/10	0.712	0.653
30	5.91	0.318	4	4/11	0.657	0.663
75	5.78	0.457	4	4/11	0.657	0.687
110	5.67	0.508	4	4/11	0.659	0.697
300	5.10	0.61	4	4/11	0.67	0.719
300	5.10	0.61	3	3/12	0.611	0.672

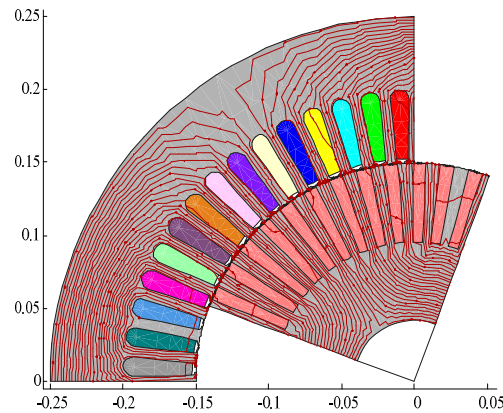


Figure 3-10. Field plot of 4-pole 15-phase induction machine.

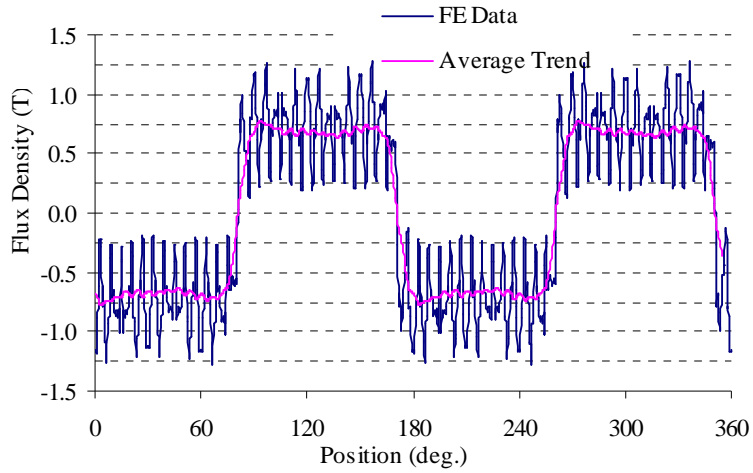


Figure 3-11. Air-gap flux density distribution around the air-gap of four pole fifteen-phase induction machine at $t = 0$.

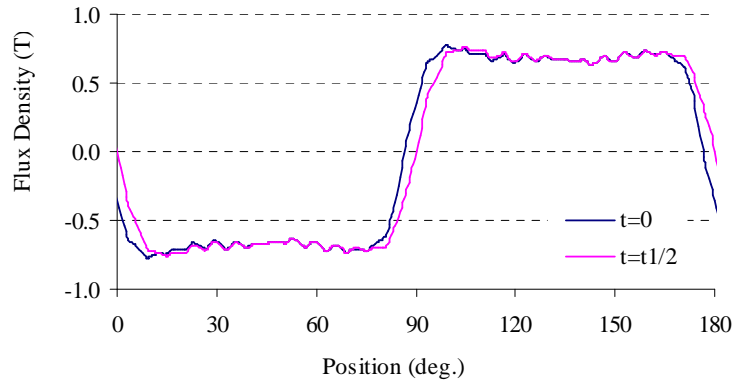


Figure 3-12. Averaged air-gap flux density at different times of a 4-pole, 15-phase induction machine.

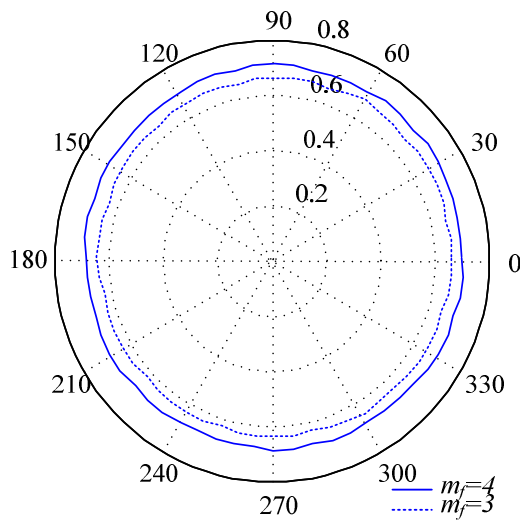


Figure 3-13. Air-gap flux density amplitude versus rotating position (4-pole, 15-phase).

3.8.2 Rotor Induced Voltage

The open circuit voltage in the i -th rotor phase bar is given by

$$e_i = \frac{d\lambda_i}{dt}, \quad (3-39)$$

where λ_i is the flux linkage of the rotor phase bar which is calculated as

$$\lambda_i = \frac{1}{k_s} \sum_{j=1}^{k_s} \lambda_{ij} \alpha_j, \quad (3-40)$$

where λ_{ij} is the total flux linkage of phase bar i with un-skewed rotor j at skewed position α_j , and k_s is the number of un-skewed rotors. The forward difference method is used to approximate the derivative of the flux linkage, i.e.

$$e_i = \frac{d\lambda_i}{dt} \approx \frac{\lambda_i(t_0 + \Delta t) - \lambda_i(t_0)}{\Delta t}. \quad (3-41)$$

With the rotor at standstill and the stator field rotating by supplying four field phase currents of the fifteen-phase induction machine of Figure 3-10, the triangular flux linkages of two of the rotor phase bars labelled phase 15 and phase 20 in the FEA, are shown in Figure 3-14. The slip is taken as 4% (60 r/min). Using the forward difference approximation and FE time stepping analysis, the induced rotor voltage is determined as shown in Figure 3-15 and Figure 3-16. Figure 3-15 shows the high frequency (equal to $30f$, where f is the fundamental frequency of the stator voltage) induced rotor bar voltage. The voltage-ripple in Figure 3-16 is due to the slotted air-gap. An almost square induced voltage is obtained, which shows the property of a brush-dc motor.

3.9 Summary

In this Chapter, analytical expressions of calculating the developed power, torque, stator and rotor copper losses of the BDCE controlled machine are presented. Also, an analytical method used to calculate the optimal ratio of field to torque phases of multiphase induction machines supplied with trapezoidal stator current waveforms, is derived. Saturation is considered in the analytical method through the use of B-H curve. The comparison of analytical and FEA calculated results shows that it is possible to use lesser field current phases to produce the required air-gap flux density. Increasing the number of phases and also increasing the number of poles are shown to lead to a lower optimal m_t/m_f ratio. With fewer field phases, there is increased rotor winding utilization and more torque phases are used.

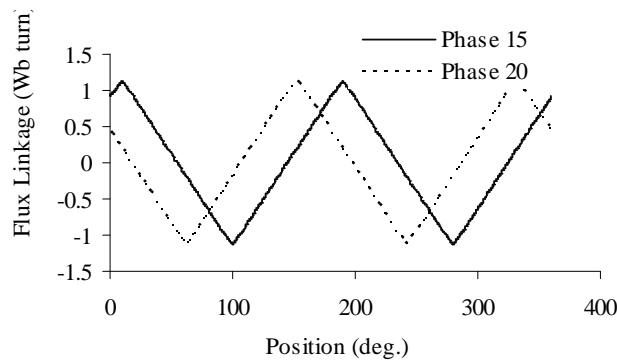


Figure 3-14. Rotor bar flux linkages with position of field MMF.

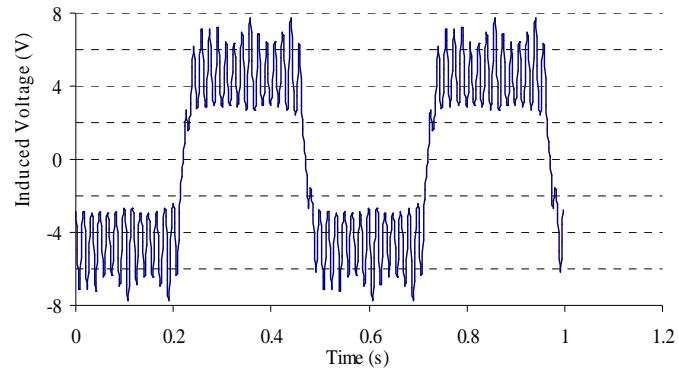


Figure 3-15. Un-skewed rotor induced bar voltage (stationary rotor and moving stator field).

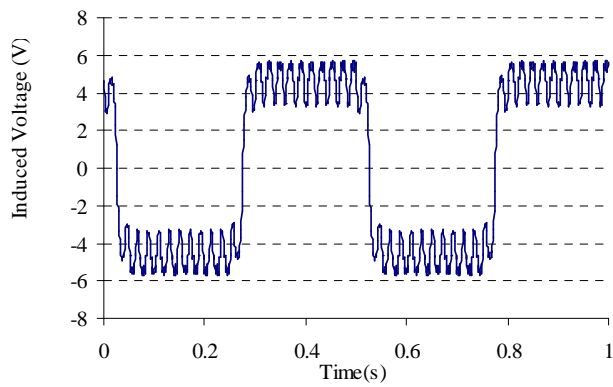


Figure 3-16. Skewed rotor induced bar voltage (moving rotor and stationary stator field).

Chapter 4

Theoretical Analysis of BDCE Controlled Multiphase Induction Machines

4.1 Introduction

Theoretical analysis is very significant in the performance study and design of an induction machine. These analyses allow the investigation and improvement of the machine's design, control and efficiency.

A theoretical or analytical method of predicting and evaluating the rotor bar current waveform is presented in this Chapter. It is based on the winding function theory that is used to calculate machine inductances presented as by Lipo et al in [8], [25], [26]. This method is used in the calculation of the rotor bar current waveform as well as the torque and rotor copper losses of the machine. To start off, the stator current waveform is broken down to its harmonic frequency components through Fourier transformations. It is assumed that each harmonic component is a perfect sinusoid and that each component acts independently of the others. Thus, each stator current harmonic can be analysed individually. Furthermore, saturation is ignored, a uniform air-gap is considered, m identical stator windings with axes of symmetry and n identical rotor windings with axes of symmetry are considered, there are no eddy currents, friction and windage losses are ignored and the rotor bars are assumed to be insulated.

The analyses in this Chapter consider an individual frequency component of the trapezoidal stator current waveform. During simulation, the results from each individual component are summed up in order to find the performance of the machine when supplied with the trapezoidal stator current waveforms. Therefore, this analysis method is independent to the number of stator phases in a multiphase induction machine under BDCE control.

Results from the application of the analytical method on an arbitrary chosen nine-phase induction machine are given. These results are compared to FEA results. Only steady-state conditions are considered, hence, transient analysis is beyond the scope of this work.

4.2 Rotor Voltage Equations

In this section, the rotor voltage equations are presented. The cage rotor can be represented by Figure 4-1 where R is resistance, L is inductance and the subscripts e and b denote end ring and rotor bar respectively. Therefore, the rotor is viewed as n identical and equally spaced rotor loops [8], [25], [26]. Also, the n th loop consists of the n th and the $(n + 1)$ th rotor bars together with the connecting end ring segments between them. Since there are n bars in the cage rotor, there are $n + 1$ independent rotor currents comprising of n loop currents and a circulating current in one of the end rings.

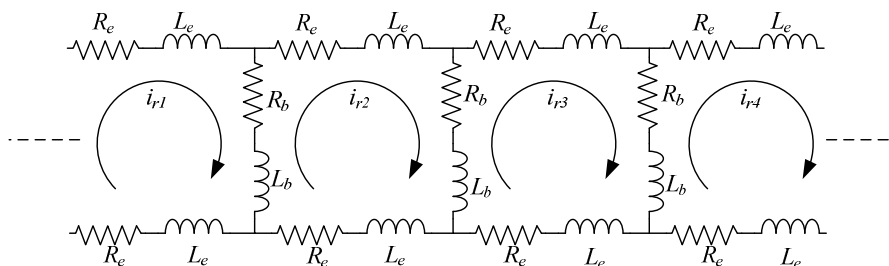


Figure 4-1. Equivalent circuit of a squirrel cage rotor showing rotor loop currents.

With the cage rotor replaced with mutually coupled loops, the voltage equations for the rotor loops in vector-matrix form are,

$$\mathbf{V}_r = \mathbf{R}_r \mathbf{I}_r + \frac{d\mathbf{\Lambda}_r}{dt}, \quad (4-1)$$

where, \mathbf{V}_r is the rotor loop voltage vector, \mathbf{R}_r is a rotor loop resistance matrix, \mathbf{I}_r is the loop currents vector and $\mathbf{\Lambda}_r$ is the rotor loop flux linkages matrix. The rotor loop voltage vector for the cage rotor can also be written as,

$$\begin{aligned} \mathbf{V}_r &= [v_{r1} \ v_{r2} \ \dots \ v_{rm} \ v_e]^t \\ &= [0 \ 0 \ \dots \ 0 \ 0]^t \\ &= \mathbf{R}_r \mathbf{I}_r + \frac{d\mathbf{\Lambda}_r}{dt}, \end{aligned} \quad (4-2)$$

where t represents vector or matrix transpose. Therefore the rotor loop flux linkages can be calculated from the loop voltage equation as,

$$\begin{aligned} \frac{d\mathbf{\Lambda}_r}{dt} &= -\mathbf{R}_r \mathbf{I}_r \\ \mathbf{\Lambda}_r &= \int -\mathbf{R}_r \mathbf{I}_r dt. \end{aligned} \quad (4-3)$$

Alternately, the rotor flux linkage is given by

$$\begin{aligned} \mathbf{\Lambda}_r &= \mathbf{L}_{rs} \mathbf{I}_s + \mathbf{L}_{rr} \mathbf{I}_r \\ &= \mathbf{L}_{sr}^t \mathbf{I}_s + \mathbf{L}_{rr} \mathbf{I}_r, \end{aligned} \quad (4-4)$$

where \mathbf{L}_{rs} is the mutual inductance matrix between rotor loop circuits and stator phases and \mathbf{L}_{sr} is the mutual inductance matrix between stator phases and rotor loop circuits, \mathbf{I}_s is the stator current vector and \mathbf{L}_{rr} is the $(n + 1)$ by $(n + 1)$ symmetric rotor loop inductance matrix. In this analysis, it is assumed that $\mathbf{L}_{rs} = \mathbf{L}_{sr}^t$ where \mathbf{L}_{sr}^t is the transpose of the matrix \mathbf{L}_{sr} . The matrices \mathbf{R}_r , \mathbf{L}_{sr} and \mathbf{L}_{rr} are described in the next sections. The stator current vector is given by

$$\mathbf{I}_s = [i_{s1} \ i_{s2} \ \dots \ i_{sm}]^t, \quad (4-5)$$

and the rotor circuit current vector can be written as

$$\mathbf{I}_r = [i_{r1} \ i_{r2} \ \dots \ i_{rn} \ i_{re}]^t. \quad (4-6)$$

In (4-6), i_{re} is the end ring current. Here, the motor is assumed to have complete end rings (no broken segments) and hence, i_{re} is equal to zero. The current vector can be obtained by making \mathbf{I}_r the subject of equation (4-4), that is

$$\mathbf{I}_r = \mathbf{L}_{rr}^{-1} \mathbf{\Lambda}_r - \mathbf{L}_{rr}^{-1} \mathbf{L}_{sr}^t \mathbf{I}_s. \quad (4-7)$$

As previously stated, the current \mathbf{I}_r is an instantaneous current matrix resulting from the application of only one stator current frequency component in the machine. It is noted that these equations represent instantaneous values.

4.2.1 Resistance matrix \mathbf{R}_r

From Figure 4-1, the rotor loop resistance matrix, \mathbf{R}_r , is an $(n + 1)$ by $(n + 1)$ symmetric matrix and can be written as

$$\mathbf{R}_r = \begin{bmatrix} 2(R_b + R_e) & -R_b & 0 & \dots & 0 & -R_b & -R_e \\ -R_b & 2(R_b + R_e) & -R_b & \dots & 0 & 0 & -R_e \\ \cdot & \cdot & \cdot & \dots & \cdot & \cdot & \cdot \\ \cdot & \cdot & \cdot & \dots & \cdot & \cdot & \cdot \\ 0 & 0 & 0 & \dots & 2(R_b + R_e) & -R_b & -R_e \\ -R_b & 0 & 0 & \dots & -R_b & 2(R_b + R_e) & -R_e \\ -R_e & -R_e & -R_e & \dots & -R_e & -R_e & nR_e \end{bmatrix} \quad (4-8)$$

where R_b and R_e are the rotor bar resistance and the end ring resistance respectively.

4.2.2 Rotor inductance matrix \mathbf{L}_{rr}

From Figure 4-1 and with the following definitions: L_{mr} is the magnetizing inductance of each rotor loop, and L_{riri} is the mutual inductance between two rotor loops i and j , the rotor inductance matrix \mathbf{L}_{rr} can be written as

$$\mathbf{L}_{rr} = \begin{bmatrix} L_{mr} + 2(L_b + L_e) & L_{r1r2} - L_b & L_{r1r3} & \dots & L_{r1r(n-1)} & L_{r1m} - L_b & -L_e \\ L_{r2r1} - L_b & L_{mr} + 2(L_b + L_e) & L_{r2r3} - L_b & \dots & L_{r2r(n-1)} & L_{r2m} & -L_e \\ \cdot & \cdot & \cdot & \dots & \cdot & \cdot & \cdot \\ \cdot & \cdot & \cdot & \dots & \cdot & \cdot & \cdot \\ L_{r(n-1)r1} & L_{r(n-1)r2} & L_{r(n-1)r3} & \dots & L_{mr} + 2(L_b + L_e) & L_{r(n-1)m} - L_b & -L_e \\ L_{mr1} - L_b & L_{mr2} & L_{mr3} & \dots & L_{mr(n-1)} - L_b & L_{mr} + 2(L_b + L_e) & -L_e \\ -L_e & -L_e & -L_e & \dots & -L_e & -L_e & nL_e \end{bmatrix} \quad (4-9)$$

4.2.3 Mutual inductance matrix \mathbf{L}_{sr}

The mutual inductance matrix, \mathbf{L}_{sr} , is an m by $(n + 1)$ matrix comprising of the mutual inductances between the stator coils and the rotor loops. It can be written as

$$\mathbf{L}_{sr} = \begin{bmatrix} L_{s1r1} & L_{s1r2} & \cdot & \cdot & L_{s1rn} & L_{s1re} \\ L_{s2r1} & L_{s2r2} & \cdot & \cdot & L_{s2rn} & L_{s2re} \\ \cdot & \cdot & \cdot & \cdot & \cdot & \cdot \\ L_{smr1} & L_{smr2} & \cdot & \cdot & L_{smrn} & L_{smre} \end{bmatrix} \quad (4-10)$$

4.3 Mutual Inductance Calculation

In this section, a description of how the mutual inductances of a machine are calculated using the winding function theory is presented. The winding function is defined as the MMF distribution along the air-gap for a unit current flowing in a winding. Figure 4-2 shows one winding function of a two-pole concentrated winding induction machine. The winding function and the winding distribution of rotor loop rl from Figure 4-1 are shown in Figure 4-3 and Figure 4-4 respectively. In Figure 4-3 and Figure 4-4, α is the angle between two rotor bars in radians.

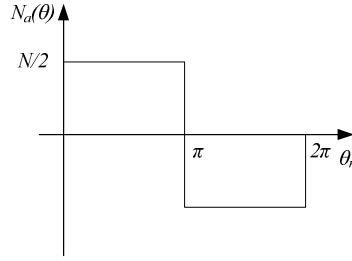


Figure 4-2. Phase a winding function for a concentrated full pitch winding.

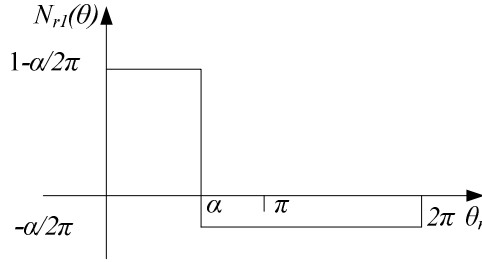


Figure 4-3. Winding function of a rotor loop [8].

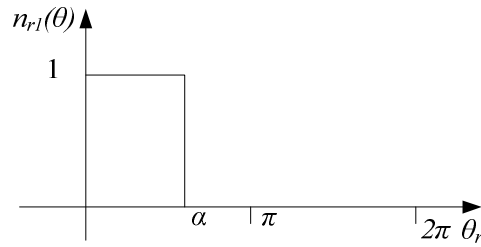


Figure 4-4. Winding distribution of a rotor loop [8].

From Figure 4-2 to Figure 4-4, the winding function theory approach presented in [8], [25] and [26] states that the mutual inductance between any two windings i and j in any electrical machine can be calculated as

$$L_{ij} = \frac{\mu_0 r_g l}{g} \int_0^{2\pi} n_i(\theta_r) N_j(\theta_r) d\theta_r, \quad (4-11)$$

where r_g is the average radius of the air-gap, l is the stack length, g is the air-gap length, θ_r is the spatial mechanical angle of the rotor with reference to a stationary point on the stator, $n_i(\cdot)$ is the i -th winding distribution and $N_j(\cdot)$ is the j -th winding function. Equation (4-11) is used to calculate the mutual inductances of (4-10).

4.4 Instantaneous Bar and End Ring Currents

Considering the rotor circuit currents in Figure 4-1, the instantaneous current flowing in the n th bar is given by

$$i_{bx(n)}(t) = i_{rn}(t) - i_{r(n+1)}(t). \quad (4-12)$$

In (4-12), x is the x th stator current time harmonic order. Furthermore, it is noted that the current flowing in an end ring segment of Figure 4-1 is equal to the loop circuit current defined for the particular segment, that is,

$$i_{es(n)}(t) = i_m(t). \quad (4-13)$$

4.5 Torque Calculation

An instantaneous torque calculation method, based on the magnetic co-energy, is summarised in this section. The magnetic co-energy, W_{co} , is equal to the stored magnetic energy in a linear magnetic system, that is

$$W_{co} = \frac{1}{2} \begin{bmatrix} \mathbf{I}_s^t & \mathbf{I}_r^t \end{bmatrix} \begin{bmatrix} \mathbf{L}_{ss} & \mathbf{L}_{sr} \\ \mathbf{L}_{sr}^t & \mathbf{L}_{rr} \end{bmatrix} \begin{bmatrix} \mathbf{I}_s \\ \mathbf{I}_r \end{bmatrix}. \quad (4-14)$$

Then, the electromagnetic torque due to the x th stator current harmonic can be calculated as,

$$T_{ex} = \left[\frac{\partial W_{co}}{\partial \theta_r} \right]_{\mathbf{I}_s, \mathbf{I}_r \text{ constant}}. \quad (4-15)$$

Here, θ_r is the spatial mechanical angle of the rotor with reference to a stationary point on the stator. Since \mathbf{L}_{rr} and \mathbf{L}_{ss} contain constant elements, then using (4-14), the torque equation (4-15) reduces to

$$T_{ex} = \frac{1}{2} \left(\mathbf{I}_s^t \frac{\partial \mathbf{L}_{sr}}{\partial \theta_r} \mathbf{I}_r + \mathbf{I}_r^t \frac{\partial \mathbf{L}_{sr}^t}{\partial \theta_r} \mathbf{I}_s \right). \quad (4-16)$$

It is seen that T_{ex} is a scalar quantity and therefore each of the terms that are added to form T_{ex} must be a scalar too. A transpose of a scalar is the scalar itself. Also, from matrix algebra,

$$(\mathbf{A}^t \mathbf{B}^t \mathbf{C})^t = \mathbf{C}^t \mathbf{B} \mathbf{A}. \quad (4-17)$$

Hence,

$$\mathbf{I}_r^t \frac{\partial \mathbf{L}_{sr}^t}{\partial \theta_r} \mathbf{I}_s = \left(\mathbf{I}_r^t \frac{\partial \mathbf{L}_{sr}^t}{\partial \theta_r} \mathbf{I}_s \right)^t = \mathbf{I}_s^t \frac{\partial \mathbf{L}_{sr}}{\partial \theta_r} \mathbf{I}_r. \quad (4-18)$$

Therefore, the electric torque equation reduces to

$$T_{ex} = \mathbf{I}_s^t \frac{\partial \mathbf{L}_{sr}}{\partial \theta_r} \mathbf{I}_r, \quad (4-19)$$

where \mathbf{I}_s is given by (4-5), \mathbf{L}_{sr} is given by (4-10) and \mathbf{I}_r is given by (4-7). For a $2p$ -pole machine, the inductance undergoes $2p/2$ complete cycles as θ_r varies from 0 to 2π mechanical, hence the electrical position is given by,

$$\theta = \frac{2p}{2} \theta_r. \quad (4-20)$$

4.6 Simulation Algorithm

In this section, the simulation algorithm used to evaluate amongst other things, the rotor bar current waveform, the torque and the rotor copper losses of a machine using the analysis acquired for an individual stator current component, is presented. The instantaneous contributions of individual stator harmonic currents to the rotor current waveform, torque or rotor copper losses are simply added during simulation. The sum, then, represents the performance of the machine when fed with trapezoidal stator current waveforms. For example, the total instantaneous current induced in rotor bar 1 can be written as

$$i_{b1} = \sum_{x=1}^{\infty} i_{bx1}(t), \quad (4-21)$$

where, x is the stator current time harmonic and $i_{bx1}(t)$ is calculated from (4-12). Similarly,

$$T_{eT} = \sum_{x=1}^{\infty} T_{ex}. \quad (4-22)$$

T_{ex} is the instantaneous torque per stator current harmonic calculated from equation (4-19), and T_{eT} is the total instantaneous torque produced by the machine supplied with the trapezoidal stator current waveforms. The simulation program flow chart to evaluate the instantaneous performance of the induction machine is shown in Figure 4-5. Considering frequency dependency, the rotor bar resistance and inductance are calculated through the method proposed by Babb and Williams [70, 71], and presented in Appendix C. The end ring resistance and inductance are calculated from analytical equations also presented in Appendix C.

4.7 Finite Element Analysis (FEA) Modelling

Maxwell2D FEA software is selected to evaluate the performance of the machine as well as to predict the rotor currents. The transient solver is used because it allows the use of non-sinusoidal current excitations and rotational motion. It also helps in analysing magnetic fields, torque, power loss and flux of a model at various time steps over a specified time period.

Since the induction machine under consideration is symmetrical, only a quarter of a nine-phase four pole machine is modelled, as shown in Figure 4-6. In the model, Dirichlet boundary conditions are applied to the stator outer and rotor inner diameter. The vector potential is tangential and defined as zero at the stator outer and rotor inner diameter. Master / slave boundaries are defined on the other edges of the model. These boundaries force the magnetic field at each point on the master boundary to match the magnetic field at each corresponding point on the slave boundary. For this model, the field on the slave boundary is defined to point in the exact opposite direction of the field on the master boundary. These boundaries are labelled in Figure 4-6.

In the transient solver, rotational motion is defined as occurring inside a selected band object. The band object is defined to cover the rotor of the machine in the model. Also, for the stator coils, stranded conductors are selected, whilst for the rotor bars solid conductors are used. The contribution of the stranded conductors to the current density is averaged over the slot area because such conductors lack eddy current behaviour in the transient solver. However, for solid conductors, skin effects are considered and they depend on the frequency of the system as well as on the location of nearby conductors.

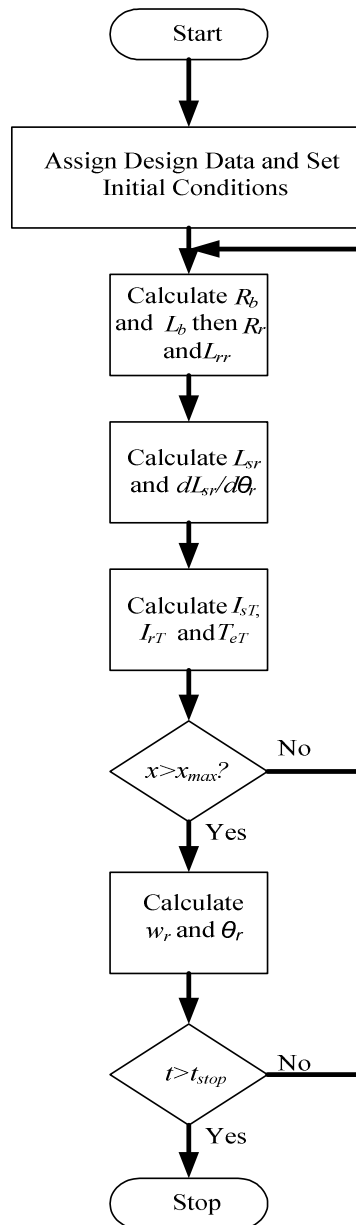


Figure 4-5. Simulation program flow chart, where t is time in seconds, t_{stop} is the time allowed for the simulation to run and x_{max} is a preset value of highest considered stator current harmonic.

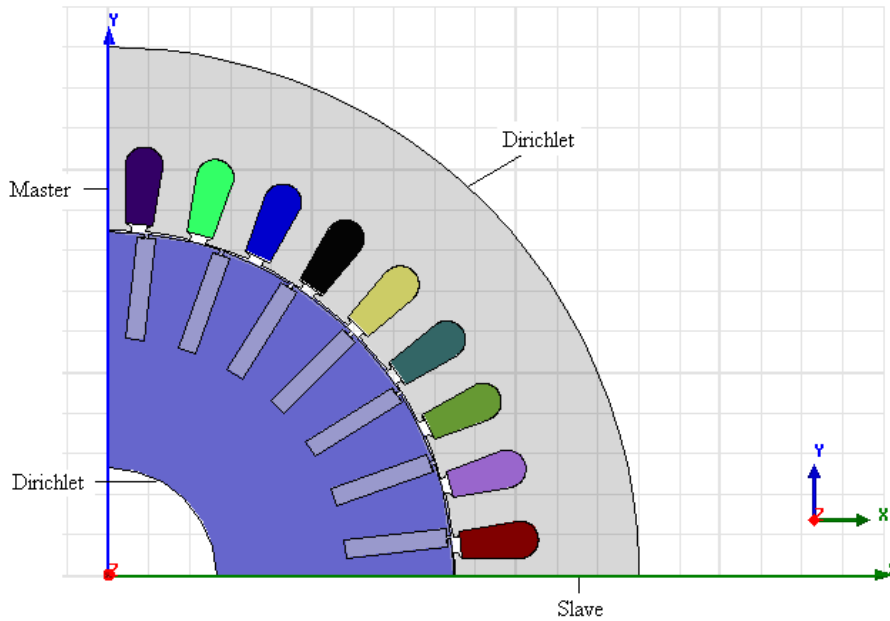


Figure 4-6. FE model of the nine-phase induction machine

4.8 Theoretical Analysis of a Nine-Phase Induction Machine

In this section, the described analytical method is used to evaluate the performance of a nine-phase induction machine given as an example. Other multiphase machines could have been used, but the nine-phase induction machine was chosen because of practical considerations. The nine-phase induction machine parameters are shown in Table 4-1. The following describes the contents of the section:

- Using the method described previously in Chapter 3, the optimal ratio of field to torque phases for a nine phase machine is found to be 0.5 whereby the number of field phases is three as shown in Table 3-6. The nine-phase current waveforms are derived as described in section 3.3. Fourier analysis is conducted in order to represent the stator current waveforms and air-gap MMF mathematically.
- The air-gap flux density due to the field current components of the stator current waveform is calculated from the MMF.
- The performance of the machine and the rotor current waveform are evaluated analytically using the described analytical method.
- Finally, FEA results are given and compared to the theoretical results where possible. Although linear conditions are assumed in the theoretical analysis, the FEA considers saturation.

4.8.1 Nine-phase trapezoidal current waveforms and their mathematical expressions

In this section, the trapezoidal stator current waveforms are presented. Figure 4-7 shows the nine-phase trapezoidal current waveforms constructed using the method described in the previous Chapter. Three phases operate as field MMF producing phases and six phases operate as torque MMF producing phases. In this section, it is also shown that these stator current waveforms produce a nearly square air-gap flux density when applied to a nine-phase, four pole induction machine with the winding layout of Figure 4-8. In Figure 4-8, crosses show a winding coil into the page and dots show a winding coil out of the page.

Table 4-1. Machine parameters of a 4-pole 9-phase induction machine.

Rated Power, P_n	11kW
Air-gap length, g	0.5 mm
Stack length, l	127 mm (copper bars)
Rotor radius	84.5 mm
End ring segment resistance, R_e	$1.28e-6 \Omega$ (75°C)
End ring segment inductance, L_{er}	29.2 nH
Number of field phases, m_f	3
Number of torque phases, m_t	6
Number of rotor bars, M_r	28
Number of stator slots, M_s	36
Number of series turns per stator phase, N_s	170
Torque current, I_t	5.5 A
Field current, I_f	5.83 A
Bar height	25 mm
Bar width	4.5mm
Operating speed	1472 r/min

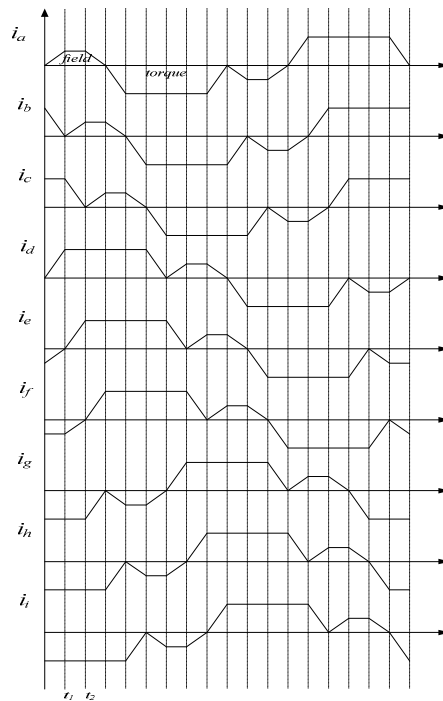


Figure 4-7. Nine-phase stator current waveforms.

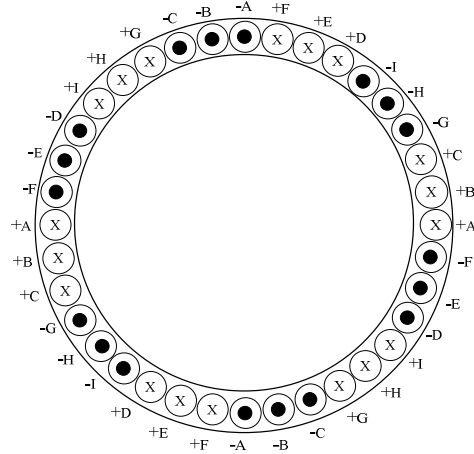


Figure 4-8. Stator winding layout of a 4-pole, 9-phase induction machine.

In order to perform analytical calculations, it is necessary to find a mathematical expression of the stator current waveforms. A mathematical representation of a waveform is obtained through the application of the Fourier transform on the waveform, as follows. Phase a of the nine-phase stator current waveforms is shown in Figure 4-9.

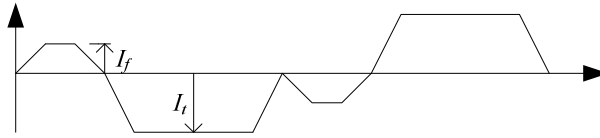


Figure 4-9. Phase a stator current waveform, $i_a(t)$, with $m_f = 3$ and $m_t = 6$.

Applying the Fourier transform on the waveform yields

$$i_a(t) = \sum_{n=-\infty}^{\infty} I(x)e^{jx\omega t}, \quad (4-23)$$

where

$$I(x) = \frac{1}{T} \int_0^T i_a(t)e^{-jx\omega t} dt \quad (4-24)$$

and ω is the electrical angular frequency and x is the time harmonic order, $x = 1, 2, 3, \dots$

Performing integration by parts, $I(x)$ become

$$I(x) = \frac{9}{2x^2\pi^2} I_f \left(-1 + e^{-\frac{jx\pi}{9}} + e^{\frac{2jx\pi}{9}} - e^{-\frac{jx\pi}{3}} + e^{-jx\pi} - e^{-\frac{10jx\pi}{9}} - e^{-\frac{11jx\pi}{9}} + e^{\frac{4jx\pi}{3}} \right) + \frac{9}{2x^2\pi^2} I_t \left(e^{\frac{jx\pi}{3}} - e^{\frac{4jx\pi}{9}} - e^{-\frac{8jx\pi}{9}} + e^{-jx\pi} + e^{\frac{13jx\pi}{9}} - e^{\frac{4jx\pi}{3}} + e^{\frac{17jx\pi}{9}} - e^{-2jx\pi} \right). \quad (4-25)$$

Substituting $I(x)$ into $i_a(t)$ of (4-23) and using trigonometric identities leads to

$$i_a(t) = \sum_{x=1}^{\infty} \frac{18}{x^2 \pi^2} (k_1 \cos(x\omega t) + k_2 \sin(x\omega t)) \quad \text{for } x = 1, 3, 5, 7, \dots, \quad (4-26)$$

where

$$k_1 = -I_t - I_f + 2I_f \cos(x\pi/18) \sin(x\pi/2) \sin(2x\pi/3) + (-I_f + I_t) \sin(x\pi/2) \sin(5x\pi/6) - 2I_t \cos(2x\pi/9) \sin(x\pi/2) \sin(7x\pi/6) \quad (4-27)$$

$$k_2 = -2I_f \cos(x\pi/18) \sin(x\pi/2) \cos(2x\pi/3) - (I_t - I_f) \sin(x\pi/2) \cos(5x\pi/6) + 2I_t \cos(2x\pi/9) \sin(x\pi/2) \cos(7x\pi/6)$$

Equation (4-26) can be further simplified using the trigonometric identity

$$A \cos(\alpha) + B \sin(\alpha) = \sqrt{A^2 + B^2} \cos(\alpha - \text{atan2}(B, A)), \quad (4-28)$$

where $\text{atan2}()$ is a four-quadrant inverse tangent. Hence, $i_a(t)$ becomes

$$i_a(t) = \sum_{x=1}^{\infty} \frac{18}{x^2 \pi^2} \left(\sqrt{k_1^2 + k_2^2} \cos(x\omega t - \text{atan2}(k_2, k_1)) \right) \quad \text{for } x = 1, 3, 5, 7, \dots \quad (4-29)$$

Therefore, the current waveform can be viewed to be made up of the addition of infinite independent sinusoidal waveforms of different frequencies as shown in Figure 4-10. The higher the number of considered harmonics, the more accurately the waveform is constructed. Similarly, the mathematical representation of the other waveforms can be obtained as for $i_d(t)$ and are given in equation (4-30).

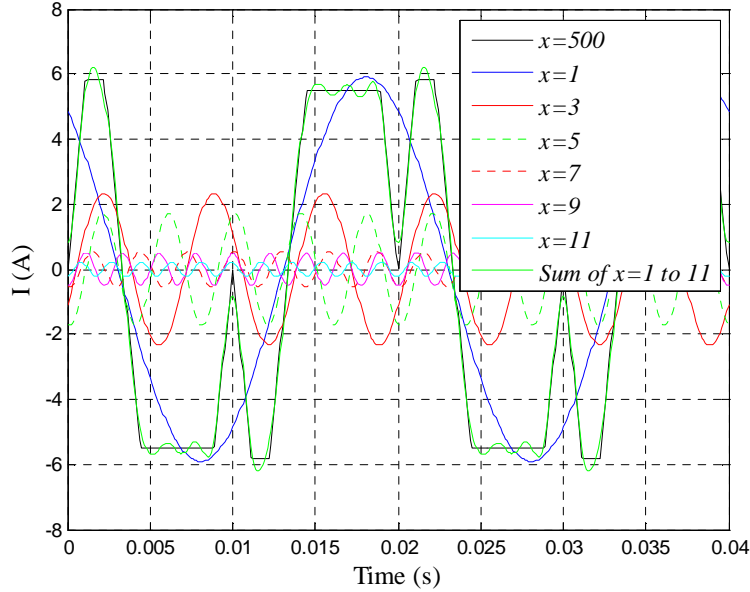


Figure 4-10. Per phase stator current waveform ($x = 500$) with its first six harmonics ($I_f = 5.83$ A and $I_t = 5.5$ A). The waveform of the sum of the first six harmonics is also shown.

4.8.2 MMF generated by the trapezoidal current waveforms

The placement of coils on stator slots is such that the stator winding produces a rotating MMF in the air-gap when excited by the stator current waveforms. In this section, a mathematical expression which can be used to show that the stator winding, with the layout shown in Figure 4-8, does produce a rotating MMF in the air-gap when excited by the stator current waveforms of Figure 4-7, is provided. The developed MMF expression is used in the calculation of the air-gap flux density and it can be used to calculate the contribution of each stator current harmonic to the rotating MMF. The

MMF waveform for a single coil with N turns and i current flowing in a four pole machine stator is shown in Figure 4-11, where F is the MMF and θ is in electrical radians. A Fourier series expansion of the MMF waveform allows it to be decomposed into all the harmonics that make up the waveform. When infinite permeability in the iron is assumed, the MMF in the stator and rotor can be neglected and therefore the MMF across the air-gap is equal to the total MMF.

$$\begin{aligned}
 i_a(t) &= \sum_{x=1}^{\infty} \frac{18}{x^2 \pi^2} \left(\sqrt{k_1^2 + k_2^2} \cos(x\omega t - a \tan 2(k_2, k_1)) \right) \\
 i_b(t) &= \sum_{x=1}^{\infty} \frac{18}{x^2 \pi^2} \left(\sqrt{k_1^2 + k_2^2} \cos(x(\omega t - \pi/9) - a \tan 2(k_2, k_1)) \right) \\
 i_c(t) &= \sum_{x=1}^{\infty} \frac{18}{x^2 \pi^2} \left(\sqrt{k_1^2 + k_2^2} \cos(x(\omega t - 2\pi/9) - a \tan 2(k_2, k_1)) \right) \\
 i_d(t) &= \sum_{x=1}^{\infty} \frac{18}{x^2 \pi^2} \left(\sqrt{k_1^2 + k_2^2} \cos(x(\omega t - 6\pi/9) - a \tan 2(k_2, k_1)) \right) \\
 i_e(t) &= \sum_{x=1}^{\infty} \frac{18}{x^2 \pi^2} \left(\sqrt{k_1^2 + k_2^2} \cos(x(\omega t - 7\pi/9) - a \tan 2(k_2, k_1)) \right) \\
 i_f(t) &= \sum_{x=1}^{\infty} \frac{18}{x^2 \pi^2} \left(\sqrt{k_1^2 + k_2^2} \cos(x(\omega t - 8\pi/9) - a \tan 2(k_2, k_1)) \right) \\
 i_g(t) &= \sum_{x=1}^{\infty} \frac{18}{x^2 \pi^2} \left(\sqrt{k_1^2 + k_2^2} \cos(x(\omega t - 12\pi/9) - a \tan 2(k_2, k_1)) \right) \\
 i_h(t) &= \sum_{x=1}^{\infty} \frac{18}{x^2 \pi^2} \left(\sqrt{k_1^2 + k_2^2} \cos(x(\omega t - 13\pi/9) - a \tan 2(k_2, k_1)) \right) \\
 i_i(t) &= \sum_{x=1}^{\infty} \frac{18}{x^2 \pi^2} \left(\sqrt{k_1^2 + k_2^2} \cos(x(\omega t - 14\pi/9) - a \tan 2(k_2, k_1)) \right)
 \end{aligned} \tag{4-30}$$

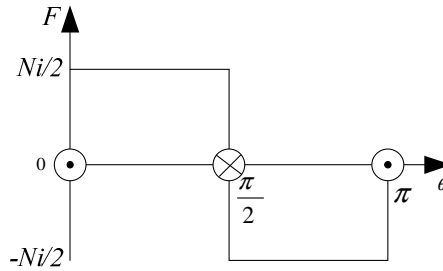


Figure 4-11. MMF waveform produced by a full-pitch single coil for a 4-pole induction machine.

The Fourier transform for the MMF waveform is

$$F(\theta) = \sum_{m=-\infty}^{\infty} F(v) e^{jvp\theta} \tag{4-31}$$

$$F(v) = \frac{1}{\pi} \int_0^{\pi} F(\theta) e^{-jvp\theta} d\theta \tag{4-32}$$

where, p is the number of pole pairs and v is the harmonic order. Applying integration by parts yields

$$F(v) = \frac{Ni}{4\pi v} (2je^{-jv\pi} - j - je^{-2jv\pi}), \quad (4-33)$$

and hence

$$F(\theta) = \sum_{v=1}^{\infty} \frac{2Ni}{\pi v} \sin(vp\theta), \quad v = 1, 3, 5, \dots \quad (4-34)$$

The current, i , is considered to be an instantaneous current. Using equation (4-30), each of the nine-phase stator current waveforms will produce a corresponding MMF given by the following equations:

$$\begin{aligned} F_a(\theta) &= \sum_{v=1}^{\infty} \frac{N_s i_a(t)}{\pi v} \sin(vp\theta) \\ F_b(\theta) &= \sum_{v=1}^{\infty} \frac{N_s i_b(t)}{\pi v} \sin(vp(\theta - \pi/18)) \\ F_c(\theta) &= \sum_{v=1}^{\infty} \frac{N_s i_c(t)}{\pi v} \sin(vp(\theta - 2\pi/18)) \\ F_d(\theta) &= \sum_{v=1}^{\infty} \frac{N_s i_d(t)}{\pi v} \sin(vp(\theta - 6\pi/18)) \\ F_e(\theta) &= \sum_{v=1}^{\infty} \frac{N_s i_e(t)}{\pi v} \sin(vp(\theta - 7\pi/18)) \\ F_f(\theta) &= \sum_{v=1}^{\infty} \frac{N_s i_f(t)}{\pi v} \sin(vp(\theta - 8\pi/18)) \\ F_g(\theta) &= \sum_{v=1}^{\infty} \frac{N_s i_g(t)}{\pi v} \sin(vp(\theta - 12\pi/18)) \\ F_h(\theta) &= \sum_{v=1}^{\infty} \frac{N_s i_h(t)}{\pi v} \sin(vp(\theta - 13\pi/18)) \\ F_i(\theta) &= \sum_{v=1}^{\infty} \frac{N_s i_i(t)}{\pi v} \sin(vp(\theta - 14\pi/18)) \end{aligned} \quad (4-35)$$

Finally, the MMF due to the stator winding is found by summing the individual MMFs as

$$\begin{aligned} F_s(\theta) &= F_a(\theta) + F_b(\theta) + F_c(\theta) + F_d(\theta) + F_e(\theta) + F_f(\theta) + F_g(\theta) + F_h(\theta) + F_i(\theta) \\ &= \sum_{j=a}^i F_j(\theta). \end{aligned} \quad (4-36)$$

Equation (4-36) can be used to show that the stator winding produce a rotating MMF in the air-gap when the trapezoidal stator current waveform are considered. Using the equation, each current harmonic contribution can be evaluated independently.

4.8.3 Air-gap flux density

Assuming infinite permeability of iron, the air-gap flux density, $B(\theta)$, can be expressed in terms of the MMF given in (4-36) as

$$B(\theta) = \frac{\mu_0 F_s(\theta)}{g}, \quad (4-37)$$

where g is the air-gap length.

The basis for the machine operation is that the torque MMF cancels the rotor MMF as explained in the conceptualisation of the control method in Chapter 2. Therefore, under balanced conditions, the field in the air-gap is produced by the field current. With $I_r = 0$ A and $I_f = 5.83$ A, the input current waveform for only phase a and its fundamental are shown in Figure 4-12.

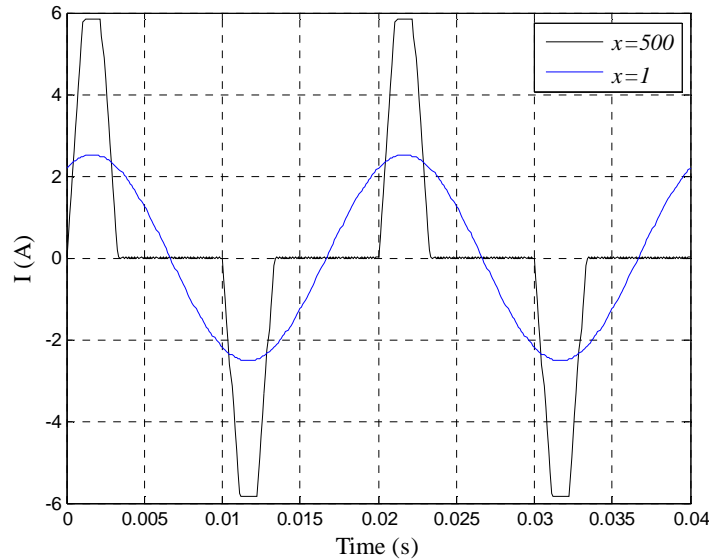


Figure 4-12. Phase a stator current waveform with only field current.

The air-gap flux density of the machine is calculated with $I_r = 0$ A and the rotor currents equal zero using a program written in MATLAB software. The flux density calculated from the MMF at a stationary point in the air-gap with the machine excited by the trapezoidal current waveforms at locked rotor test, is shown in Figure 4-13. The analytically calculated air-gap flux density has a flat topped amplitude of 0.63 T. Also, the analytically calculated air-gap flux density versus air-gap position at a particular time-instance is shown in Figure 4-14. The FEA calculated flux density is shown in Figure 4-15, showing visible slotting effects. The average air-gap flux density calculated through FEA has an average amplitude of 0.71 T. There is a similarity between the waveforms of the analytical results, Figure 4-14, and the FEA results, Figure 4-15.

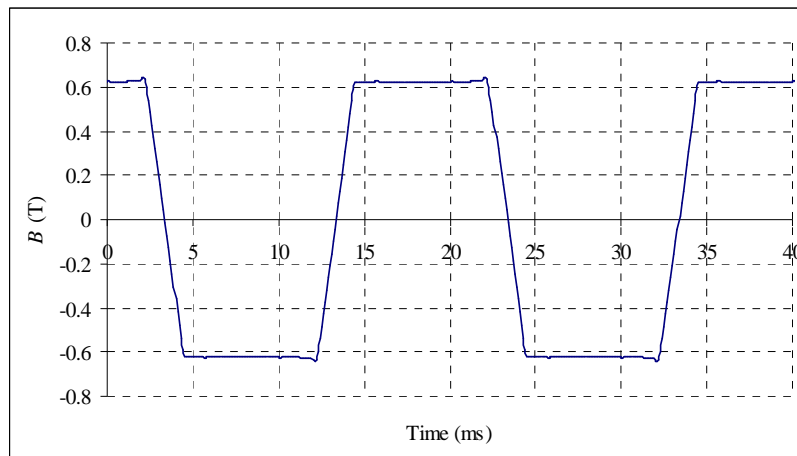


Figure 4-13. Analytically calculated flux density variation versus time at a position in the air-gap ($x = 1, 3, \dots, 49, v = 1, 3, \dots, 99$).

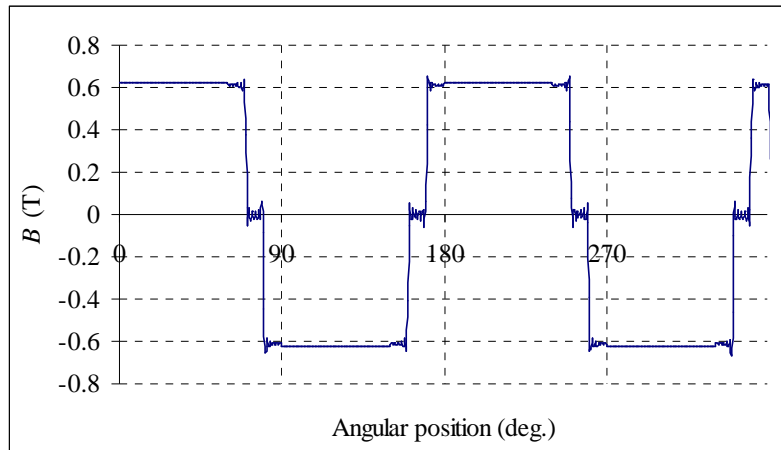


Figure 4-14. Analytically calculated air-gap flux density versus air-gap position ($x = 1, 3, \dots, 49, v = 1, 3, \dots, 99$).

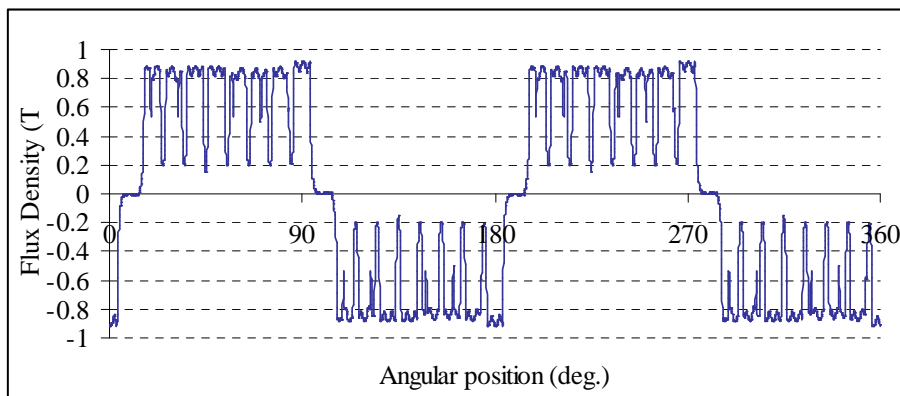


Figure 4-15. FEA air-gap flux density versus air-gap position at time $t = 0$ (unskewed rotor).

4.8.4 Rotor current waveforms

The rotor current waveforms are evaluated analytically as described in section 4.4 and compared with FEA results. In Figure 4-16, an approximate trapezoidal stator current waveform consisting of the first seven harmonics is shown. The first seven harmonics are sufficient in the study of the shape of the rotor current waveform, because the higher current harmonics have little contribution. The analytically evaluated end ring and bar current waveforms are shown in Figure 4-17 and Figure 4-18 respectively when stator current harmonic orders 1, 3, ..., 13 are considered. The rotor is rotating at rated speed of 1472 r/min given in Table 4-1. The filtered version of Figure 4-18 is shown in Figure 4-19. It looks like the bar current is following the stator current waveform. The rotor current waveform evaluated through FEA is shown in Figure 4-20. It is clear that, the analytically calculated and FEA simulated bar current waveforms are very similar. They differ only in amplitude as observed in Figure 4-19 and Figure 4-20. The cause of this difference is unknown at the moment. Nonetheless, the FEA results do validate the theoretical calculation method.

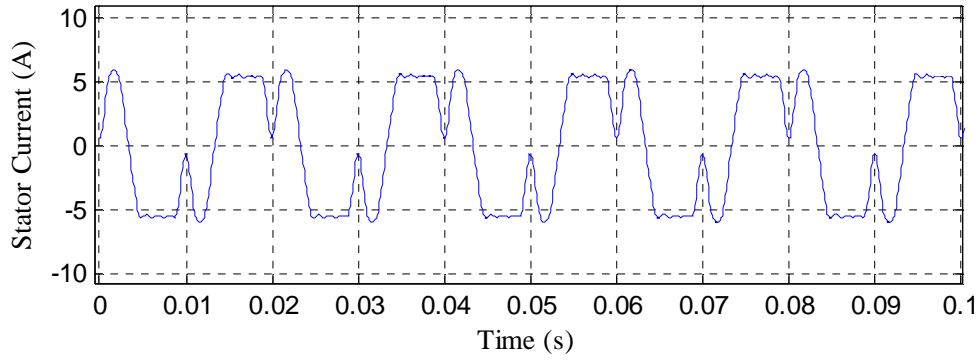


Figure 4-16. An approximate stator current waveform consisting of the first seven harmonics.

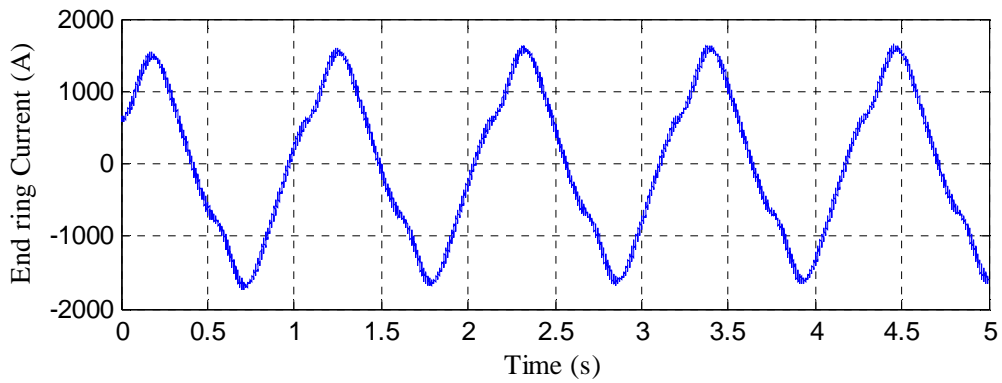


Figure 4-17. End ring current waveform of the nine-phase induction machine.

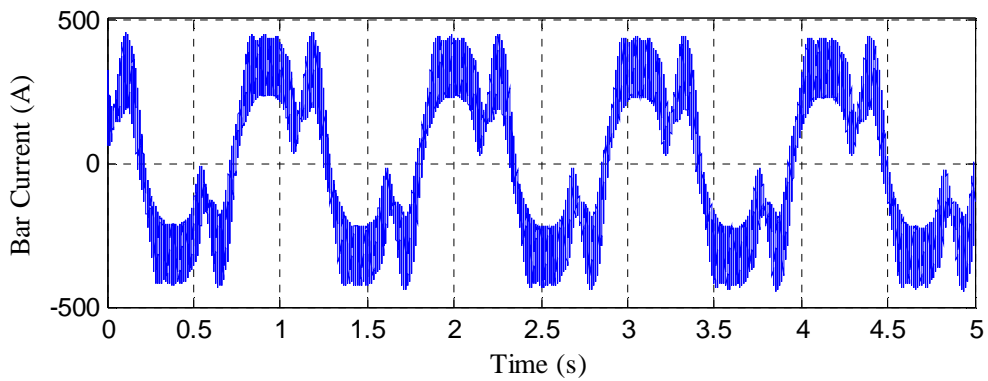


Figure 4-18. Rotor bar current waveform of the nine-phase induction machine.

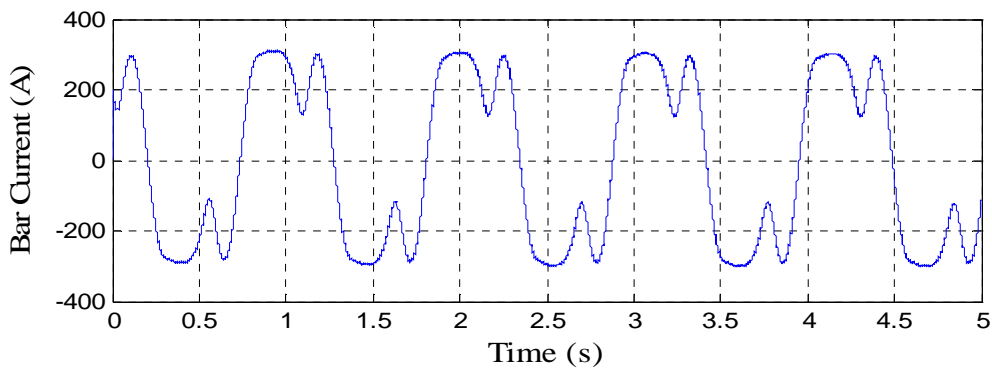


Figure 4-19. Filtered rotor bar current waveform of the nine-phase induction machine.

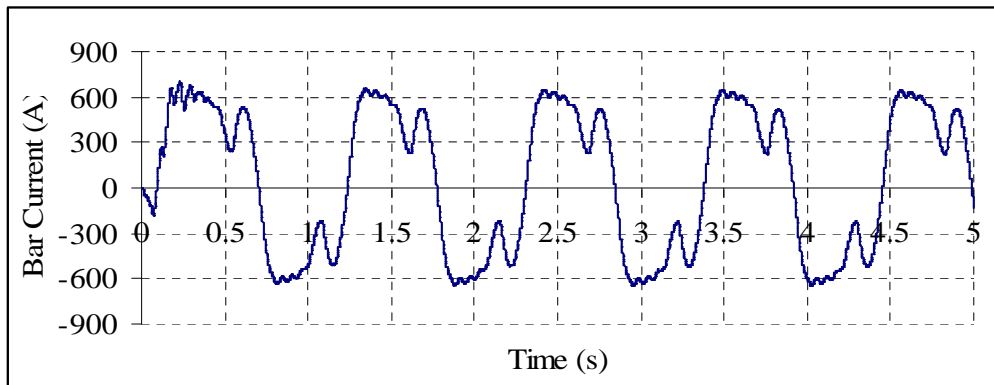


Figure 4-20. FEA simulated rotor bar current waveform of the 9-phase induction machine.

4.8.5 Torque

The torque predicted by the analytical method is shown in Figure 4-21 with a steady-state value of 58.9 Nm. The FEA predicted torque is shown in Figure 4-22 and its average steady-state torque is 58.5 Nm. This is very close in agreement with the analytical calculated torque. The first couple of seconds in the figures show the stabilising of the software solution (they do not show the transient response). A high steady-state torque ripple is observed in Figure 4-22 together with a high frequency ripple resulting from the slotting effects. An investigation of the torque ripple is not part of this study.

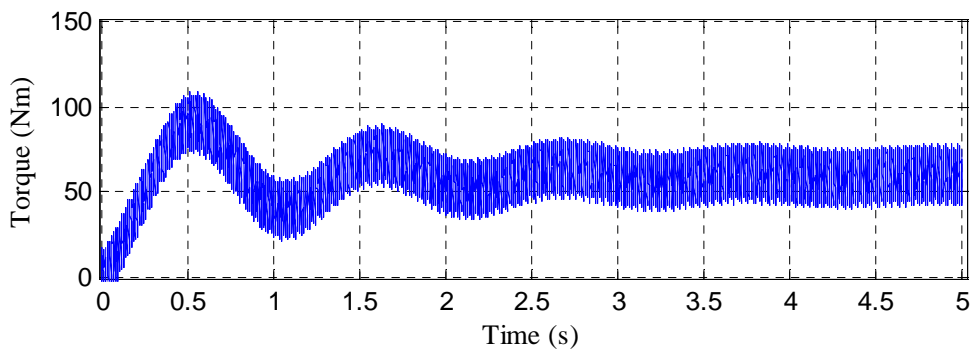


Figure 4-21. Analytically calculated torque of the nine-phase induction machine.

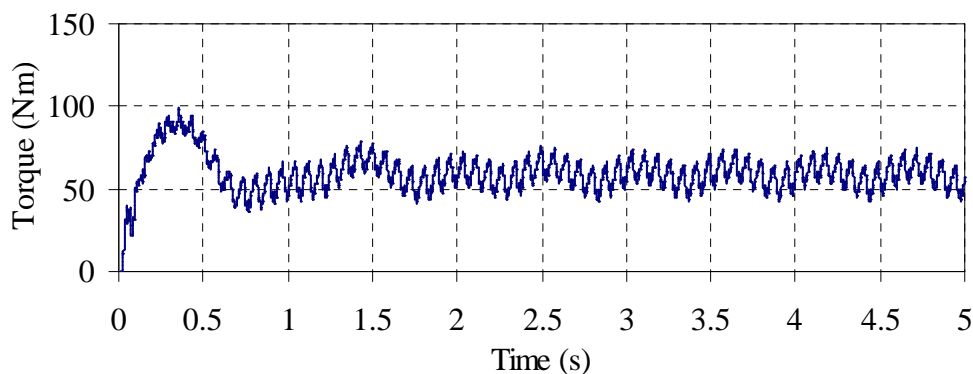


Figure 4-22. FEA predicted torque waveform of the nine-phase induction machine (unskewed rotor).

4.8.6 Rotor copper loss

The instantaneous bar and end ring currents can be used to calculate the instantaneous rotor copper losses of the machine. Using the analytical method, the rotor copper losses are calculated and are

shown in Figure 4-23. The average value of the losses is 150.0 W. Figure 4-24 displays the machine’s rotor copper losses from FEA, with an average value of 117.3 W. This is quite different from the value calculated through the analytical method. The difference can be explained by the assumptions made in the analytical approach. It is noted that in the FEA, the current waveform is applied in its trapezoidal form, whilst in the theoretical approaches, the Fourier expansion is used with limited harmonics. Also, linear conditions are assumed in the theory, whilst the FEA considers non-linear conditions. Again, the stabilising of the software solution is visible in the figures.

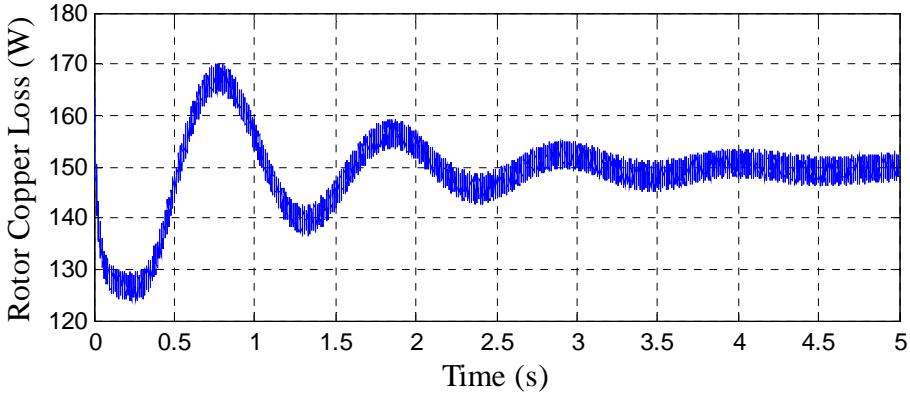


Figure 4-23. Rotor copper losses of the nine-phase induction machine calculated by the analytical method.

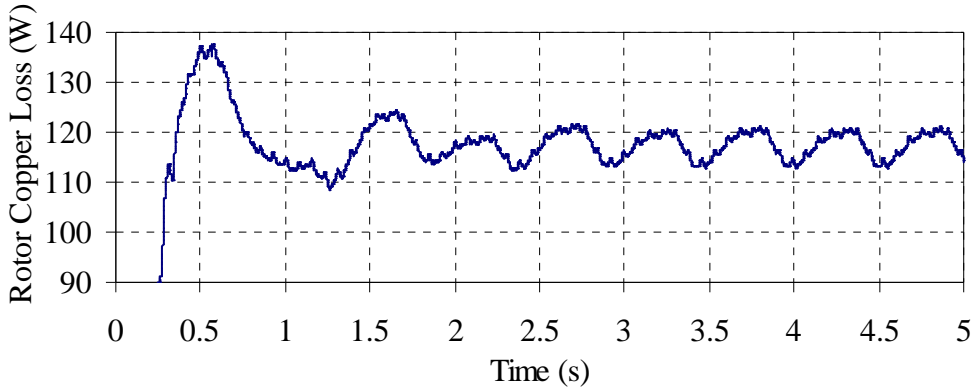


Figure 4-24. FEA calculated rotor copper loss of the 9-phase induction machine.

4.9 Summary

In this Chapter, an analytical method that can be used to evaluate the performance of multiphase induction machines under BDCE control is presented. The method can be used to predict and evaluate the shape of the rotor bar and end ring current waveforms of the machine. Theoretical and FEA calculated results of a nine-phase induction machine supplied with the trapezoidal stator currents are presented. Although linear conditions are assumed in the analysis, the results are sufficient to show the machine’s behaviour when excited with the trapezoidal current waveforms. Another analysis technique based on the equivalent circuit approach is described in Appendix E.

Chapter 5

Design and Test Setup of Experimental Nine-Phase Induction Motor Drive System

5.1 Introduction

In the previous Chapters, the theoretical analysis of the induction machine that is excited by trapezoidal current waveforms is provided. The design of the Rogowski current transducer, nine-phase induction machine, nine-phase inverter and the experimental setup are described in this Chapter.

5.2 Rogowski Coil Current Transducer

The Rogowski current transducer is appropriate for the rotor bar current measurement mainly because it is easy to install the Rogowski coil on the rotor cage. It consists of the coil, the integrator and the interconnecting coaxial cable. A split-flex coil with simple nylon clips forming a 70 mm radius is sufficient for this application. This allows the coil to be unplugged during installation and then clipped back. Integration is performed through the use of a microcontroller. The output voltage equivalent to a maximum current of 800 A is set to 10 V and the supply voltage to the integrator is 24 V. In addition, a Mercotac contactor is put in between the coil and the integrator to allow current measurement whilst the rotor is rotating. The Mercotac contactor is a perfect substitute for a slip ring and is commercially available. The transducer is calibrated and tested. The measured current is then displayed on an oscilloscope. Figure 5-1 shows a schematic of the Rogowski current transducer. A picture of the developed Rogowski current transducer is shown in Figure 5-2.

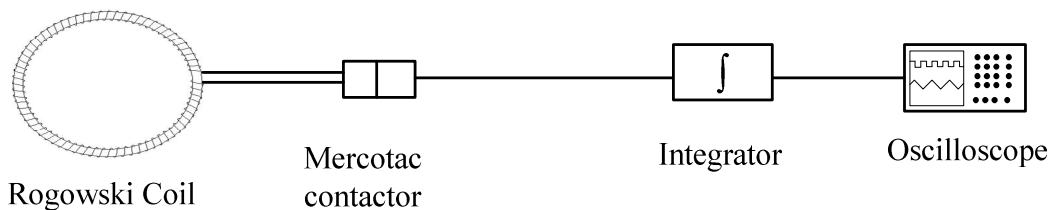


Figure 5-1. Schematic of the Rogowski current transducer.

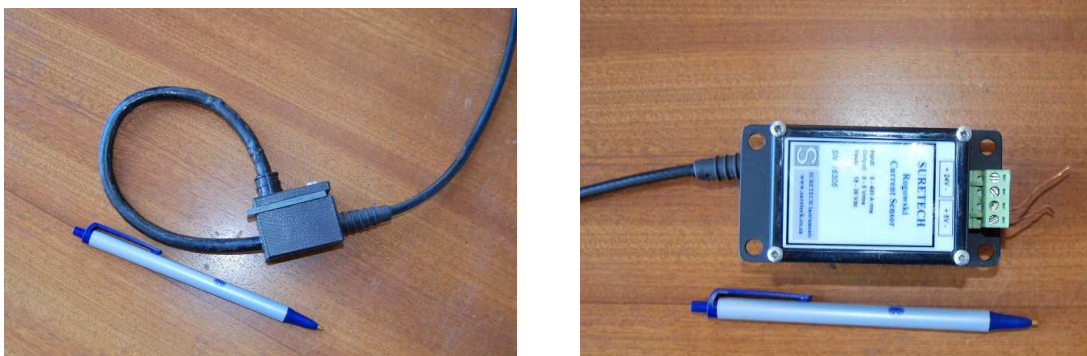


Figure 5-2. Rogowski Coil and integrator box.

5.3 Nine-phase Induction Machine

The design of a nine-phase induction machine with four poles and 11 kW power rating is described in this section. Included is the design of the nine-phase induction machine stator winding and the design of a rotor that is used for the rotor bar and end ring measurement. A commercially available (standard) three-phase, four pole, 11kW induction machine is suitable for rewinding to form a nine-phase, four pole induction machine. The standard induction machine has 36 stator slots and 28 rotor slots. The stator and rotor laminations of the induction machine are shown in Figure 5-3.

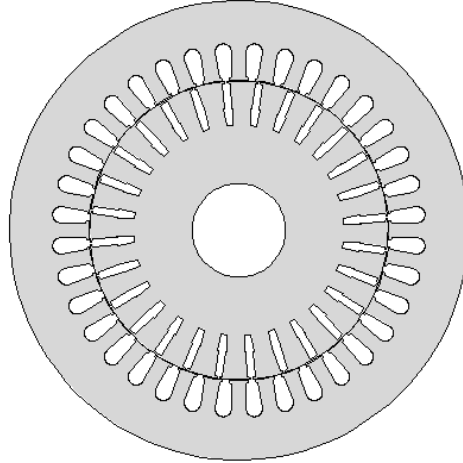


Figure 5-3. Stator and rotor laminations of an off-the-shelf 11 kW three-phase induction machine.

5.3.1 Stator winding

Since there are 36 stator slots in the standard four pole induction machine, assigning one coil per slot per phase per pole leads to a nine-phase four pole induction machine. The induced stator phase voltage under BDCE control has a quasi-square waveform. The dc flat-topped voltage-value of this waveform is given by,

$$\begin{aligned} E_s &= 2BN_s l r_g \omega_m \frac{P}{a} \\ &= \frac{2}{a} BN_s l r_g \omega, \end{aligned} \quad (5-1)$$

where a is the number of parallel circuits, $\omega_m = \omega/p$ and the number of turns per stator phase, N_s , can be calculated as

$$N_s = \frac{E_s}{2Blr_g \omega}, \quad (5-2)$$

where $a = 1$, B is the air-gap flux density, l is the stack length, r_g is the machine radius at the centre of the air-gap and $\omega = 2\pi f$; f is the fundamental electrical frequency at which the machine operates. The values of the variables in the above equation are given in Table 5-1. From this, the number of turns per stator phase, N_s , is calculated as 170. A fill factor, k_{fill} , of 0.5 is assumed from which the stator coil wire diameter, d_{wire} , is calculated as

$$d_{wire} = \sqrt{\frac{4S_A k_{fill}}{\pi N_s / 2}}, \quad (5-3)$$

where S_A is the stator slot area. Substitution gives $d_{wire} = 1$ mm. Based on the sequence of the nine-phase trapezoidal current waveforms, the stator winding layout is as shown in Figure 5-4. In the figure, the direction of current at this particular instance is represented by dots and crosses, whereby, a

dot represents current flowing out of the page and a cross represents current flowing into the page. The coil sides are labelled from A to I. A picture of the rewinded stator is shown in Figure 5-5. The stator lot geometry of the induction machine is shown in Figure 5-6. The dimensions of the stator slot are given in Table 5-2, whereby, the variables are as defined in Figure 5-6. (Note that the back-emf dc voltage of a phase winding for the machine is designed to be $E_s = 800$ V at 50 Hz whereby the coils are connected in series. However, during measurements, the stator coils are connected in parallel and then $E_s = 400$ V at 50 Hz and the phase current doubles. Then in this scenario, I_f and I_t represent the coil current. The high value of $E_s = 800$ V was due to a manufacturing error. Initially, the design was at $E_s = 400$ V (with coils in series) but during the rewinding, the number of turns per phase was wound as turns per coil, thus doubling the E_s .)

Table 5-1: General design data.

E_s	B	l	r_g	f
800 V	0.7 T	0.127 m	0.0848 m	50 Hz

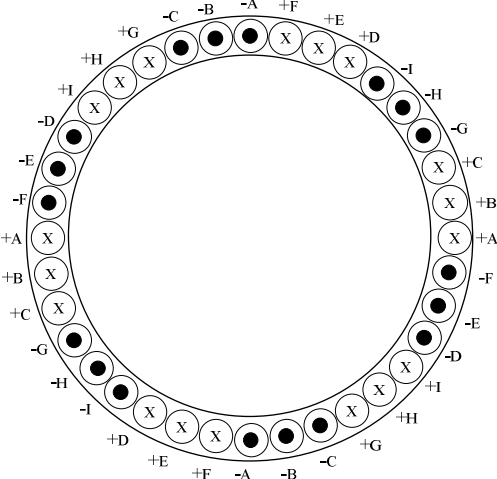


Figure 5-4. 9-phase, 4-pole induction machine stator winding layout.

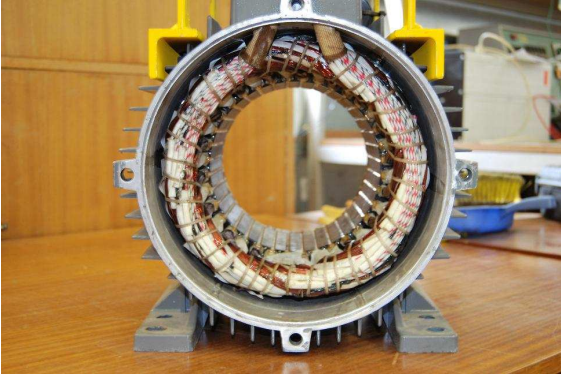


Figure 5-5. Stator of the nine-phase induction machine.

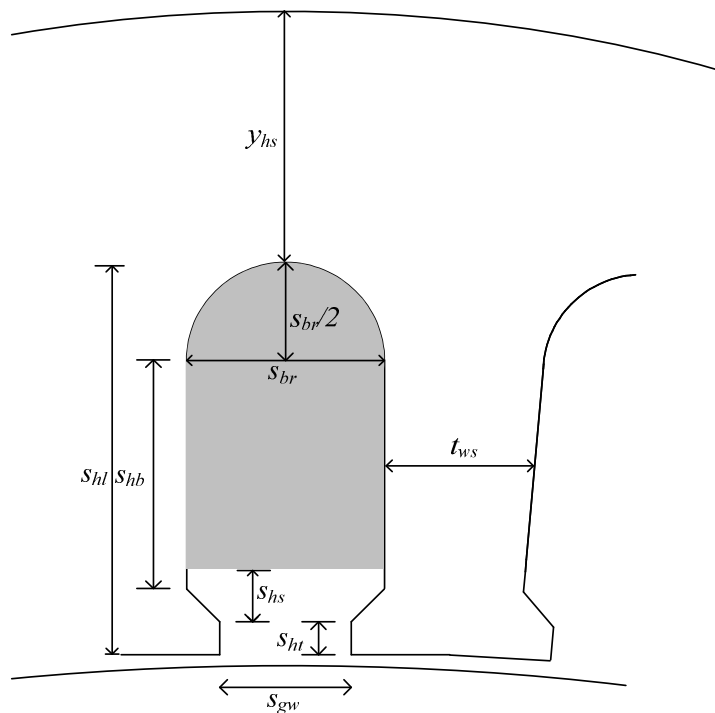


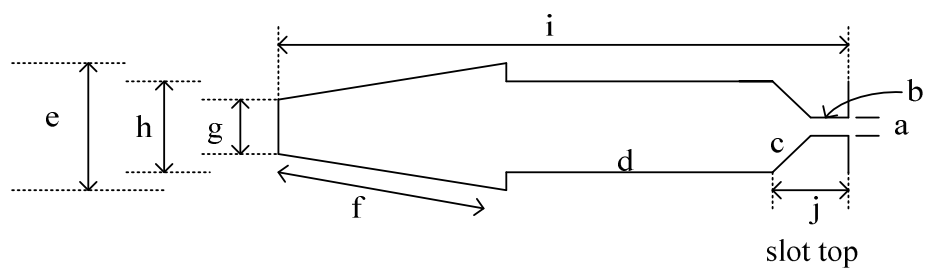
Table 5-2. Stator slot variables.

Variable	Length (mm)
s_{ht}	1.0
s_{hs}	2.0
s_{br}	9.2
s_{hb}	12.6
s_{gw}	3.8
y_{hs}	24.8
s_{hl}	20.2
t_{ws}	8.15

Figure 5-6. Stator slot geometry.

5.3.2 Standard rotor winding

The standard induction machine rotor has 28 slots and a cast aluminium cage. The rotor slot shape and dimensions are given in Figure 5-7.



Edge	length (mm)
a	1
b	1
c	2
d	13.67
e	5.15
f	8.82
g	3.25
h	4.5
i	25
j	1.65

Figure 5-7. Slot shape and dimensions of the standard cage rotor.

5.3.3 Special rotor for current measurement

The rotor bar current measurement is essential in order to verify the developed analytical model. However, it is not possible to measure the bar current on a cast aluminium rotor. Therefore, a custom manufactured rotor is required for the purpose of measuring the current in the cage winding. This rotor must allow easy fit of the Rogowski coil. A general rectangular rotor slot is arbitrarily chosen because of manufacturing simplicity. From the main dimensions of Figure 5-7, the slot breadth and depth is chosen to be 4.5 mm and 25 mm respectively. The selected total number of slots is 28 as in the standard cage rotor. For ease of manufacturing, copper is selected over aluminium for the rotor cage winding. The copper bars are slightly longer than the lamination stack in order to fit the Rogowski coil. A groove on the shaft is designed for the coaxial cable to pass underneath the induction machine case bearing from the Rogowski coil on the rotor to the integrator outside the induction machine. Figure 5-8 shows the rotor schematic and Figure 5-9 shows the new rotor lamination, lamination holder and end ring of the new rotor. Pictures of the rotor without copper bars are shown in Figure 5-10. Figure 5-11 shows the photo of the rotor with copper bars and the Rogowski coil mounted on the

end ring. The Rogowski coil is mounted on the end ring or on the bar in order to measure the end ring or the bar current.

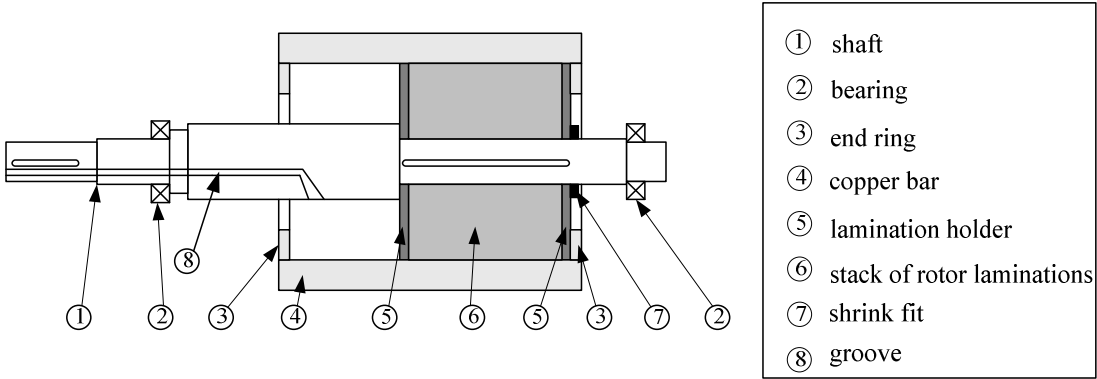


Figure 5-8. Schematic of the new rotor.

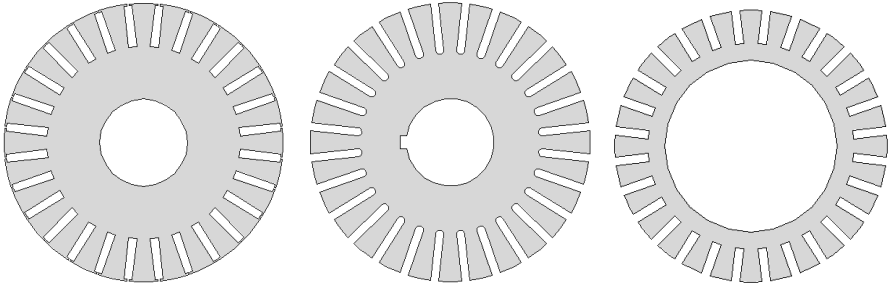


Figure 5-9. From left to right: new rotor lamination, lamination holder and end ring.



Figure 5-10. Developed rotor without rotor bars.

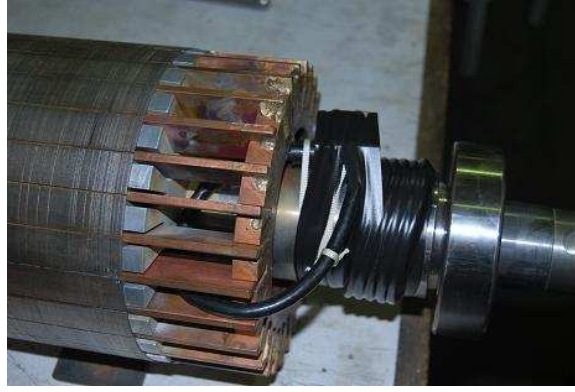


Figure 5-11. Rotor with Rogowski coil fitted on the end ring.

5.3.4 Other design and performance parameters

Using the method described in section 1.1, the air-gap flux density versus field current relationship is obtained for the nine-phase machine and plotted in Figure 5-12. The torque current is zero and the number of field phases is three. It is observed from the figure that an air-gap flux density of 0.7 T corresponds to a field current of 5.83 A.

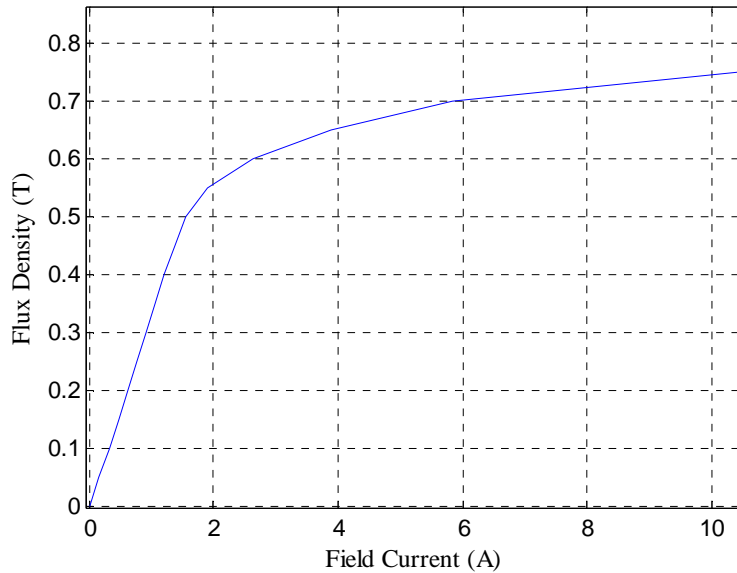


Figure 5-12. Relationship between flux density and field current.

In order to find the machine rated operating speed and rated torque current, an equation of the static torque of the machine based on the method described by [58] is first derived from the rotor bar current. The square like shaped air-gap flux density leads to a square like induced voltage waveform in the rotor bar, as previously shown. The flat-topped amplitude of the induced bar voltage, E_b , is given by

$$E_b = 2N_r B l \omega_{sl} r_g, \quad (5-4)$$

where N_r is the number of turns per rotor phase ($N_r = 0.5$ for a squirrel cage winding), B is the air-gap flux density, l is the stack length, ω_{sl} is angular slip frequency and r_g is the air-gap radius. The dc flat-topped induced rotor bar current is then given by

$$I_r = \frac{E_b}{R_b} = \frac{2N_r B l \omega_{sl} r_g}{R_r}, \quad (5-5)$$

where, R_b is the dc bar resistance and the bar inductance is neglected (the end ring resistance is ignored in this analytical calculation). Theoretically, the number of active bars per pole is

$$m_{ra} = \frac{M_r (m_t - 1)}{2N_p p}, \quad (5-6)$$

where M_r is the number of rotor bars, m_t is the number of torque phases, N_p is the total number of stator phases and p is the number of pole pairs. Therefore, the torque of the machine can be calculated by using the Lorentz force law and is given by

$$T = 4p m_{ra} N_r B l r_g I_r, \quad (5-7)$$

and the amplitude of the rotor air-gap MMF is given by

$$F_r = m_{ra} N_r I_r. \quad (5-8)$$

MMF balance between the torque MMF and the rotor MMF ($F_r = F_t$) is assumed, as this is a requirement for the operation and control of the machine using the trapezoidal current waveforms. It can be shown from the phase current waveforms of Figure 4-7 and the winding layout of Figure 4-8 that the amplitude of the stator torque MMF produced by the m_t torque phase winding at any instant is

$$F_t = \frac{(m_t - 1) N_s I_t}{2p}, \quad (5-9)$$

where, N_s is the number of series turns per stator phase and I_t is the stator torque current amplitude. Then, the stator torque current is given by

$$\begin{aligned} I_t &= \frac{2p m_{ra} N_r I_r}{(m_t - 1) N_s} \\ &= \frac{4p m_{ra} N_r^2 B l \omega_{sl} r_g}{(m_t - 1) N_s R_r}. \end{aligned} \quad (5-10)$$

The relationship between I_t and ω_{sl} is therefore given by

$$k = \frac{\omega_{sl}}{I_t} = \frac{(m_t - 1) N_s R_r}{4p m_{ra} N_r^2 B l r_g}. \quad (5-11)$$

It is clear that k depends on the bar resistance R_b and the air-gap flux density B . Since the value of k is dependent on the bar resistance, which in turn is dependent on temperature, a machine designer must know the operational temperature of the machine precisely before calculating the value of k . B can be controlled through the field current, I_f . From equations (5-7) and (5-10), the torque can also be expressed as,

$$T = 2(m_t - 1) N_s I_t B l r_g. \quad (5-12)$$

Hence, under balanced MMF conditions, the electromagnetic torque is directly proportional to the torque current. Rated torque is equal to 70 Nm for the induction machine and therefore I_t is calculated from (5-12) and found to be 5.5 A. The slip speed can then be calculated from (5-10). The full load slip is found to be 2.23 % and the rotor current amplitude equals 600 A. It is noted that the rotor bar

calculations in this case ignore frequency dependency and also the calculation is for a bar resistance at 75 °C. Other machine parameters are given in Table 5-3. L_e and R_e are calculated as described in Appendix C.

Table 5-3. Nine-Phase Machine Data.

N_r	0.5
B	0.7 T
l	0.127 m
r_g	0.08475 m
R_e	$1.28 \times 10^{-6} \Omega$ (at 75°C)
L_{er}	2.92×10^{-8} H
m_f	3
m_t	6
m_r	28
p	2
N_s	170
I_t	5.5 A
I_f	5.83 A
a	1
<i>speed</i>	1466 r/min
k	0.638 rad/As

5.4 Inverter design

The inverter comprises of Intelligent Power Modules (IPMs), the control and isolated power circuits, the bus bar and per phase current sensors. Modular design allows independent testing and simple replacement of faulty boards. A description of the important inverter components is given in the following sections.

5.4.1 Intelligent power module (IPM)

The IPM is selected for this application due to its superior advantages compared to conventional insulated-gate bipolar transistors (IGBTs). It helps in simplifying the design and development through the integration of the drive and protection circuitry into one compact casing. Other IPM features include: low power loss, soft switching and high reliability. The IPM selected here is the 6MBP25RA120 due to availability and also re-usability in multiphase induction machine applications because of its high voltage rating. The block diagram of this IPM is shown in Figure 5-13. Some of the functions of the pre-drivers are: amplifier for driver, short circuit protection, under-voltage lockout circuit, over-current protection and IGBT chip over heating protection. The IPM has three phase arms. It has a voltage rating of 1200 V and a current rating of 25 A.

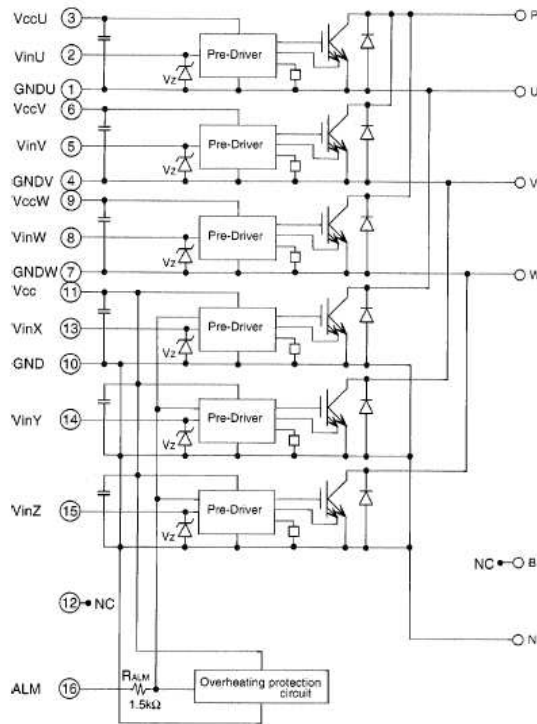


Figure 5-13. Block diagram of the 6MBP25RA120 IPM.

5.4.2 Control modules and power modules

The IGBT power switches in the IPM are active low. Therefore, the input pin of the IPM is pulled high with a resistor connected to the positive side of the control power supply. Then, an ON signal is generated by pulling the control input low. Isolation is provided through the use of optocouplers. An H-bridge is needed for each stator phase (two legs per phase). With three phase arms per IPM, the layout of the interface modules for control signals is such that two IPMs are used to control three phases as shown in the diagram shown in Figure 5-14. A single control signal is used to control (that is switch on / off) the top switch of the first leg as well as the bottom switch of the second leg of the H-bridge. The inverse of this signal is used to control the bottom switch of the first leg and the top switch of the second leg of the H-bridge. Each IPM requires four isolated 15V power supplies for its internal drive and protection circuits. Figure 5-14 also shows the three stator phase connections on two IPMs.

5.4.3 Nine-phase inverter

A high level block diagram of the nine-phase inverter is shown in Figure 5-15. Altogether six IPMs are used, with two IPMs per three phases. It is noted that two IPMs share the same control board. Two series connected dc-link capacitors are used at the input of each IPM and the rating for each capacitor is 450 Vdc and 470 μ F. Photos of the nine-phase inverter are shown in Figure 5-16.

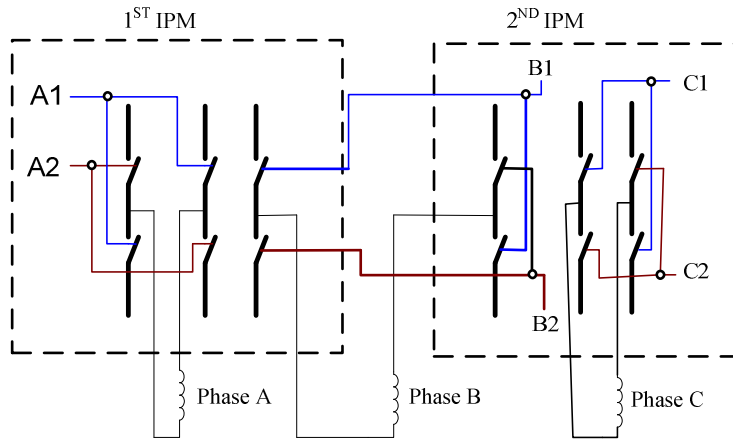


Figure 5-14. Schematic of the IGBT control signals and H – bridge connections.

9+

Figure 5-15. The nine-phase inverter block diagram.

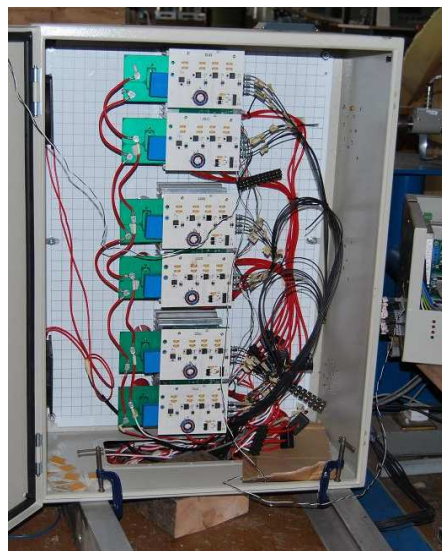


Figure 5-16. Nine-phase inverter.

5.4.4 Digital signal processor (DSP) control system

The functional diagram of the DSP control system is shown in Figure 5-17. The inputs into the system are the control program from the personal computer (PC), current data from the current sensors, the speed signal from the resolver and the torque current references, whilst the outputs are the pulse width modulated signals (PWM) and reference or measured data. The DSP chip produces the reference nine-phase current waveforms, executes the speed proportional integral (PI) controller after receiving data from the resolver and receives data from the PC. The field programmable gate array (FPGA) functions are: read the nine-phase current data from the analog to digital converters (ADC), execute the digital hysteresis current controller, calculate the duty cycle of the PWM signals and write the PWM signals to the electrically programmable logic device (EPLD). The digital hysteresis current controller is described in Appendix D. The EPLD is used to increase the PWM signals output pins since the FPGA

does not have enough pins for assigning the PWM signals to every power switch device. The oscilloscope is used to display measured or reference signals. Figure 5-18 shows a photo of the DSP controller.

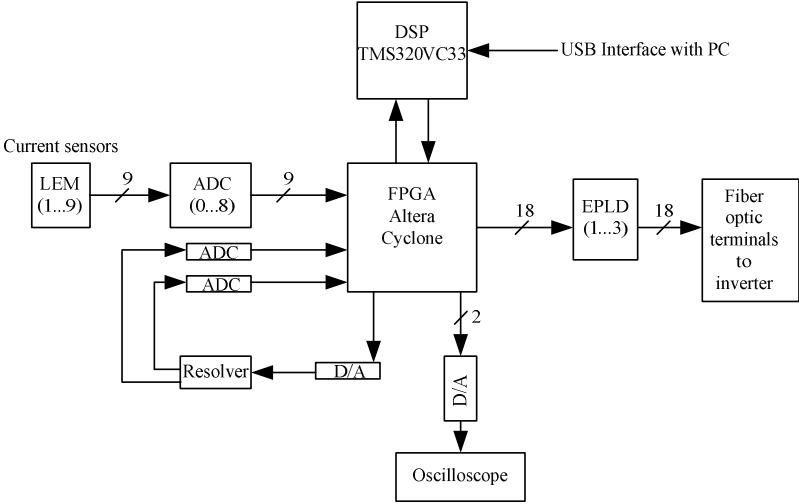


Figure 5-17. Functional diagram of the DSP controller.



Figure 5-18. DSP controller.

5.5 Nine-phase Drive System

The entire nine-phase drive system consists of the induction machine, the inverter and the DSP control system as shown in Figure 5-19. An appropriate value of I_f is set in the control program and an external reference is used for I_r . The value of k in the system is calculated through equation (5-11) and is kept constant. This value is used in the calculation of the angular slip frequency, ω_{sl} . The rotational speed of the induction machine is measured through the resolver attached to its shaft. A written software program is used to calculate the speed from the resolver signals and filter the measured speed. The sum of the angular slip frequency, ω_{sl} , and the measured angular rotor speed frequency, ω_r , gives the angular synchronous frequency. The electrical angle, θ , is then calculated from the synchronous rotational frequency through integration. Once the electrical angle is known, a lookup

table is used to evaluate the reference nine-phase stator currents. The actual currents measured through the current sensors are then compared with their respective reference currents, and PWM signals are produced to control the nine-phase inverter. The inverter then controls the nine-phase induction motor.

5.6 Experimental Setup

Figure 5-20 shows a schematic of the experimental setup built to test the nine-phase induction machine. A three-phase 37 kW induction machine is used as a load drive. During testing, the induction machine load drive is kept at a constant speed through the Powerflex 700 drive. The nine-phase DSP control system measures the rotor speed and produces the PWM signals that drive the inverter. The torque is measured through a torque transducer installed on the shaft linking the two machines. A photo of the machine on the test bench is shown in Figure 5-21.

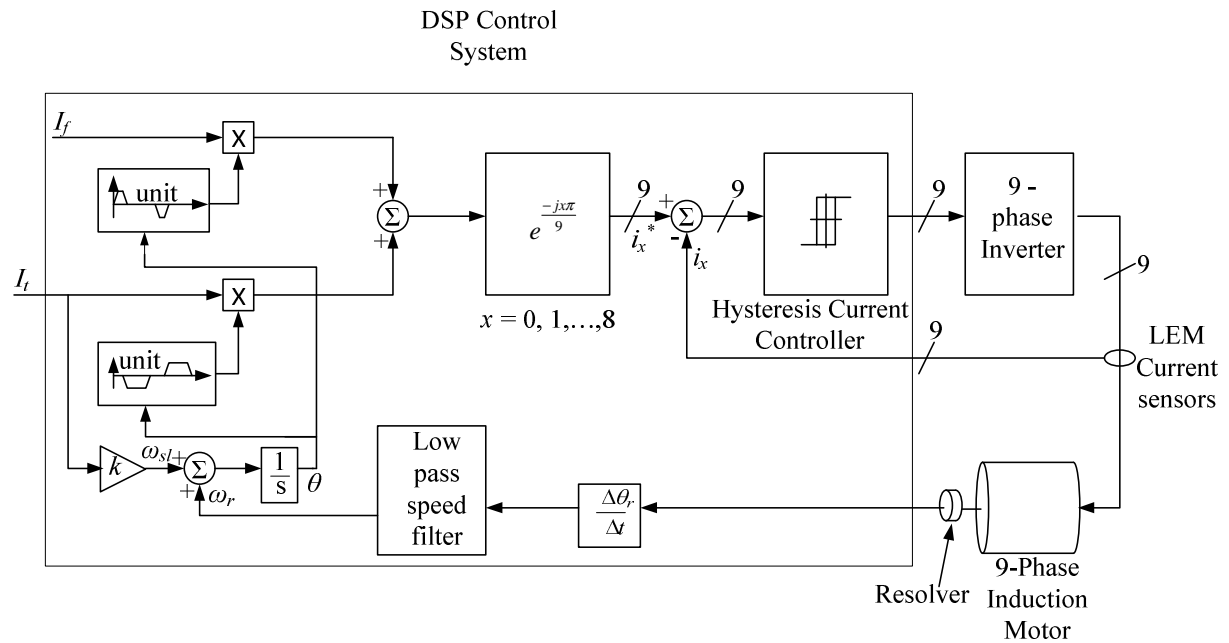


Figure 5-19. The nine-phase drive system.

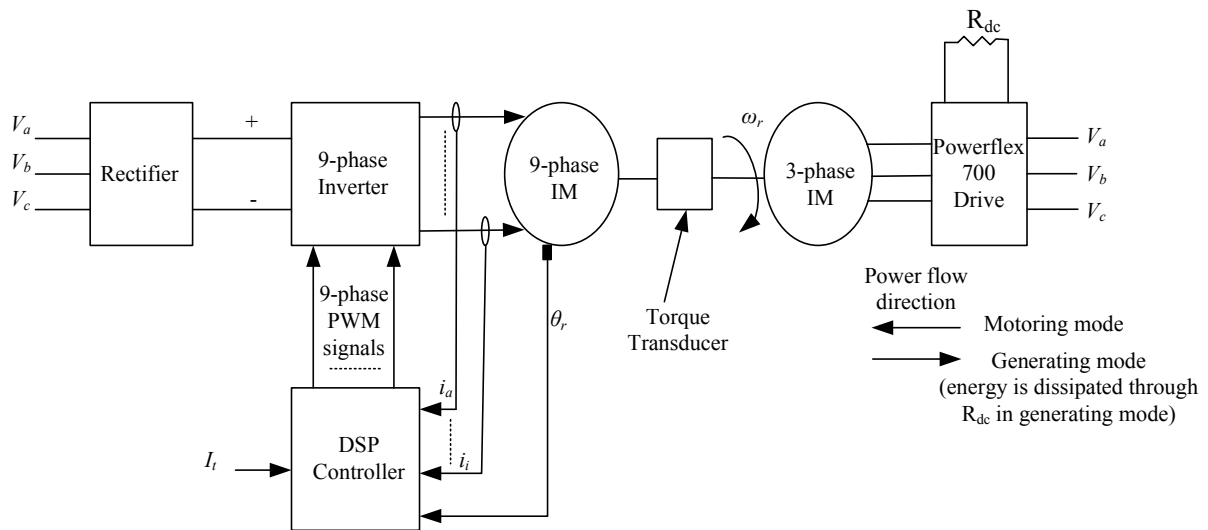


Figure 5-20. Test bench setup schematic.

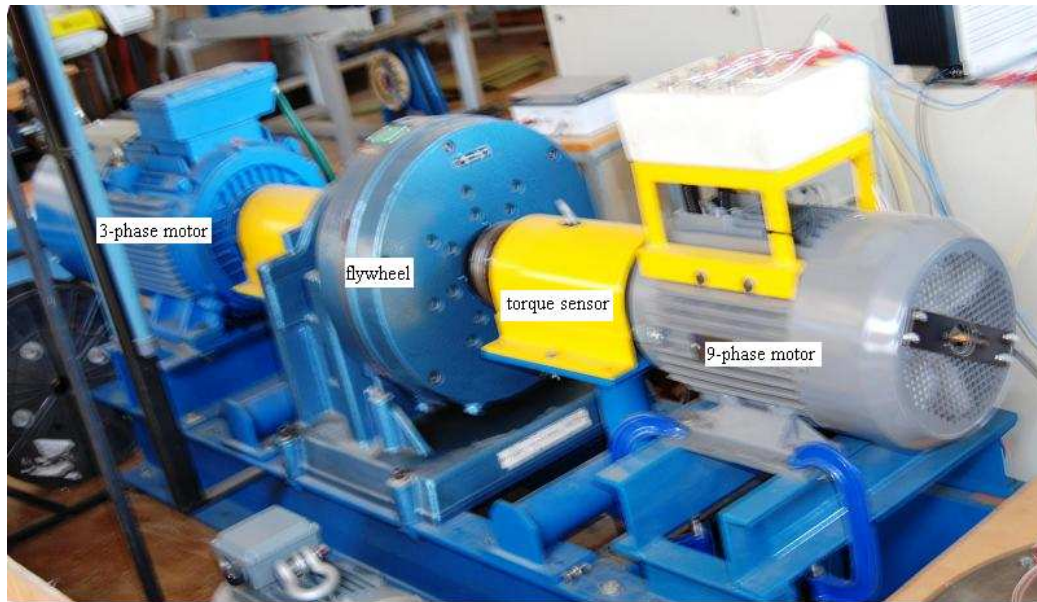


Figure 5-21. Nine-phase induction machine on the test bench.

5.7 Summary

In this chapter a description of components that make up the nine-phase drive system were provided. The Rogowski current transducer used in the measurement of the rotor bar and end ring currents was presented. A detailed description of the nine-phase induction machine was also given in this chapter. Practical considerations led to the selection of the nine-phase induction machine. Two rotors were described: one strictly designed for rotor current measurement whilst the other is the standard three-phase machine rotor used in the performance measurement of the nine-phase induction machine. The stator dimensions of the standard three-phase machine were described together with the design of the nine-phase stator winding. The slip and the control gain value, k , are calculated. The design of the nine-phase inverter and its components is given in detail. Finally the test setup of the nine-phase drive is also presented. Photos of the component and systems are also presented. The analytically calculated and experimental results of the machine designed in this chapter are provided in Chapter 6.

Chapter 6

Calculated and Measured Results

6.1 Introduction

This chapter contains theoretical and measured results of the nine-phase induction machine drive described in Chapter 5. The theoretical results include both analytically calculated and FEA results from Maxwell2D as described in Chapter 4. Measurement results presented here include: rotor bar and end ring current waveforms, torque and efficiency of the drive system. Once the analytical method results are validated through FEA and measurements, the rotor current waveform at rated slip is predicted analytically and through FEA. The relationship between the torque and torque current of the machine is verified through measurements in the constant flux and flux weakening speed regions. The ratios of generated torque to rotor copper losses are presented with the machine supplied with sinusoidal currents and compared to when supplied with the proposed trapezoidal stator currents.

6.2 Calculated Current Waveforms

Analytically calculated and FEA results are provided in this section. For all the results in this section, the rated value of $I_f = 5.83$ A is used unless stated otherwise. The results provided in this section are to show that the analytical method can be used to predict the shape of the rotor current waveform under different shapes of stator current waveforms. The finite element model of the nine-phase induction machine with the special rotor is shown in Figure 6-1. Only a quarter of the machine is modelled in the FEA as stated in section 4.7.

6.2.1 Rotor circuit loop current waveforms

In this section, the rotor loop current is presented. The special designed rotor with rectangular copper bars presented in section 5.3.3 is considered in the calculation of the rotor current. The current waveforms are calculated through the analytical method where the loop currents are as described in Figure 4-1; the loop currents are equal to the end ring current. FEA results are given in the next section. Documented equations are used in the end ring resistance and inductance calculations in the analytical method. Also the frequency dependence of the rotor bar resistance and inductance is considered through the use of the equations given in Appendix C. The waveforms of three consecutive rotor loop currents (i_{r1} , i_{r2} and i_{r3}) are shown in Figure 6-2 for different values of I_t and the rotor at standstill. The torque current amplitudes, I_t , for Figure 6-2 *a*), *b*), and *c*) are 0 A, 2 A and 4 A respectively. The phase shift between consecutive end ring segments / loops is as expected. The next section presents rotor bar currents calculated from the loop currents as given in equation (4-12).

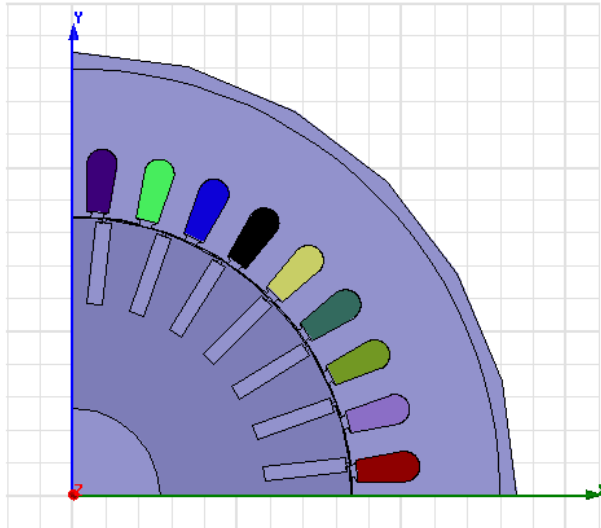
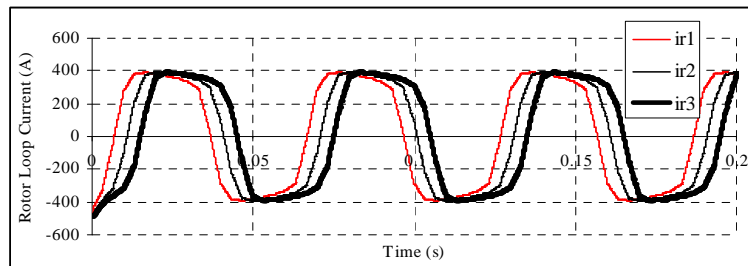
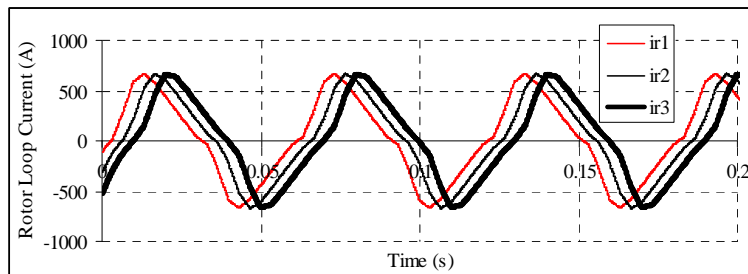


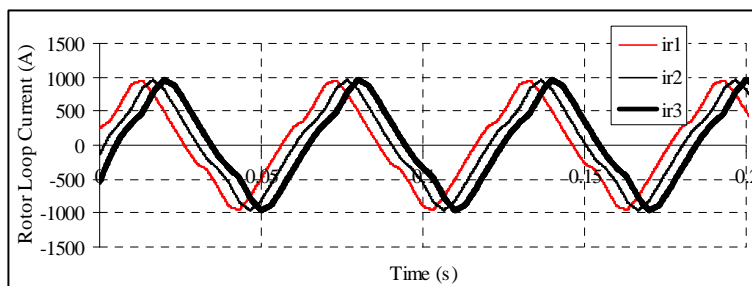
Figure 6-1. Finite element model of a nine-phase induction machine with the special rectangular copper bar cage rotor.



a)



b)



c)

Figure 6-2. Waveforms of the analytically calculated consecutive rotor circuit loop currents ir_1 , ir_2 and ir_3 at rotor standstill with the field current, $I_f = 5.83$ A and torque currents equal to a) $I_t = 0$ A, b) $I_t = 2$ A, and c) $I_t = 4$ A. The fundamental frequency of the stator current waveform is 16.67 Hz.

6.2.2 Rotor bar current waveforms

The special designed copper bar cage rotor is considered again in the evaluation of the rotor bar current waveforms and for the same conditions as given in Figure 6-2. Figure 6-3 shows the FEA and analytically calculated current waveforms of the n th rotor bar for different values of I_t . The bar current waveform seems to follow the stator phase current waveform. Furthermore, it is noted that the peak values obtained from the FEA are higher than those of the analytical calculation. This may be a result of different rotor bar resistance or inductance used in the FEA and analytical method. The equations used in the transient FEA software model are not known. It is clear that, the analytical method prediction of the rotor bar current waveform compares very well with the FEA.

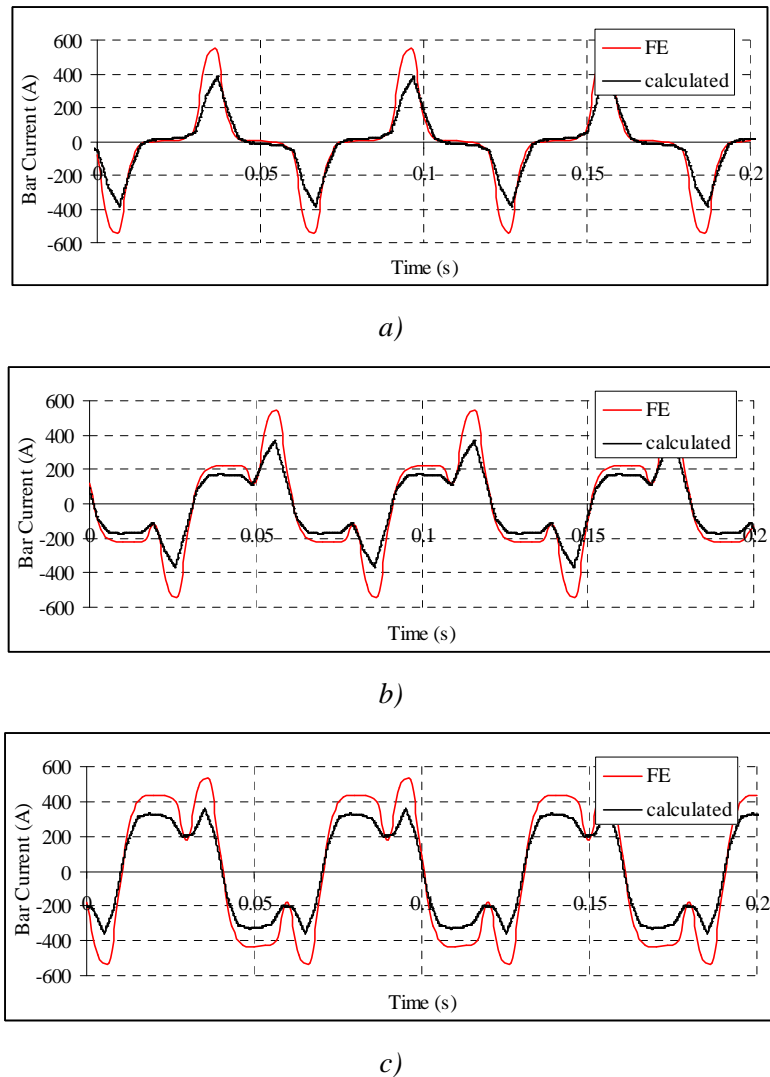


Figure 6-3. Analytically calculated and FE calculated rotor bar current at rotor standstill with $I_f = 5.83$ A and torque currents equal to, a) $I_t = 0$ A, b) $I_t = 2$ A, and c) $I_t = 4$ A. The fundamental stator frequency is 16.67 Hz.

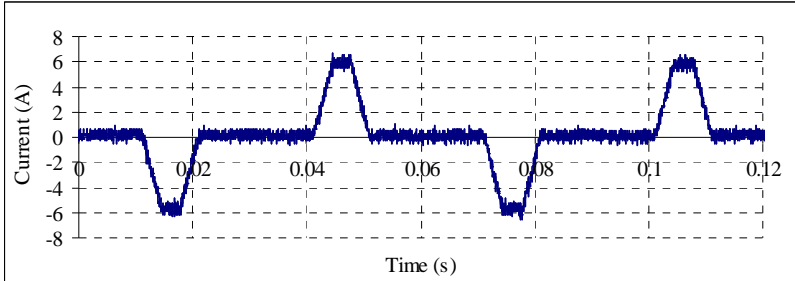
6.3 Measured Current Waveforms

This section presents the measured stator, rotor bar and end ring current waveforms. The aim of these measurements is to validate the analytical method experimentally. Torque is not a concern in the current waveform measurements as this is merely a demonstration of the effectiveness of the control system. Torque measurements are presented in section 6.4. The assembled rotor that is specially designed for current measurements is installed in the nine-phase machine, and the rotor currents are measured using the Rogowski current transducer with the Rogowski coil installed in the rotor. The

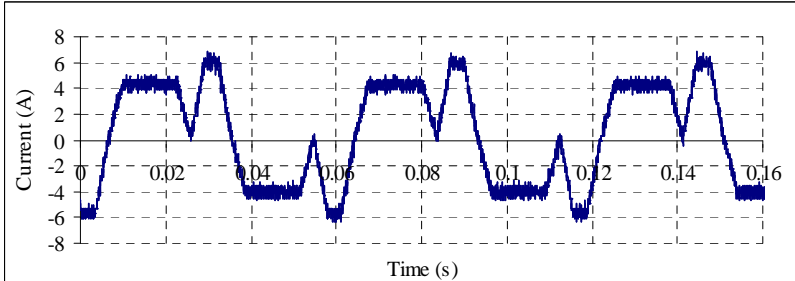
Rogowski coil is installed in the rotor bar or end ring depending on the current being measured. The rotor is locked during the rotor bar and end ring current measurements. The measured current waveforms are compared to the analytically evaluated current waveforms presented in the previous section. Similar to the previous section, the rated value of $I_f = 5.83 \text{ A}$ is used with the stator current fundamental frequency at 16.67 Hz. Since the rotor is locked during measurements, the rotor current frequency is also 16.67 Hz. The stator phase current measurements are measured through a current transducer connected to an oscilloscope.

6.3.1 Inverter output current waveforms

Before measurements are taken, it is necessary to validate the nine-phase inverter output current waveform that is fed to the stator of the machine. This is achieved by measuring the stator current waveform. For demonstration purposes, a measured single stator phase current waveform is shown in Figure 6-4 at different torque current values. The waveform shows the effectiveness of the digital hysteresis current controller, since the desired waveform is measured. In Figure 6-4, the field current average amplitude is 5.83 A whilst the average torque current amplitudes are 0 A and 4.0 A for *a)* and *b)* respectively. The nine-phase inverter and control system are validated by these waveforms. Measured stator phase current waveforms at rated and high speeds are presented in section 6.4.



a)

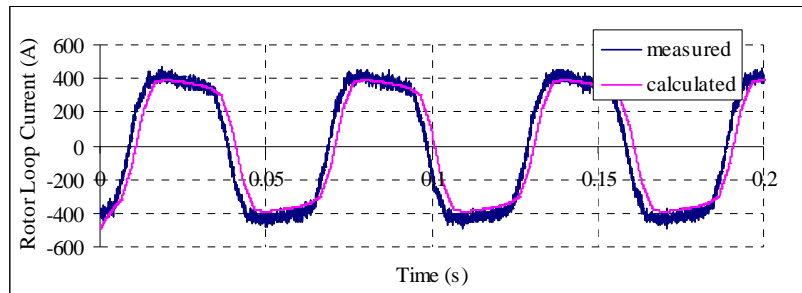


b)

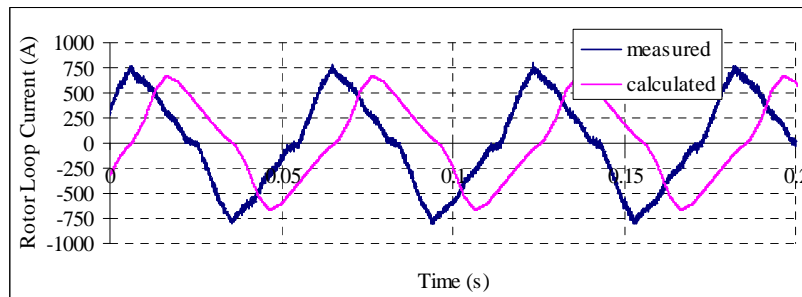
Figure 6-4. Measured stator phase current waveforms at rotor standstill with the fundamental stator current frequency at 16.67 Hz, $I_f = 5.83 \text{ A}$ and *a)* $I_t = 0 \text{ A}$, and *b)* $I_t = 4 \text{ A}$. Note: these waveforms are for demonstration purposes only and have nothing to do with the actual control of the machine.

6.3.2 Rotor loop / end ring current waveforms

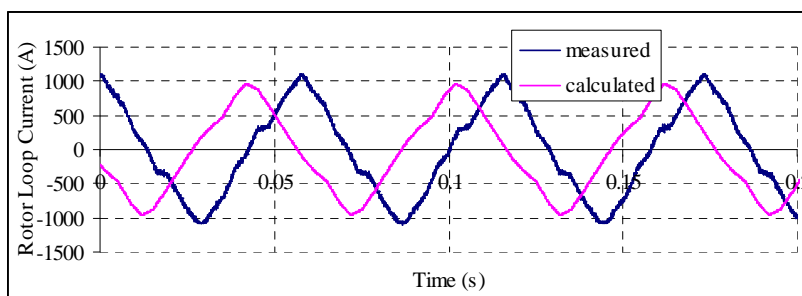
The measurements in this section are taken with the Rogowski current transducer with the Rogowski coil installed on the end ring of the specially designed rotor. The measured and analytical-calculated end ring current waveforms are very similar as shown in Figure 6-5. Therefore, the measured results validate the analytical method.



a)



b)

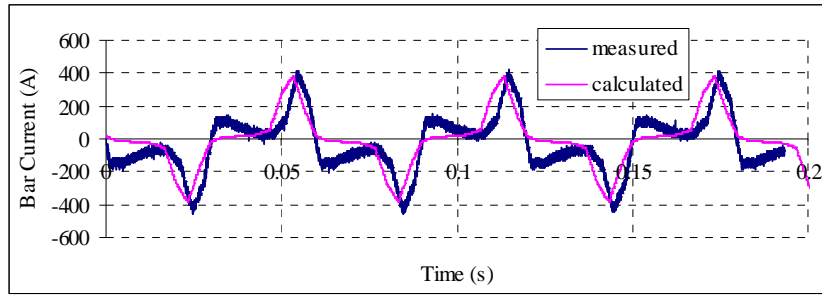


c)

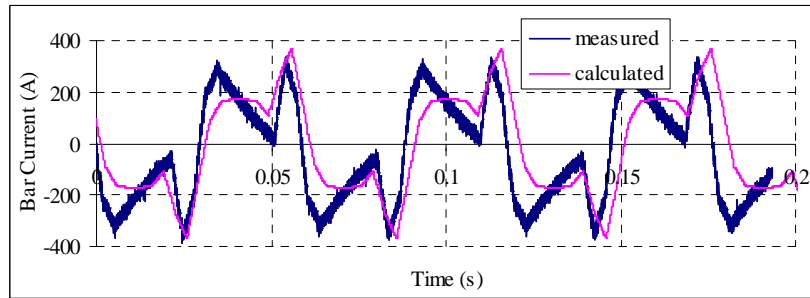
Figure 6-5. Comparison of measured and analytically calculated end ring current waveforms at rotor standstill with the fundamental stator current frequency at 16.67 Hz, $I_f = 5.83$ A and a) $I_t = 0$ A, b) $I_t = 2$ A, and c) $I_t = 4$ A.

6.3.3 Bar current waveforms

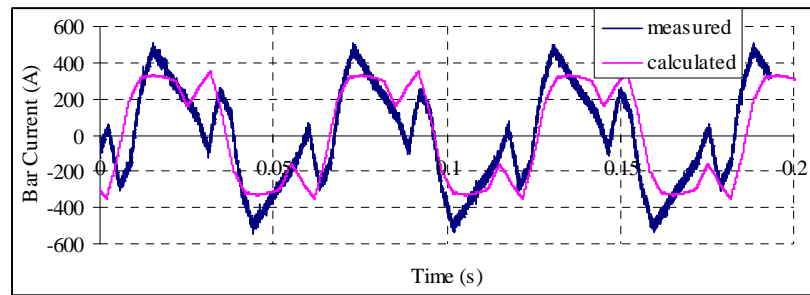
For the measurements in this section, the Rogowski coil is installed on a bar of the specially designed rotor. The measured and calculated rotor bar current waveforms are shown in Figure 6-6. There is an observable and good similarity between the waveforms. The cause of the peaks in the measured current waveforms is not clear.



a)



b)



c)

Figure 6-6. Comparison of measured and calculated rotor bar current waveforms at rotor standstill with the fundamental stator current frequency at 16.67 Hz, $I_f = 5.83$ A and a) $I_t = 0$ A, b) $I_t = 2$ A, and c) $I_t = 4$ A.

6.3.4 Rotor bar current waveform at rated speed

In the previous sections, the rotor bar current waveform has been verified through FEA and measurements whilst the rotor is at standstill. In this section, the analytical method is used to calculate the rotor current waveform with the machine operating at the rated speed and under balanced MMF conditions. The rotor bar current waveform at rated speed of the nine-phase induction machine is shown in Figure 6-7. This differs from the square wave assumption also shown in the figure. At this moment, it is not known why the bar current waveform from the analytical method is lower than the others. The difference between the assumed waveform and the calculated waveform may not be simply due to transformer action in the machine, since the amplitude of the supposed field current component is lower than that of the torque component, which is in contrast to the stator current waveform. The difference may be due to commutator action in the machine. It is clear that there is current flowing under the field phases as opposed to the ideal assumption of no current flowing. In dc machines, a similar effect is suppressed through the introduction of interpoles. A further investigation of the current waveform is recommended.

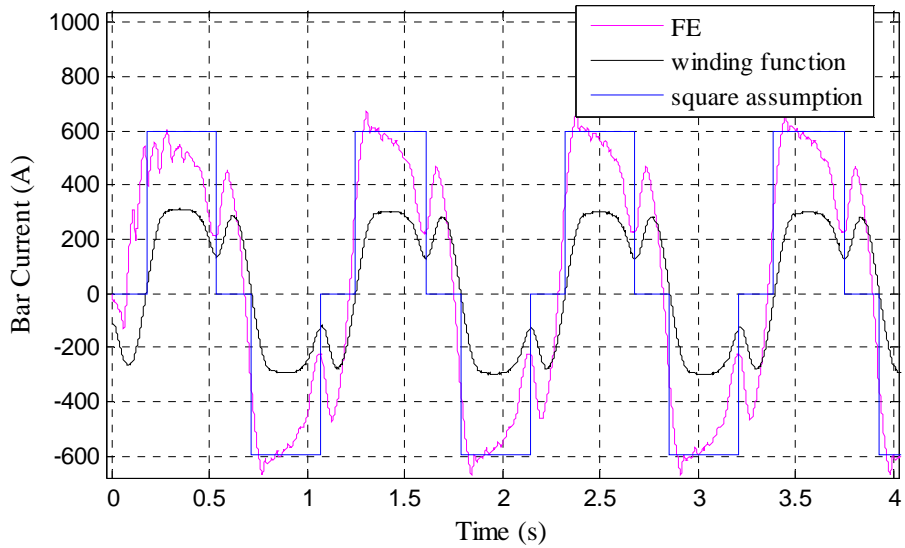


Figure 6-7. Different calculated rotor bar current waveforms with the machine running at rated operating speed of 1466 r/min, $I_f = 5.83$ A and $I_t = 5.5$ A. The stator current is at 50 Hz.

6.4 Measured Torque and Efficiency

In this section, the measured, FEA and analytically calculated torque of the nine-phase induction machine excited with trapezoidal stator current waveforms are provided. Equation (5-12) is used to calculate the torque of the machine analytically. The measurements are for a nine-phase induction machine consisting of the rewinded nine-phase stator and the original standard cast aluminium cage rotor. It should be noted that the standard rotor is skewed, whilst skewing is not considered in the analytical calculation. However, the difference between the measured and analytically calculated results due to skewing is not expected to have a bearing on the conclusions. A quarter of the machine with the standard rotor is shown in Figure 6-8.

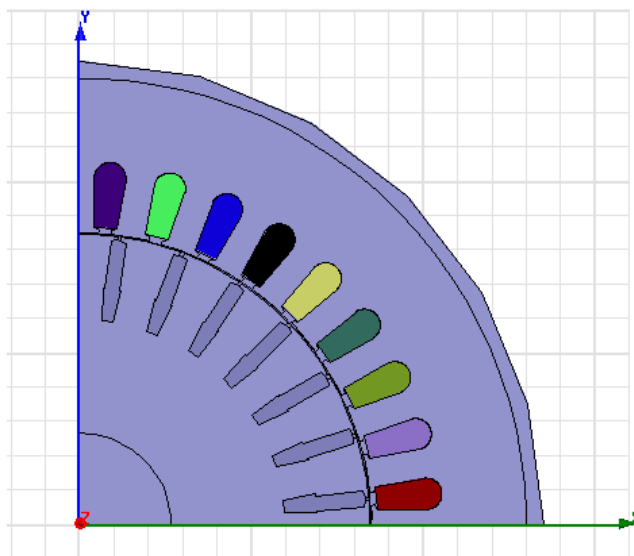


Figure 6-8. Finite element model of a nine-phase induction machine with the standard cast aluminium cage rotor.

6.4.1 Torque measurements at constant flux

In Figure 6-9, the comparison of the measured and analytically calculated torque results of the drive are shown at rated field current, $I_f = 5.83 \text{ A}$ and a rated control gain value, $k = 0.638$ (k is calculated from (5-11)). In this measurement, the rotor speed is 500 r/min. The analytically calculated results are evaluated through the static torque equation (5-12). Both results show a linear relationship between the torque current and the developed torque. The figure shows that at the rated torque current value ($I_t = 5.5 \text{ A}$), the measured and calculated torque values are more or less the same. Nonetheless, the result show that the drive maintains balanced MMF condition regardless of the torque current. This proves the BDCE operation (the similarity to brush dc operation with a compensating winding). The linear relationship between the measured torque and torque current is achievable at rated speed as shown in Figure 6-10. In this figure there is a slight difference between the analytically calculated torque and the measured torque. This may be a result of increased friction and windage losses, and other stray-load losses (the calculated torque is the developed torque whilst the measured torque is the shaft torque of the machine).

Table 6-1 gives the comparison of the calculated and measured torque values at rated conditions. From the table, it is clear that the analytical method provide a good approximation of the torque in the machine. The effects of changing k values are evaluated through measurements as shown in Figure 6-11. The figure shows that at the rated torque current, a small change in the value of k (resulting from, for example, a change in the rotor resistance) has a minimal effect on the torque of the machine. Also, at higher than rated torque current, a small change in k from the rated k -value leads to a reduction in torque as shown for $I_t = 7.5 \text{ A}$. Furthermore, it is shown in Figure 6-12 that a wrong value of k leads to the loss of the linear relationship between torque and torque current, that is, the loss of the MMF balance in the machine.

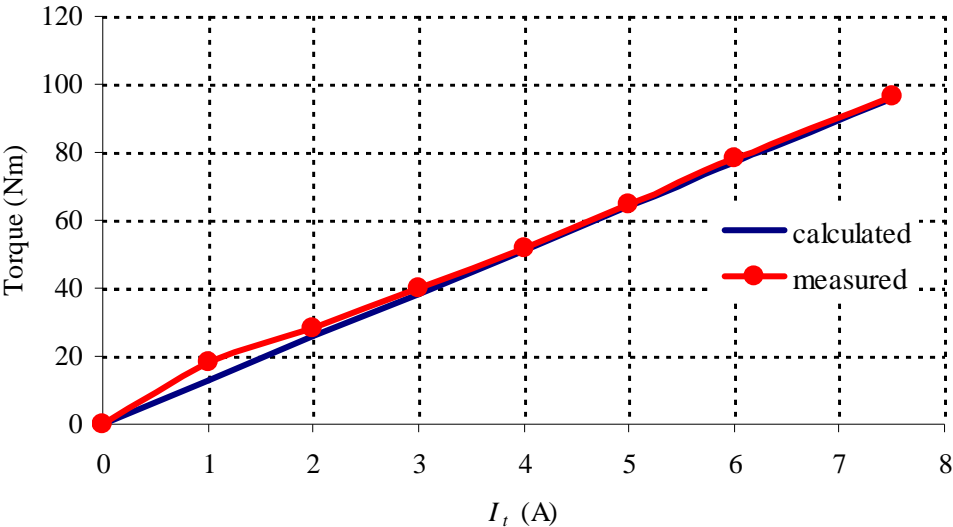


Figure 6-9. Comparison of the measured and calculated torque versus torque current with $I_f = 5.83 \text{ A}$ and $k = 0.638$. The rotor speed for this measurement is 500 r/min.

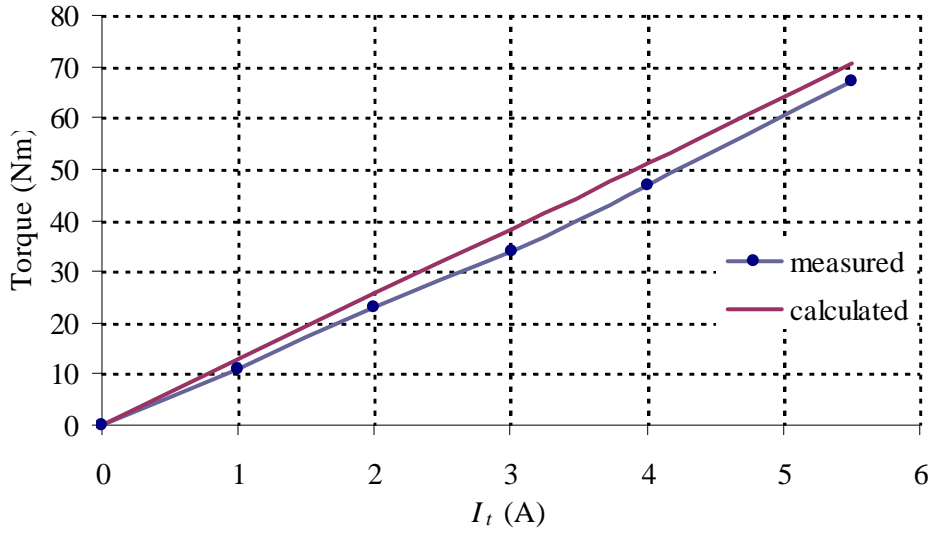


Figure 6-10. Comparison of the measured and calculated torque versus torque current with $I_f = 5.83$ A and $k = 0.638$. The rotor speed for this measurement is 1500 r/min.

Table 6-1. Rated torque with $I_f = 5.83$ A, $I_t = 5.5$ A and $k = 0.638$ at a rotor speed of 1466 r/min

	Torque (Nm)
FEA	67.5
Balanced condition, equation (5-12)	70.4
Analytical method of Chapter 4	64.4
Measured	67

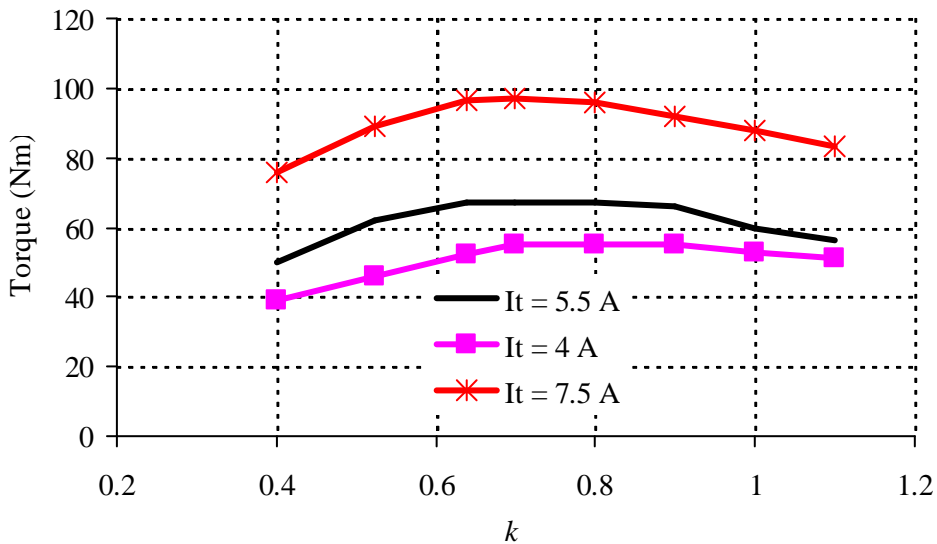


Figure 6-11. Measured effects of changing the k -value in the drive system on the torque for different values of I_t . The rotor speed for the measurements is 500 r/min.

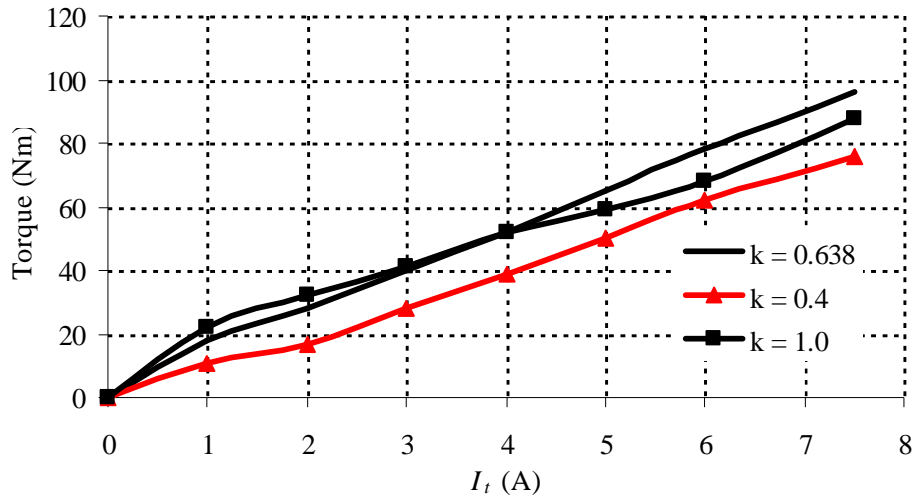


Figure 6-12. Measured effect of different k -values at 500 r/min.

6.4.2 Efficiency measurements at constant flux

The percentage efficiency of the drive system (converter and induction motor) is calculated as the percentage ratio of the output (shaft) power to the input (ac) power. The input power is measured with a power analyser at the ac supply of the converter. Figure 6-13 shows the measured percentage efficiency versus percentage load. The percentage load is calculated as the percentage ratio of the measured torque to the rated torque. The figure shows that there is a slight gain in efficiency when less field phases are used similar to what was observed in Chapter 3. Furthermore, the nine-phase induction machine drive system compares well, in terms of efficiency, to the standard three-phase drive system under constant volt per hertz operation as shown in the figure; a Danfoss drive is used in this case to supply the three-phase induction machine. The per phase stator current waveforms for different number of field and torque phase combinations are shown in Figure 6-14, at rated flux and load. Here, the negative (un-equal) effect of the $(m_f, m_t) = (4,5)$ winding option on the torque and field converter currents compared to the $(m_f, m_t) = (3,6)$ winding option, can be clearly seen.

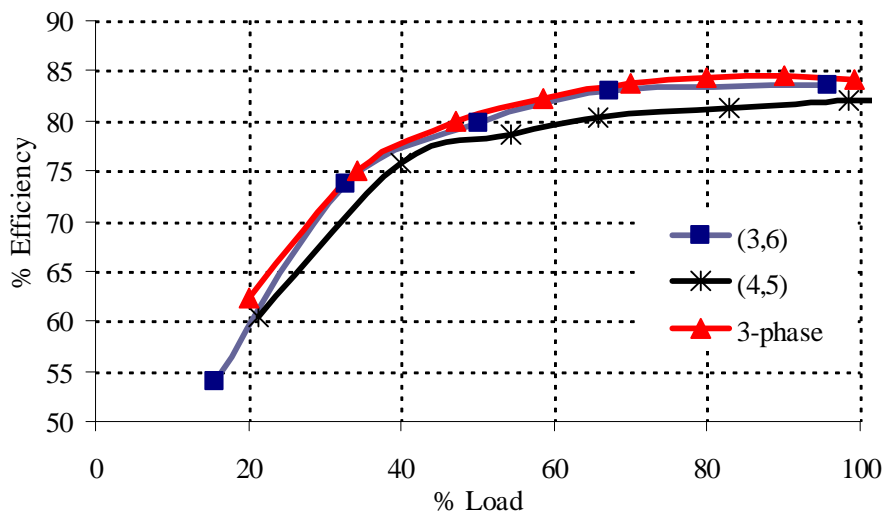


Figure 6-13. Measured system (converter and motor) efficiency versus percentage load of the nine-phase induction machine drive compared to a conventional three-phase induction machine drive, with (m_f, m_t) a parameter. (Rotor speed = 1500 r/min and at rated dc bus voltage of $V_{dc} = 400$ V)

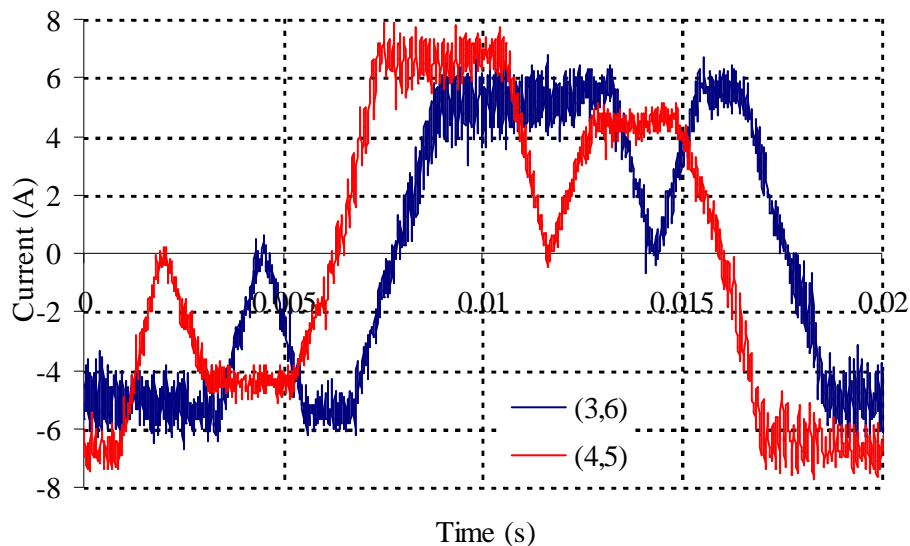


Figure 6-14. Measured stator current waveforms at rated flux and rated torque, with (m_f, m_t) a parameter and $k = 0.638$. For (3,6), $I_f = 5.83$ A and $I_t = 5.5$ A, whilst, for (4,5), $I_f = 4.68$ A and $I_t = 6.83$ A. The dc bus voltage for this measurement is, $V_{dc} = 400$ V and the rotor speed is 1500 r/min.

6.4.3 Flux weakening measurements above base speed

Similarly to dc drives, the output torque of the nine-phase induction machine drive is proportional to the product of the air-gap flux and the torque producing current. Therefore, the speed of the nine-phase induction machine can be increased above the rated 1500 r/min speed, whilst keeping the dc bus voltage constant and reducing the field current. The speed region above the rated speed is called the flux weakening or constant power speed region, since the machine torque falls in proportion with the flux, whilst the output power remains constant. The relationship between the air-gap flux density, control gain, k , and the field current of the machine versus frequency is shown in Figure 6-15. The flux density is halved at 3000 r/min, and the relationship between flux density and field current is obtained from Figure 5-12. The control gain, k , is inversely proportional to the flux density as given by (5-11). The measured torque versus the stator frequency of the drive is shown in Figure 6-16. The measured torque at rotor speed = 3000 r/min is 36 Nm whilst it is 67 Nm at 1500 r/min. The measured per phase stator current waveforms at base speed and double base speed are shown in Figure 6-17. The drop in the field current amplitude at double base-speed can be clearly seen. Note also the increase in slip frequency at double base speed. The current waveforms show that the current controller works well even at double rated frequency. The slip is clearly seen in the results. The results further confirm the brush dc compensating winding operation of the control method.

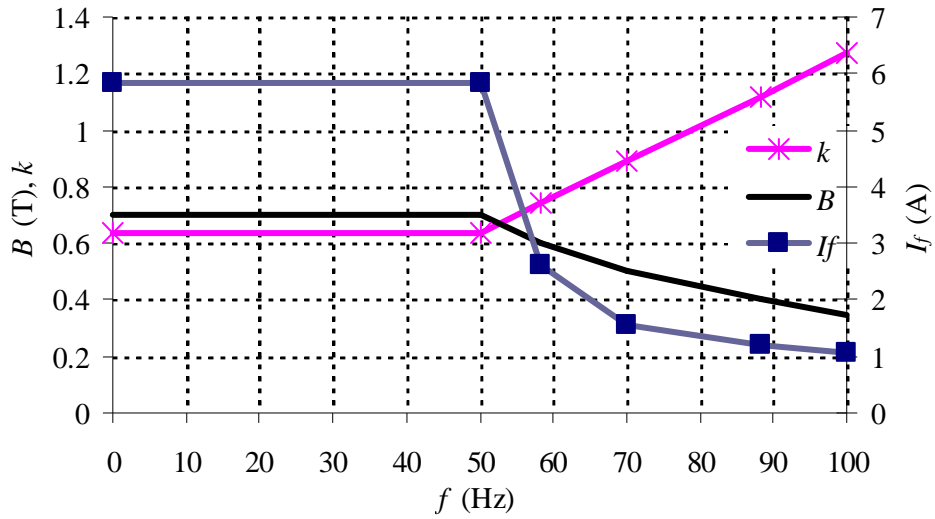


Figure 6-15. Relationship between the air-gap flux density, B , control gain, k , and field current, I_f , versus frequency, f .

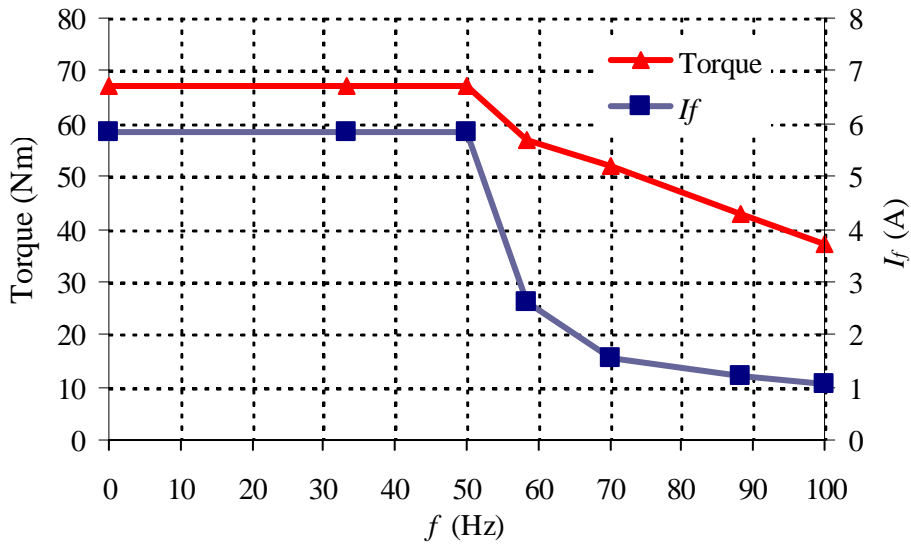


Figure 6-16. Measured torque and field current versus the frequency range of the drive.

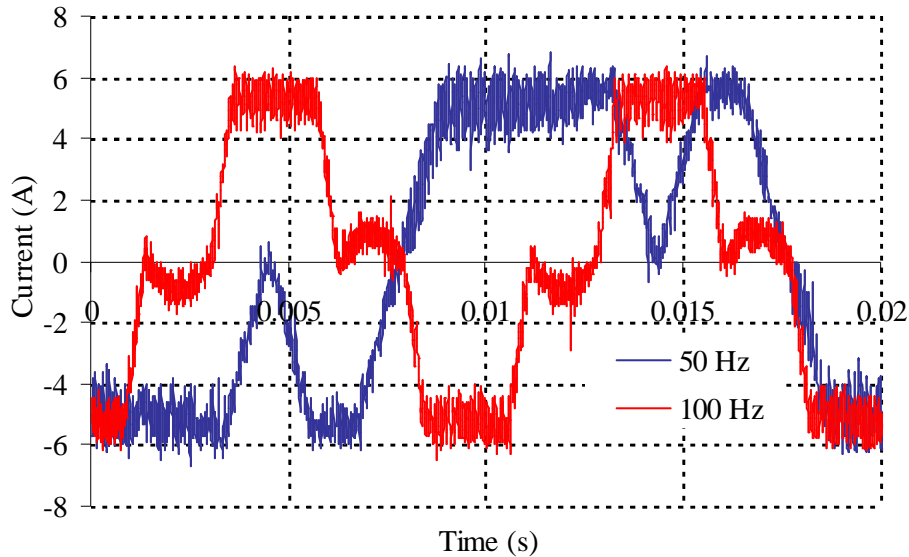


Figure 6-17. Measured stator current waveforms at 1500 r/min and 3000 r/min. The dc bus voltage for this measurement is $V_{dc} = 400$ V.

6.5 Ratio of torque to rotor copper losses

In this section, the theoretical ratios of torque to rotor copper losses of an induction motor supplied with three-phase or nine-phase sinusoidal currents and nine-phase trapezoidal currents are compared. The same full load stator copper losses are enforced to make these conditions comparable through the use of the same stator winding. Since the same stator winding is utilized, the same rms stator coil current is used. The trapezoidal rms current value is calculated to be 4.69 A at full load. Therefore, the rms current for the three-phase and nine-phase sinusoidal supplies is also 4.69 A in a coil. The rated speed is 1466 r/min for all the supply configurations of the machine.

The stator winding layout of the nine phase induction machine is the same as in Figure 4-8 and is repeated in Figure 6-18. The same nine-phase stator is also re-connected to form a three-phase stator, that is, the same nine-phase stator winding is used for both the trapezoidal and sinusoidal current supplies. From Figure 6-18, the three phase winding is mapped as follows:

Phase 1 of the three phase winding consists of phases A, B and C of the nine-phase winding.

Phase 2 of the three phase winding consists of phases D, E and F of the nine-phase winding.

Phase 3 of the three phase winding consists of phases G, H and I of the nine-phase winding.

The current directions in the three phase case remain the same as in the layout of the nine-phase winding. Note that the three-phase stator winding is a single layer winding.

In Table 6-2, the results of the analytically and FEA calculated torque to rotor copper loss ratios of the induction machine supplied with three different current waveform configurations are given. The results are calculated with torque in Newton-metre (Nm) and losses in watts (W). Good comparison is obtained between the analytically and FEA calculated ratios. The theoretical results in the table show that the ratio of the developed torque to rotor copper loss is lower when the machine is supplied with trapezoidal stator current waveforms. The effect of this on the overall efficiency of the drive is beyond the scope of this work and needs to be further investigated.

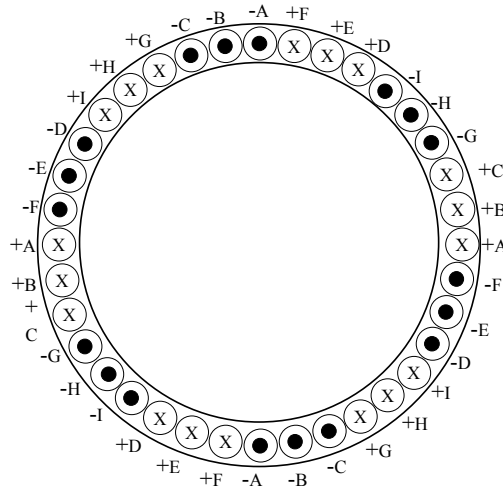


Figure 6-18. 36-slot, nine-phase stator winding layout.

Table 6-2. Comparison of the ratio of torque to rotor copper losses for different windings and different current waveform supplies.

	sinusoidal		trapezoidal
	3-phase (Nm/W)	9-phase (Nm/W)	9-phase (Nm/W)
Analytical method of Chapter 4	0.41	0.42	0.38
FEA	0.42	0.45	0.37

6.6 Summary

In this Chapter, theoretical results are validated through measurements on an 11 kW drive. Although there are differences in the amplitudes of the current waveforms, it is clear that the theoretical calculation gives a good prediction of the rotor bar and end ring current waveform shape. The FEA evaluated current waveform has a higher amplitude compared to that of the analytical method. However, the current waveform evaluated through the analytical method compares well with the measured one of the specially designed rotor. The torque of the machine is evaluated and measured for different values of the control gain, k , and the torque current. The measured value of the percentage efficiency of the proposed nine-phase induction machine drive compares well with the off-the-shelf drive. The proposed drive is also shown to operate comfortably at higher speeds.

In conclusion, the analytical method can be used in the study of the prediction of the shape of the rotor current. The square-like assumption of the rotor bar current waveform is shown to be incorrect. However, the square-like bar current assumption does provide a simple method of calculating the amplitude of the rotor current waveform. This is shown through the FEA results and also the measured results since the control gain, k , is calculated indirectly from the square-like assumed bar current waveform. Finally, the calculated results show a substantial drop in the ratio of the torque to rotor copper losses for the proposed drive. It is, thus, expected that the efficiency will not be as high as that with a sinusoidal supply.

Chapter 7

Conclusion and Recommendation

In this dissertation the proposed BDCE control method for multiphase induction machine drives is further investigated and evaluated. The focus of the study is specifically on cage rotor induction machine drives. This Chapter states the contributions and conclusions of the study, and also comes to recommendations for further study.

7.1 Contributions of the study

The following four aspects are considered as contributions of the study on the topic of BDCE controlled multiphase induction machine drives:

- (i) A simple, but confirmed to be accurate, analytical calculation method is presented whereby the defined optimal ratio of the number of field phases to the number of torque phases can be found for the drive. The method can be used in an initial study and preliminary design of the multiphase induction machine.
- (ii) The winding function theory is used in the development of an analytical simulation tool for the prediction of the rotor current waveform of a multiphase induction machine under BDCE control. This simulation is much faster than a FEA simulation. With the waveform known, the rotor copper losses and developed torque of the machine can be studied.
- (iii) Practical test results in the constant-flux and flux-weakening speed regions of a developed nine-phase, cage-rotor, multiphase induction machine drive are presented for the first time. These test results not only give information about the practicability of the proposed control method, but also about the performance of the drive with this type of control.
- (iv) The conclusions reached from this study give important new research information about the proposed control scheme. These conclusions are stated in the next section.

7.2 Conclusions

The following main conclusions are drawn from this study on the proposed BDCE control method for multiphase induction machine drives:

- (i) It is clearly found that there is a best (optimal) ratio of the number of field phases to the number of torque phases (m_f/m_t) of the multiphase induction machine. The optimal ratio equalises (or closely equalises) the rated field and torque inverter currents, and lowers and equalises the peak slot current densities in the machine. For 4-pole, 15-phase induction machines in the small to medium power levels this ratio is found to be $0.5 > m_f/m_t > 0.25$. In the megawatt application power level, it is found that $m_f/m_t = 3/12 = 0.25$ for a 4-pole, 15-phase machine.
- (ii) The rotor bar current is found not to have a quasi-square wave shape as assumed in the theory. It is argued that this difference may not simply be explained by transformer action, but rather by the same effect that is happening in dc commutator machines. This aspect still needs further clarification.
- (iii) Although the actual bar current is found different from the theoretically assumed bar current, this does not indicate or prove that the BDCE theory and the proposed control method are wrong and that it can not be used. In fact, it is proved that the theoretical and measured relationships between the torque and the torque current and between the flux and the field current of the proposed drive, are very close in agreement with each other. Furthermore, the proposed BDCE control scheme for the multiphase induction machine is

showed to work remarkably accurate. This has been specifically demonstrated in the field-weakening speed region of the drive.

- (iv) The overall measured efficiency of the proposed multiphase induction machine drive is found to be less but close to that of the conventional three-phase drive system (within 3%). This important aspect, however, needs much more investigation than in this study. A concern from the calculated results, hitherto, is that the torque per rotor copper loss performance of the proposed drive with its trapezoidal phase currents is showed to be 8 – 15 % lower than with sinusoidal currents. If future research shows that the overall efficiency of the drive is not as good, then there will be a serious question if the proposed multiphase drive scheme will be used by industry.

7.3 Recommendations

It is clear from the study in this dissertation that there are still important outstanding research questions to be answered about the proposed multiphase induction machine drive. The recommendations for further study on this topic are summarised as follows:

- (i) A design optimisation of the multiphase induction machine used in the proposed control scheme is necessary to specifically improve the efficiency and torque quality of the machine drive. Such a design optimisation must consider e.g. the rotor slot shape and the ratio of the number of stator slots to rotor slots.
- (ii) The power electronic converter design and the method of switching the inverter switches must be investigated to improve the efficiency of the drive. For example, for the H-bridge phase inverter, an auxiliary resonant commutated pole circuit can be used for soft switching. Also, for the H-bridge inverter switching, bipolar switching can be used to double the effective inverter switching.

If the outcomes of the research of (i) and (ii) above are positive, then the following further studies are recommended:

- (i) The dynamic modelling of the proposed drive system must be investigated to evaluate the dynamic response and performance of the proposed drive. The design of the current controllers e.g. can be done with this modelling.
- (ii) An investigation should be conducted in collaboration with industry into the development and evaluation of a very large multiphase induction machine drive of the proposed type. The following detail gives an interesting example of such a drive:

Rated power: 45 MW

Number of phases: 15

Number of field phases (m_f): 3

Number of torque phases (m_t): 12

Power per phase: $45\text{MW}/(12 - 1) = 4.09 \text{ MW}$

IGBT switches: 4.5 kV / 2000 A

DC-bus voltage: $V_{dc} = 0.75 \times 4.5 \text{ kV} = 3.375 \text{ kV}$

Rated field and torque phase currents: $I_f \approx I_t = 4.09 \text{ MW}/3.375 \text{ kV} = 1212 \text{ A}$.

References

- [1] G. K. Singh, Multi-phase induction machine drive research - a survey. *Elsevier Electric Power Systems Research*, 2002: p. 139-147.
- [2] E. Levi, R. Bojoi, F. Profumo, H. A. Toliyat, and S. Williamson, Multiphase induction motor drives - a technology status review. *IEE Proceedings - Electric Power Applications*, 2007. vol. 1, no. 4: p. 489-516.
- [3] A. C. Smith, S. Williamson, and C. G. Hodge. High torque dense naval propulsion motors. *Proc. IEEE International Electric Machines and Drives Conference IEMDC*,. 2003.
- [4] M. Jones, S. N. Vukosavic, and E. Levi, Parallel-connected multiphase multidrive systems with single inverter supply. *IEEE Transactions on Industrial Electronics*, 2009. vol. 56, no. 6: p. 2047 - 2057.
- [5] H. Xu, H. A. Toliyat, and L. J. Petersen. Rotor field oriented control of five-phase induction motor with the combined fundamental and third harmonic currents. *16th Annual IEEE Applied Power Electronics Conference and Exposition, APEC 2001*. 2001.
- [6] R. O. C. Lyra and T. A. Lipo, Torque density improvement in a six-phase induction motor with third harmonic current injection. *IEEE Transactions on Industry Applications*, 2002. vol. 38, no. 5: p. 1351-1360.
- [7] G. W. McLean, G. F. Nix, and S. R. Alwash, Performance and design of induction motors with square-wave excitation. *IEE Proceedings*, 1969. vol. 116, no. 8: p. 1405 - 1411.
- [8] H. A. Toliyat, T. A. Lipo, and J. C. White, Analysis of a concentrated winding induction machine for adjustable speed drive applications: Part 1 (motor analysis). *IEEE Transactions on Energy Conversion*, 1991. vol. 6: p. 679-683.
- [9] F. Terrien, S. Siala, and P. Noy. Multiphase induction motor sensorless control for electric ship propulsion. *Proc. IEE Power Electronics, Machines and Drives Conference. PEMD*. 2004.
- [10] R. I. Jones. The more electric aircraft: The past and the future? *IEE Colloquium on Electrical Machines and Systems for the More Electric Aircraft*. 1999.
- [11] M. J. J. Cronin, The all-electric aircraft. *IEE Review*, 1990. vol. 36: p. 3.9-311.
- [12] L. de Lillo, L. Empringham, P. W. Wheeler, S. Khwan-On, C. Gerada, M. N. Othman, and X. Huang, Multiphase power converter drive for fault-tolerant machine development in aerospace applications. *IEEE Transactions on Industrial Electronics*, 2010. vol. 57, no. 2: p. 575 - 583.
- [13] U. C. Mupambireyi, N. P. van der Duijn Schouten, B. M. Gordon, and R. A. McMahon. High phase number induction motor drives for battery applications. *The 8th International Conference on Power Electronics and Variable Speed Drives*. 2000. London, UK.
- [14] E. E. Ward and H. Harer, Preliminary investigation of an inverter-fed 5-phase induction motor. *Proceedings of IEE*, 1969. vol. 116, no. 6: p. 980-984.

- [15] R. H. Nelson and P. C. Krause, Induction machine analysis for arbitrary displacement between multiple winding sets. *IEEE Transactions on Power Apparatus and Systems*, 1974. vol. PAS-93, no. 3: p. 841 - 848.
- [16] T. M. Jahns, Improved reliability in solid-state ac drives by means of multiple independent phase drive units. *IEEE Transactions on Industry Applications*, 1980. vol. IA-16, no. 3: p. 321 - 331.
- [17] E. A. Klingshirn, High phase order induction motors-part 2-experimental results. *IEEE Transactions on Power Apparatus and Systems*, 1983. vol. PAS-102, no. 1: p. 54-59.
- [18] K. N. Pavithran, R. Parimelalagan, and M. R. Krishnamurthy, Studies on inverter-fed five-phase induction motor drive. *IEEE Transactions on Power Electronics*, 1988. vol. 3, no. 2: p. 224-235.
- [19] E. A. Klingshirn, High phase order induction motors-part i-description and theoretical considerations. *IEEE Transactions on Power Apparatus and Systems*, 1983. vol. PAS-102, no. 1: p. 47-53.
- [20] K. Gopakumar, S. Sathiakumar, S. K. Biswas, and J. Vithayathi, Modified current source inverter fed induction motor drive with reduced torque pulsations. *IEE Proceedings Electric Power Applications Part B*, 1984. vol. 131, no. 4: p. 159 - 164.
- [21] E. Levi, Multiphase electric machines for variable-speed applications. *IEEE Transactions on Industrial Electronics*, 2008. vol. 55, no. 5: p. 1893-1909.
- [22] D.C. White and H. H. Woodson, *Electromechanical energy conversion*. 1959, New York, NY: John Wiley and Sons.
- [23] T. A. Lipo. A d-q model for six-phase induction machine. *Proceedings on International Electric Machines Conference*. 1980.
- [24] M. A. Abbas, R. Christen, and T. M. Jahns, Six-phase voltage source inverter driven induction motor. *IEEE Transactions on Industry Applications*, 1984. vol. IA-20, no. 5: p. 1251-1259.
- [25] H. A. Toliyat, T. A. Lipo, and J. C. White, Analysis of a concentrated winding induction machine for adjustable speed drive applications: Part 2 (motor design and performance). *IEEE Transactions on Energy Conversion*, 1991. vol. 9, no. 4: p. 692-700.
- [26] H. A. Toliyat and T. A. Lipo, Transient analysis of cage induction machines under stator, rotor bar and end ring faults. *IEEE Transactions on Energy Conversion*, 1995. vol. 10: p. 241-247.
- [27] H. A. Toliyat, Analysis and simulation of five-phase variable-speed induction motor drives under asymmetrical connections. *IEEE Transactions on Power Electronics*, 1998. vol. 13, no. 4: p. 748-756.
- [28] H. A. Toliyat, M. S. Arefeen, and A. G. Parlos, A method for dynamic simulation of air-gap eccentricity in induction machines. *IEEE Transactions on Industry Applications*, 1996. vol. 32: p. 910-918.
- [29] M. J. Duran, F. Salas, and M. R. Arahal, Bifurcation analysis of five-phase induction motor drives with third harmonic injection. *IEEE Transactions on Industrial Electronics*, 2008. vol. 55, no. 5: p. 2006-2014.

- [30] L. De Camillis, M. Matuonto, A. Monti, and A. Vignati, Optimizing current control performance in double winding asynchronous motors in large power inverter drives. *IEEE Transactions on Power Electronics*, 2001. vol. 16, no. 5: p. 676 - 685.
- [31] G. K. Singh, K. Nam, and S. K. Lim, A simple indirect field-oriented control scheme for multiphase induction machine. *IEEE Transactions on Industrial Electronics*, 2005. vol. 52, no. 4: p. 1177-1184.
- [32] R. Bojoi, F. Farina, A. Tenconi, and F. Profumo, Dual three-phase induction motor drive with digital current control in the stationary reference frame. *IEE Proceedings - Electric Power Applications*, 2006. vol. 153, no. 1: p. 129-139.
- [33] R. Bojoi, M. Lazzari, F. Profumo, and A. Tenconi, Digital field-oriented control for dual three-phase induction motor drives. *IEEE Transactions on Industry Applications*, 2003. vol. 39, no. 3: p. 752-760.
- [34] R. Bojoi, G. Griva, and F. Profumo. Field oriented control of dual three-phase induction motor drives using a Luenberger flux observer. *41st Industry Applications Conference Annual Meeting*. 2006.
- [35] S. N. Vukosavic, M. Jones, E. Levi, and J. Varga, Rotor flux oriented control of a symmetrical six-phase induction machine. *Elsevier Electric Power Systems Research*, 2005. vol. 75: p. 142-152.
- [36] R. Kianinezhad, B. Nahid-Mobarakeh, F. Betin, and G. A. Capolino. Sensorless field-oriented control for six-phase induction machines. *Industry Applications Conference, 2005. 14th IAS Annual Meeting*. 2005.
- [37] R. Bojoi, A. Tenconi, G. Griva, and F. Profumo, Vector control of dual-three-phase induction-motor drives using two current sensors. *IEEE Transactions on Industry Applications*, 2006. vol. 42, no. 5: p. 1284 - 1292.
- [38] A.D. Graham. Vector control of a multiphase induction motor with open circuit phases. *IEEE International Electric Machines and Drives Conference, IEMDC '09*. 2009.
- [39] S. Mythili and K. Thyagarajah. Direct torque control (DTC) of multi-phase induction motor using tms320f2407 digital signal processor. *International Conference on Power Electronics and Drives Systems, PEDS 2005*. 2005.
- [40] H.A. Toliyat and X. Huangsheng. A novel direct torque control (DTC) method for five-phase induction machines. *Fifteenth Annual IEEE Applied Power Electronics Conference and Exposition, APEC 2000*. 2000.
- [41] R. Kianinezhad, B. Nahid, F. Betin, and G. A. Capolino. A novel direct torque control (DTC) method for dual three phase induction motors. *IEEE International Conference on Industrial Technology, ICIT 2006*. 2006.
- [42] R. Kianinezhad, R. Alcharea, B. Nahid, F. Betin, and G. Capolino. A novel direct torque control (dte) for six-phase induction motors with common neutrals. *International Symposium on Power Electronics, Electrical Drives, Automation and Motion, SPEEDAM 2008*. 2008.

- [43] R. Bojoi, F. Farina, G. Griva, F. Profumo, and A. Tenconi, Direct torque control for dual three-phase induction motor drives. *IEEE Transactions on Industry Applications*, 2005. vol. 41, no. 6: p. 1627-1636.
- [44] K. Hatua and V. T. Ranganathan, Direct torque control schemes for split-phase induction machine. *IEEE Transactions on Industry Applications*, 2005. vol. 41, no. 5: p. 1243-1254.
- [45] X. Huangsheng, H. A. Toliyat, and L. J. Petersen, Five-phase induction motor drives with dsp-based control system. *IEEE Transactions on Power Electronics*, 2002. vol. 17, no. 4: p. 524 - 533.
- [46] Y. Zhao and T. A. Lipo, Space vector PWM control of dual three-phase induction machine using vector space decomposition. *IEEE Transactions on Industry Applications*, 1995. vol. 31, no. 5: p. 1100 - 1109.
- [47] K. K. Mohapatra, K. Gopakumar, V. T. Somasekhar, and L. Umanand. A novel modulation scheme for a six phase induction motor with open-end windings. *Industrial Electronics Society, 28th Annual Conference of the IEEE, IECON 02*. 2002.
- [48] D. Casadei, M. Mengoni, G. Serra, A. Tani, and L. Zarri. An algorithmic approach to space vector modulation for multiphase inverters. *24th Annual IEEE Applied Power Electronics Conference and Exposition, APEC 2009*. 2009.
- [49] K. Marouani, L. Baghli, D. Hadiouche, A. Kheloui, and A. Rezzoug. Discontinuous SVPWM techniques for double star induction motor drive control. *32nd IEEE Annual Conference on Industrial Electronics, IECON 2006*. 2006.
- [50] M. J. Duran and E. Levi. Multi-dimensional approach to multi-phase space vector pulse width modulation. *32nd IEEE Annual Conference on Industrial Electronics, IECON*. 2006.
- [51] A. Lega, M. Mengoni, G. Serra, A. Tani, and L. Zarri, Space vector modulation for multiphase inverters based on a space partitioning algorithm. *IEEE Transactions on Industrial Electronics*, 2009. vol. 56, no. 10: p. 4119 - 413.
- [52] D. Dujic, M. Jones, and E. Levi. Space vector PWM for nine-phase vsi with sinusoidal output voltage generation: Analysis and implementation. *33rd Annual Conference of the IEEE Industrial Electronics Society, IECON 2007*. 2007.
- [53] D. Dujic, M. Jones, and E. Levi. Continuous carrier-based vs. Space vector PWM for five-phase vsi. *The International Conference on "Computer as a Tool", EUROCON 2007*.
- [54] A. Iqbal and S. Moinuddin, Comprehensive relationship between carrier-based PWM and space vector PWM in a five-phase VSI. *IEEE Transactions on Power Electronics*, 2009. vol. 24, no. 10: p. 2379 - 2390.
- [55] D. Gritter and S. S. Kalsi. Variable speed electric drive options for electric ships. *IEEE Electric Ship Technologies Symposium, ESTS*. 2005.
- [56] S. Lu and K. Corzine. Multilevel multi-phase propulsion drives. *2005 IEEE Electric Ship Technologies Symposium*. 2005.

- [57] O. Lopez, J. Alvarez, J. Doval-Gandoy, and F. D. Freijedo, Multilevel multiphase space vector PWM algorithm with switching state redundancy. *IEEE Transactions on Industrial Electronics*, 2009. vol. 56, no. 3: p. 792 - 804.
- [58] Y. Ai, M. J. Kamper, and A. D. Le Roux, Novel direct flux and direct torque control of six-phase induction machine with nearly square air gap flux density. *IEEE Transactions on Industry Applications*, 2007. vol. 43, no. 6: p. 1534-1543.
- [59] K. Gopakumar, V. T. Ranganthan, and S. R. Bhat, Split-phase induction motor operation from PWM voltage source inverter. *IEEE Transactions on Industry Applications*, 1993. vol. 29, no. 5: p. 927 - 932.
- [60] F. Barrero, M. R. Arahal, R. Gregor, S. Toral, and M. J. Duran, A proof of concept study of predictive current control for VSI-driven asymmetrical dual three-phase ac machines. *IEEE Transactions on Industrial Electronics*, 2009. vol. 56, no. 6: p. 1937 - 1954.
- [61] M. Jones, S. N. Vukosavic, D. Dujic, and E. Levi, A synchronous current control scheme for multiphase induction motor drives. *IEEE Transactions on Energy Conversion*, 2009. vol. 24, no. 4: p. 860 - 868.
- [62] E. Abdi-Jalebi, P. C. Roberts, and R. A. McMahon. Real-time rotor bar current measurement using a Rogowski coil transmitted using wireless technology. *18th International Power System Conference, PSC2003*. 2003.
- [63] E. Abdi-Jalebi and R. McMahon. Application of real-time rotor current measurements using bluetooth wireless technology in study of the brushless doubly-fed (induction) machine (BDFM). *41st IAS Annual Meeting IEEE Industry Applications Conference*. 2006.
- [64] C. Bruzzese, O. Honorati, and E. Santini. Spectral analyses of directly measured stator and rotor currents for induction motor bar breakages characterization by M.C.S.A. *International Symposium on Power Electronics, Electrical Drives, Automation and Motion, SPEEDAM 2006*. 2006.
- [65] D. A. Ward and J. L. T. Exon, Using Rogowski coils for transient current measurements. *Engineering Science and Education Journal*, 2003.
- [66] W. F. Ray and C. R. Hewson. High performance Rogowski current transducers. *Industry Applications Conference*. 2000.
- [67] L. Weichao, H. An, G. Shiguang, and S. Chi. Rapid control prototyping of fifteen-phase induction motor drives based on DSPACE. *International Conference on Electrical Machines and Systems, ICEMS 2008*. 2008.
- [68] N. Gule and M. J. Kamper. Optimal ratio of field to torque phases in multi-phase induction machines using special phase current waveforms. *Proceedings of International Conference on Electrical Machines (ICEM2008)*. 2008.
- [69] I. Boldea and S. A. Nassar, *The induction machine handbook*. 2002, Florida: CRC Press LLC.

- [70] D. S. Babb and J. E. Williams, Circuit analysis method for determination of a-c impedances of machine conductors. *AIEE Transactions (Power Apparatus and Systems)*, 1951. vol. 70: p. 661-666.
- [71] D. S. Babb and J. E. Williams, Network analysis of a-c machine conductors. *AIEE Transactions (Power Apparatus and Systems)*, 1951. vol. 70: p. 2001-2005.
- [72] M. M. Liwschitz-Garik, Skin-effect bars of squirrel-cage rotors. *AIEE Transactions (Power Apparatus and Systems), Part III*, 1954: p. 255-258.
- [73] M. M. Liwschitz-Garik, Computation of skin effect in bars of squirrel-cage rotors. *AIEE Transactions (Power Apparatus and Systems)*, 1955: p. 768-771.
- [74] E. A. Klingshirn, Polyphase induction motor performance and losses on nonsinusoidal voltage sources. *IEEE Transactions on Power Apparatus and Systems*, 1968. vol. PAS-87: p. 624-631.

Appendix A

Control of Induction Machines

Scalar control is a widely used method to control induction machines. In this control technique, the machine is controlled by magnitude variation of the control variable, for example, voltage or current and frequency. It is a relatively easy control method to implement. Its major disadvantage is the inherent coupling effect leading to sluggish torque response and instability. The coupling is a result of the dependence of both the flux and the torque on the voltage or current and the frequency.

An improved method of scalar control is called direct torque control (DTC). Here, an inverter voltage space vector selection through a lookup table is used to control the torque and the stator flux directly. Scalar controlled drives have inferior performance compared to vector controlled drives. A very brief description of the principle and operation of vector control and DTC follows.

A.1 Vector Control

Vector control is used in order to make an induction motor drive to operate similarly to a separately excited dc motor drive. In a dc machine, the analytic expression for the developed torque (T) is a product of the field current (I_f) and the armature current (I_a) multiplied by a constant (K), that is

$$T = KI_a I_f \quad (\text{A-1})$$

This expression of the torque is true when armature reaction is ignored. A dc machine is constructed such that the field flux is perpendicular to the armature flux and therefore the flux's space vectors are decoupled. The field current is kept constant (and thus the flux), and the torque is controlled by controlling the armature current and thus a fast transient response is obtained. Since the field and armature flux space vectors are orthogonal, any changes in the field current have no effect on the armature flux and vice versa. Similar performance can be obtained in an induction motor if the machine control is considered in a synchronously rotating reference frame. The transformation leads to the sinusoidal variables appearing as dc quantities in steady state. Under this transformation, the armature / stator current and flux are resolved into two components which rotate synchronously with the rotor and with the air gap flux wave. The armature current and flux components that are aligned with the field winding are referred to as direct axis components, whilst those which are perpendicular to this axis are referred to as quadrature axis components. Thus, with vector control, the developed torque in an induction machine is given by,

$$T = K_I i_{ds} i_{qs}, \quad (\text{A-2})$$

where i_{ds} and i_{qs} are the direct axis and quadrature axis components of the armature / stator currents in a synchronously rotating reference frame respectively. In vector control operation, it is important that the currents are kept perpendicular to each other for all operating conditions in order to achieve the dc-machine-like performance. The operation of vector control can be better explained through Figure A.1.

In Figure A.1, the machine is perceived to perform the transformation internally such that it can be controlled by the control currents i_q^* and i_d^* . The control currents i_q^* and i_d^* , which are currents in the synchronously (dq) rotating reference frame, are first inverse transformed to a stationary reference frame ($d_s q_s$) and then to three-phase control currents. The inverter then generates the currents i_a , i_b and i_c , which are then transformed to a stationary reference frame inside the machine. The stationary reference frame currents are transformed to the rotating reference frame which in turn produces the field and torque in the induction machine. The unit vector is used to maintain the alignment and orientation of the flux vector and the current perpendicular to it. The control currents on the control side in Figure A.1 correspond to the machine currents i_d and i_q .

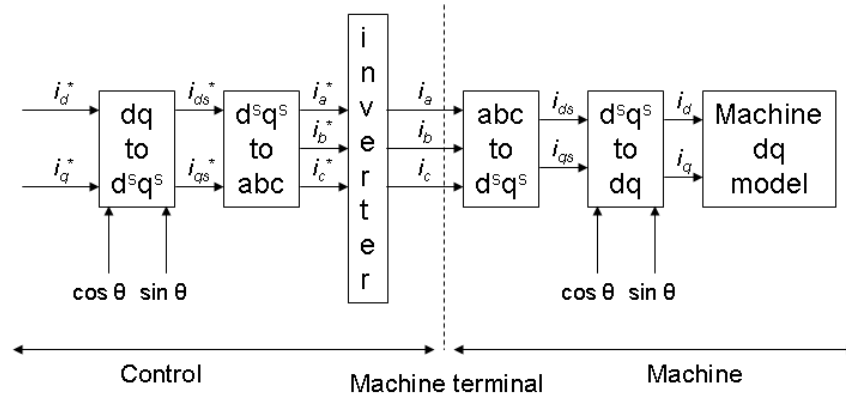


Figure A.1. Vector control principle

A.2 Direct Torque Control (DTC)

Direct torque control (DTC) allows the direct control of the stator flux and the torque by selecting the appropriate inverter states without any coordinate transformations. Figure A.2 shows the operation of DTC. As can be seen from the schematic, the stator flux and the torque reference values are compared with actual (estimated values). The hysteresis controller's output values together with the flux sector are used as inputs to the look up table. The flux and torque estimations required for this technique, increases in complexity with increase in the number of stator phases being used in an induction machine.

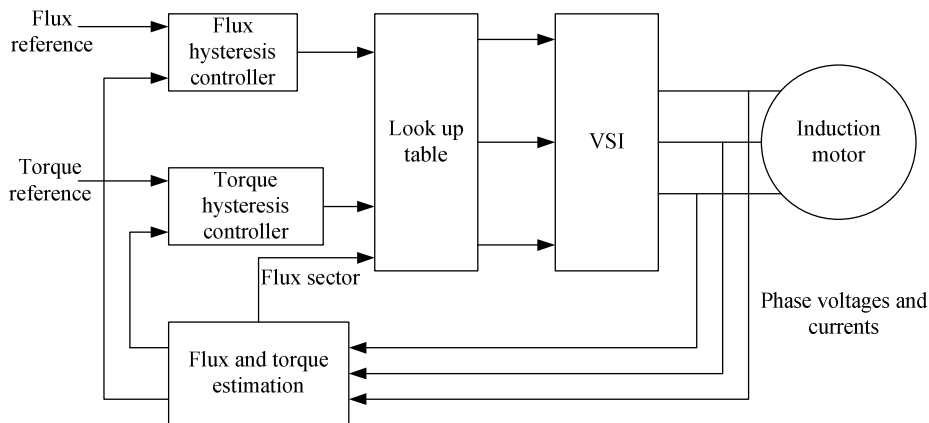


Figure A.2. Direct torque control principle

Appendix B

Rogowski coil

A schematic diagram of a Rogowski coil obtained from literature is shown in Figure B.1. Assuming an evenly wound coil with N turns/m on a non-magnetic former of average cross sectional area, A , in m^2 , then the induced voltage at the coil terminals, E , is proportional to the rate of change of the encircled current, I , that is

$$E = \mu_o NA \frac{dI}{dt} . \quad (\text{B-1})$$

This holds only if the coil is a closed loop with no discontinuities. The integrator output within the designed working bandwidth is,

$$V_{out} = \frac{1}{\tau} \int E dt , \quad (\text{B-2})$$

where τ is the integration time constant. The sensitivity in volts per ampere is

$$\frac{V_{out}}{I} = \frac{\mu_o NA}{\tau} . \quad (\text{B-2})$$

Then the sensitivity can be adjusted such that the same Rogowski coil can be used to measure current ranging from a few milli-amperes to several mega-amperes. The flexibility in the design of the Rogowski current transducer (achieved through altering the number of turns and the cross sectional area of the coil and adjusting the integrator) provides a versatile current measuring system.

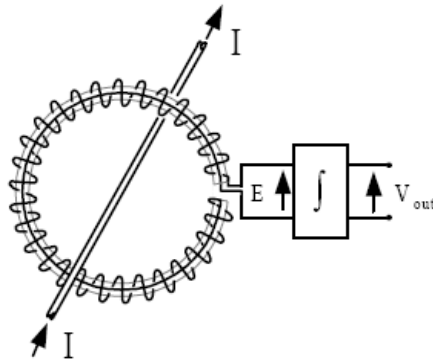


Figure B.1. The basic Rogowski current transducer.

Appendix C

Calculation of Resistances and Inductances

C.1 End Ring Resistance and Inductance Calculation

When dc current flows uniformly across the end ring, the resistance of the ring is given by

$$R_{dc} = \frac{\rho l}{A}, \quad (\text{C-1})$$

where ρ is the resistivity of the bar material at a particular temperature, l is the average length between rotor bars and A is the cross sectional area of the ring segment. The relationship between the resistivity and temperature is,

$$\rho = \rho_{20}(1 + Y(t - 20)), \quad (\text{C-2})$$

where ρ_{20} is the bar material resistivity at 20°C, $Y = 0.0039/^\circ\text{C}$ and t is the temperature at which the resistivity is calculated at.

With the following definitions: M_r is the number of rotor bars, l_i is the average length of the end ring segment, p is the number of pole pairs, and a and b are the breadth and height of the end ring segment respectively. Then the end ring inductance is given by [69],

$$L_{er} = \mu_0 l_i \frac{2.3d_r}{4M_r l (\sin^2(\pi p / M_r))} \ln\left(\frac{4.7d_r}{(a + 2b)}\right), \quad (\text{C-3})$$

with the end-ring attached to the rotor stack and

$$L_{er} = \mu_0 l_i \frac{2.3d_r}{4M_r l (\sin^2(\pi p / M_r))} \ln\left(\frac{4.7d_r}{2(a + b)}\right), \quad (\text{C-4})$$

with the end ring distanced from the stack.

C.2 Rotor Bar Resistance and Inductance

The effective cross sectional area of a conductor carrying high frequency alternating current decreases due to the skin effect. A number of techniques have been employed to calculate the bar resistance at different frequencies. It is generally assumed that the bar fills the slot. Babb and Williams [70], [71] proposed a method whereby transmission line equations are used to calculate the rotor bar impedance. The impedance of a rectangular bar can be calculated as

$$Z_r = \frac{1}{Y} \sqrt{YZ} \operatorname{ctnh} \sqrt{YZ}, \quad (\text{C-5})$$

where,

$$\begin{aligned} Y &= \frac{1}{R} \\ Z &= j2\pi fL \\ R &= \rho \frac{1}{A} \\ L &= \mu_0 \frac{d}{3w}. \end{aligned} \quad (\text{C-6})$$

In C-6, R is the per unit length slot resistance, f is frequency in Hz, L is the per unit length slot inductance, A is the bar cross sectional area, μ_0 is the absolute permeability, d is the bar depth and w is the bar width.

Similarly, Liwschitz-Garik [72], [73] proposed the following formula for calculating the bar impedance,

$$Z_r = \frac{\rho}{w} \alpha \frac{\sinh(2\alpha d) + \sin(2\alpha d)}{\cosh(2\alpha d) - \cos(2\alpha d)}, \quad (C-7)$$

where

$$\alpha = \sqrt{\frac{\omega\mu_0}{2\rho}}, \quad \omega = 2\pi f. \quad (C-8)$$

Both the above methods yield similar results, and the relationship between the ratio of the ac to dc bar resistance versus frequency is shown in Figure C.1. It is clear that at 50 Hz the ac resistance is almost double the dc resistance. Therefore, the effect of frequency on the resistance is important in the analytical evaluation of a machine's performance. The frequency effect on inductance is shown in Figure C.2. The inductance of the bar decreases as frequency increases, as shown in Figure C.2.

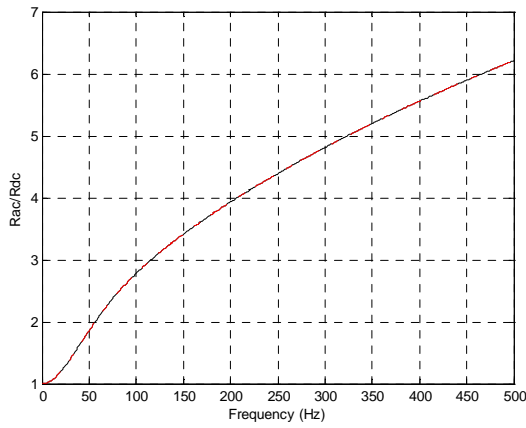


Figure C.1. Relationship between R_{ac}/R_{dc} and frequency of a 4 mm by 25 mm cage rotor bar.

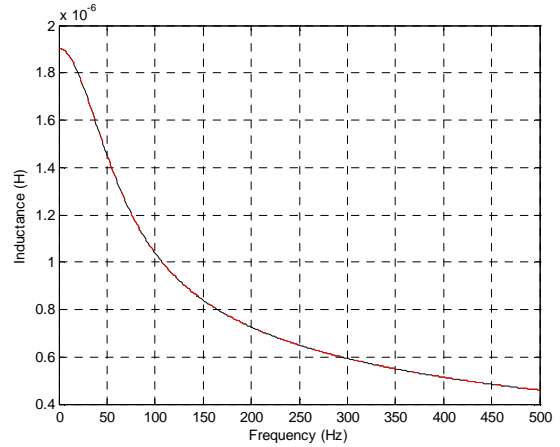


Figure C.2. Relationship between inductance and frequency a 4 mm by 25 mm cage rotor bar.

Appendix D

Digital Hysteresis Controller

The motor stator phase winding current flows in both directions of the H-bridge shown in Figure D.1. Bipolar switching is used in the inverter control. The FPGA in the DSP controller executes the software based digital hysteresis current control. Hysteresis control can be explained with the aid of Figure D.2. With this controller, the current is kept within a predefined band. The band borders the reference current that is calculated in the DSP. The FPGA samples each stator phase current at a rate of 250 kHz, and then compares it with a lower and / or upper band current. If the actual current exceeds the upper band current, as shown in Figure D.2, switches S_1 and S_4 are turned OFF, while switches S_3 and S_2 are turned ON after an interval of dead time. The opposite occurs if the actual current crosses the lower band. The same control signal controls switches S_1 and S_4 whilst its inverse controls S_3 and S_2 . If the actual current is in the band, the switches remain unchanged.

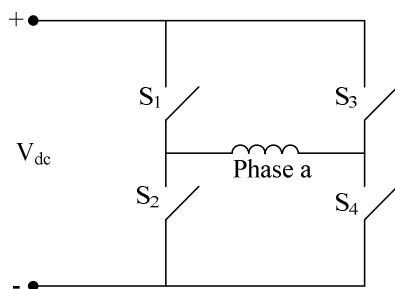


Figure D.1. Per phase H-bridge inverter circuit.

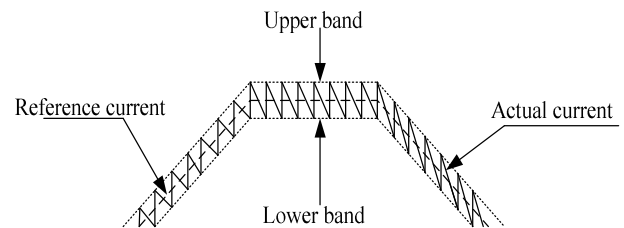


Figure D.2. Hysteresis band with reference current and actual current.

Appendix A

Per Phase Equivalent Circuit

The general three-phase induction machine per phase equivalent circuit approach has been widely used to evaluate the steady state performance of an induction machine. This approach is presented in this section as it is used in the steady state performance evaluation of a nine-phase induction machine. An approach similar to the one presented in [74] is adopted. In [74], the stator voltage is broken down to its frequency components and the equivalent circuit approach is used to evaluate the performance of the machine. For simplicity, saturation is ignored and it is assumed that there are independent current sources for each harmonic order 1 to x as shown in Figure E.1. The nine-phase machine is assumed to be made of three independent symmetrical three-phase machines. Each harmonic is represented by an independent equivalent circuit since it is assumed that each harmonic is independent of the others. The circuits are shown in Figure E.2.

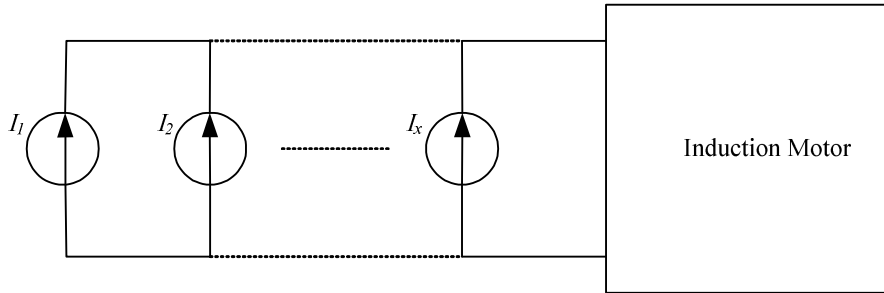


Figure E.1. Per phase excitation of the induction machine with stator current harmonics (the current harmonics forms the trapezoidal current waveform).

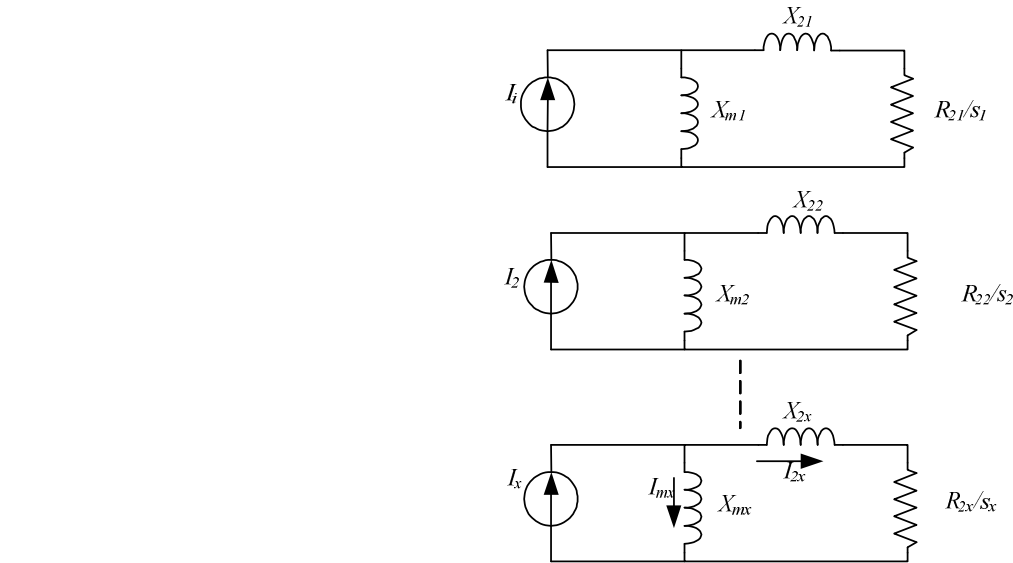


Figure E.2. Per phase equivalent circuit for each stator current harmonic.

E.1 Determination of the x th Equivalent Circuit Parameters

From Figure E.2, I_{2x} can be found by using Kirchoffs current law as follows:

$$I_x = I_{mx} + I_{2x}$$

$$(I_x - I_{2x}) jX_{mx} = I_{2x} (jX_{2x} + R_{2x} / s_x). \quad (\text{E-1})$$

Then,

$$I_{2x} = \frac{I_x jX_{mx}}{jX_{mx} + jX_{2x} + R_{2x} / s_x}, \quad (\text{E-2})$$

and the rotor bar current is

$$I_b = \frac{I_{2x} N_s N_p}{N_r M_r}, \quad (\text{E-3})$$

where, I_x is the x th harmonic current, I_{mx} is the x th harmonic magnetizing current, I_{2x} is the x th harmonic rotor current referred to the stator, X_{mx} is the x th magnetizing reactance, X_{2x} is the x th rotor reactance referred to the stator, R_{2x} is the x th rotor resistance, s_x is the x th per unit slip and p is the number of pole pairs. Generally,

$$X_{mx} = \frac{2N_p x f N_s^2 \mu_0 l d_r}{p^2 g}, \quad (\text{E-4})$$

$$X_{2x} = \frac{12\pi x f l N_s^2 L_{slot} N_p}{M_r}, \quad (\text{E-5})$$

$$R_{2x} = \frac{4l N_s^2 R_{slot} N_p}{M_r}, \quad (\text{E-6})$$

where, N_p is the number of phases, f is the fundamental frequency, N_s is the number of stator series turns, l is the stack length, d_r is the rotor diameter, g is the air-gap length, M_r is the number of rotor slots, L_{slot} is the per unit length slot inductance and R_{slot} is the per unit length slot resistance. L_{slot} and R_{slot} are calculated through the method provided by Babb and Williams [70, 71] as explained in Appendix C since they vary with each harmonic frequency.

E.2 Analysis of the x th Equivalent Circuit

Each equivalent circuit is analyzed independently. The resultant power transferred across the air-gap is calculated as

$$P_g = \sum_{x=1}^{\infty} \frac{N_p I_{2x}^2 R_{2x}}{s_x}. \quad (\text{E-7})$$

The rotor I^2R loss can be calculated as

$$P_{rotor} = \sum_{x=1}^{\infty} N_p I_{2x}^2 R_{2x}. \quad (\text{E-8})$$

Then the electromagnetic power developed by the machine is

$$P_{em} = P_g - P_{rotor}. \quad (\text{F-9})$$

Similarly, the resultant electromagnetic torque of the machine is the sum of all the torques produced by each current harmonic, that is,

$$T_{em} = \frac{P_{em}}{\omega_r} = \sum_{x=1}^{\infty} \frac{N_p I_{2x}^2 R_{2x} P}{s_x \omega}. \quad (\text{E-10})$$